

OPTICAL STAR-FORMATION RATE INDICATORS

JOHN MOUSTAKAS¹, ROBERT C. KENNICUTT, JR.^{1,2}, & CHRISTY A. TREMONTI¹

ApJ, accepted

ABSTRACT

Using integrated optical spectrophotometry for 412 star-forming galaxies at $z \sim 0$, and fiber-aperture spectrophotometry for 120,846 SDSS galaxies at $z \sim 0.1$, we investigate the $H\alpha$ $\lambda 6563$, $H\beta$ $\lambda 4861$, $[O\ II]$ $\lambda 3727$, and $[O\ III]$ $\lambda 5007$ nebular emission lines and the U -band luminosity as quantitative star-formation rate (SFR) indicators. We demonstrate that the extinction-corrected $H\alpha$ $\lambda 6563$ luminosity is a reliable SFR tracer even in highly obscured star-forming galaxies. We find that variations in dust reddening dominate the systematic uncertainty in SFRs derived from the observed $H\beta$, $[O\ II]$, and U -band luminosities, producing a factor of ~ 1.7 , ~ 2.5 , and ~ 2.1 scatter in the mean transformations, respectively. We show that $[O\ II]$ depends weakly on variations in oxygen abundance over a wide range in metallicity, $12 + \log(O/H) = 8.15 - 8.7$ dex ($Z/Z_{\odot} = 0.28 - 1.0$), and that in this metallicity interval galaxies occupy a narrow range in ionization parameter ($-3.8 \lesssim \log U \lesssim -2.9$ dex). We show that the scatter in $[O\ III]$ $\lambda 5007$ as a SFR indicator is a factor of 3–4 due to its sensitivity to metal abundance and ionization. We develop empirical SFR calibrations for $H\beta$ and $[O\ II]$ parameterized in terms of the B -band luminosity, which remove the systematic effects of reddening and metallicity, and reduce the SFR scatter to $\pm 40\%$ and $\pm 90\%$, respectively, although individual galaxies may deviate substantially from the median relations. Finally, we compare the $z \sim 0$ relations between blue luminosity and reddening, ionization, and $[O\ II]/H\alpha$ ratio against measurements at $z \sim 1$ and find broad agreement. We emphasize, however, that optical emission-line measurements including $H\alpha$ for larger samples of intermediate- and high-redshift galaxies are needed to test the applicability of our locally derived SFR calibrations to distant galaxies.

Subject headings: galaxies: abundances — galaxies: evolution — galaxies: formation — galaxies: ISM

1. INTRODUCTION

Over the past twenty years many techniques have been devised to estimate the global star-formation rates (SFRs) of galaxies. The first quantitative analysis of SFRs using the $H\alpha$ $\lambda 6563$ nebular recombination line was undertaken by Kennicutt (1983). Today, with the advent of large, multi-wavelength surveys of galaxies, virtually every part of the electromagnetic spectrum has been explored as a means of deriving SFRs (e.g., Kennicutt 1983; Buat et al. 1989; Condon 1992; David et al. 1992). Two indicators directly associated with massive star formation are the ultraviolet (UV; $\lambda\lambda 1200 - 2500$ Å) and nebular recombination line luminosities. These techniques were particularly important in establishing the order-of-magnitude rise in the SFR density of the universe from the present day to $z = 1$ and beyond (Lilly et al. 1996; Madau et al. 1996; Cowie et al. 1997; Glazebrook et al. 1999; Steidel et al. 1999; Hopkins 2004). Despite considerable progress in measuring SFRs of distant galaxies, however, their accuracy remains limited by a wide range of systematic uncertainties (Cram et al. 1998; Glazebrook et al. 1999; Bell & Kennicutt 2001; Sullivan et al. 2001; Hopkins et al. 2001, 2003; Charlot et al. 2002; Rosa-González et al. 2002; Kewley et al. 2002, 2004; Hirashita et al. 2003; Bell 2003). Well-calibrated SFR diagnostics with well-understood systematic uncertainties are needed to improve constraints on the evolution

of the cosmic SFR, and to investigate the physical processes responsible for this evolution. In this paper we carry out a detailed empirical analysis of rest-frame optical SFR indicators.

One of the most well-understood SFR indicators is $H\alpha$ $\lambda 6563$. The $H\alpha$ luminosity is directly proportional to the hydrogen-ionizing radiation from massive ($\gtrsim 10 M_{\odot}$) stars, and therefore provides a near-instantaneous ($\lesssim 10$ Myr) measure of the SFR with minimal dependence on the physical conditions of the ionized gas (Kennicutt 1998). Unfortunately, $H\alpha$ is only observable from the ground at $z \lesssim 0.4$ in the optical, and at $0.7 \lesssim z \lesssim 2.5$ through the near-infrared atmospheric windows (Fig. 1). Given the observational difficulties of observing $H\alpha$ at high redshift, therefore, the $[O\ II]$ $\lambda 3727$ nebular emission line has been suggested as an alternative SFR indicator (Gallagher et al. 1989; Kennicutt 1992b; Guzman et al. 1997; Barbaro & Poggianti 1997; Jansen et al. 2001; Aragon-Salamanca et al. 2002; Rosa-González et al. 2002; Hopkins et al. 2003; Kewley et al. 2004; Mouhcine et al. 2005). Its intrinsic strength and blue rest-frame wavelength allow it to be measured even in low signal-to-noise (S/N) spectra at $z \lesssim 1.5$ in the optical, and at $2 \lesssim z \lesssim 5.2$ in the near-infrared (Fig. 1). However, the $[O\ II]$ luminosity depends explicitly on the chemical abundance and excitation state of the ionized gas, and suffers a larger amount of dust extinction than $H\alpha$. Therefore, unlike the Balmer recombination lines, $[O\ II]$ is not directly proportional to the SFR and must be calibrated either empirically (Kennicutt 1992b; Rosa-González et al. 2002; Kewley et al. 2004), or theoretically (Barbaro & Poggianti 1997;

¹ Steward Observatory, University of Arizona, 933 N Cherry Ave., Tucson, AZ 85721, USA

² Institute of Astronomy, University of Cambridge, Madingley Road, Cambridge CB3 0HA, United Kingdom

Charlot & Longhetti 2001).

Gallagher et al. (1989) presented the first quantitative analysis of [O II] as a SFR indicator using [O II] and H β measurements of a sample of 75 blue-irregular galaxies. Kennicutt (1992b) improved upon this study by obtaining integrated optical (3650 – 7150 Å) spectra of 55 galaxies spanning the Hubble sequence, including a handful of peculiar objects, and derived the first empirical calibration of [O II] relative to H α . Previously, the equivalent width of [O II] was used only indirectly to infer ongoing star formation (e.g., Broadhurst et al. 1988; Colless et al. 1990; Dressler 1984; Couch & Sharples 1987). Subsequently, Jansen et al. (2001) and Kewley et al. (2004) used the Nearby Field Galaxy Survey (NFGS; Jansen et al. 2000a,b), an imaging and spectrophotometric survey of a representative sample of ~ 200 nearby galaxies, to quantify how variations in reddening and chemical abundance affect the observed [O II] luminosity, and to improve the [O II] SFR calibration. Jansen et al. (2001) showed that the observed [O II]/H α ratio varies by a factor of ~ 7 near M_B^* , predominantly due to variations in dust reddening, and that the [O II]/H α ratio is inversely proportional to galaxy luminosity (see also Carter et al. 2001; Aragon-Salamanca et al. 2002). Comparing the NFGS observations to photoionization models, Kewley et al. (2004) concluded that the [O II]/H α ratio is also strongly dependent on the heavy element abundance and varies weakly with the strength of the ionizing radiation field.

However, all these studies have been based on relatively small samples of optically selected normal galaxies exhibiting modest current-to-past-averaged star-formation rates, normal morphologies, and typical or lower-than-average infrared luminosities. From models of hierarchical galaxy formation (e.g., Somerville & Primack 1999), we anticipate a higher incidence of extreme or bursty star formation at high redshift due to a greater frequency of mergers/interactions and larger reservoirs of neutral gas (e.g., Hammer et al. 2005). Therefore, SFR calibrations based on local samples of normal galaxies may not apply at high redshift.

Large spectrophotometric surveys of the nearby universe such as the Sloan Digital Sky Survey (SDSS; York et al. 2000) provide the opportunity to study the emission-line properties of galaxies with unprecedented statistical precision (e.g., Brinchmann et al. 2004; Tremonti et al. 2004). Hopkins et al. (2003) present a thorough analysis of multi-wavelength SFR diagnostics in the SDSS. However, the fraction of light subtended by the 3'' fiber-optic aperture utilized by the SDSS depends on the distance and intrinsic properties (size, bulge-to-disk ratio, surface-brightness distribution, etc.) of each individual galaxy. For example, in the star-forming galaxy sample studied by Tremonti et al. (2004) the median light fraction is only $\sim 25\%$. Furthermore, the SDSS's strict magnitude-limited selection ($r < 17.7$ mag) targets primarily the most luminous present-day galaxies, which are unlikely to be representative of high-redshift star-forming galaxies. Therefore, empirical SFR calibrations based on SDSS observations should not be applied blindly to distant samples.

As part of a larger effort to characterize the physical properties of star-forming galaxies, we have obtained

high S/N optical spectrophotometry (3600 – 6900 Å at ~ 8 Å FWHM resolution) for a diverse sample of 417 nearby galaxies (Moustakas & Kennicutt 2005a, hereafter MK05). This survey targets objects that represent a small fraction of the galaxy population today, but which may be more typical of high-redshift samples, including starbursts, interacting/merging systems, and dusty, infrared-luminous galaxies; the sample also includes a large number of normal star-forming galaxies. We utilize the long-slit drift-scanning technique developed by Kennicutt (1992a) to obtain spatially integrated spectra at intermediate spectral resolution, which makes our observations well-matched to traditional long-slit spectroscopy of distant galaxies. We supplement our new observations with the NFGS to increase the number of normal galaxies, and to identify any selection biases in our diverse sample of galaxies. In addition, we compare our analysis of optical SFR diagnostics against a sample of $\sim 120,000$ star-forming galaxies from the SDSS in order to assess the effects of statistical incompleteness and aperture bias in our integrated galaxy sample and in the SDSS, respectively.

We use these data to study the [O II] $\lambda 3727$, H β $\lambda 4861$, and [O III] $\lambda 5007$ nebular emission lines as quantitative SFR diagnostics by comparing them against SFRs derived from the extinction-corrected H α luminosity. We also investigate the U -band luminosity as a SFR indicator in an effort to determine whether far-optical broadband photometry offers comparable precision to empirically calibrated emission-line diagnostics for deriving SFRs of distant galaxies. In §2 we present our integrated and SDSS samples. In §3 we explore empirical correlations between optical SFR diagnostics and global properties such as luminosity, dust extinction, and chemical abundance in order to understand the dominant sources of uncertainty that limit the application of these diagnostics. In §4 we derive new empirical SFR calibrations. Finally, §5 we discuss the applicability of our new calibrations to intermediate-redshift galaxy samples, and present our conclusions in §6. To compute distances and absolute magnitudes (always on the Vega system) we adopt $\Omega_0 + \Omega_\Lambda = 1$, $\Omega_0 = 0.3$, and $H_0 = 70 \text{ km s}^{-1} \text{ Mpc}^{-1}$ (Spergel et al. 2003; Freedman et al. 2001). Following convention, we give both emission- and absorption-line equivalent widths as positive numbers in the rest frame-of-reference. Finally, we adopt $12 + \log(\text{O}/\text{H})_\odot = 8.7$ dex as the solar oxygen abundance (Allende Prieto et al. 2001; Holweber 2001).

2. THE DATA

2.1. The Integrated Galaxy Sample

Our integrated galaxy sample consists of our own spectroscopic observations (MK05) and the NFGS (Jansen et al. 2000a,b). We briefly summarize the relevant details of each survey, and refer the reader to the original papers for more information regarding the sample selection and data reductions. The MK05 survey provides high S/N optical (3600 – 6900 Å) spectrophotometry at ~ 8 Å FWHM resolution for 417 nearby galaxies. Based on a variety of internal and external comparisons MK05 find that the relative spectrophotometric precision of the data is $\sim 4\%$. The survey roughly divides into four major subsamples: (1) ~ 125 galaxies

selected from the First Byurakan Survey of UV-excess galaxies (Markarian et al. 1989); (2) ~ 100 infrared-luminous galaxies selected from the IRAS Warm and Bright Galaxy Surveys (Kim et al. 1995; Veilleux et al. 1995, 1999); (3) ~ 35 morphologically selected interacting/merging systems drawn from the Ph. D. thesis sample of Turner (1998); and (4) ~ 130 normal galaxies selected from a volume-limited H α - and UV-imaging survey of the 11 Mpc local volume (R. C. Kennicutt et al., 2006, in preparation), and the Ursa Major cluster (Tully et al. 1996). These samples are intentionally chosen to span the diverse range of galaxies in the local universe with active star formation, both to improve our understanding of galactic star formation and to serve as a more comprehensive reference sample for lookback studies. To provide a more representative, complementary sample of nearby galaxies we turn to the NFGS. The NFGS is a photometric and spectroscopic survey of 196 galaxies selected to reproduce the B -band luminosity function (Jansen et al. 2000a). The wavelength coverage (3600 – 7100 Å), spectral resolution (~ 6 Å FWHM), relative spectrophotometric precision ($\sim 6\%$), and S/N of the NFGS are well-matched to our own observations. Excluding several broad-line AGN and one BL Lac, the combined integrated galaxy sample consists of spectrophotometry for 589 galaxies.

To measure fluxes and equivalent widths of the nebular emission lines we utilize ISPEC1D, a spectral synthesis fitting code described in detail in MK05. Using ISPEC1D we find the non-negative linear combination of population synthesis models (Bruzual & Charlot 2003) that optimally reproduces the observed stellar continuum. Subtracting the model continuum from the data results in a pure nebular emission-line spectrum self-consistently corrected for underlying stellar absorption. We measure the emission-line fluxes and equivalent widths of the strong nebular lines, tabulated in MK05, using simultaneous, multi-Gaussian profile fitting with physically motivated constraints on the intrinsic velocity widths and redshifts of the Balmer and forbidden lines. For consistency we re-measure the emission-line fluxes in the NFGS spectra using ISPEC1D. We find our measurements broadly consistent with Jansen et al. (2000b), except at low equivalent widths where we argue that our technique is more reliable.

To define a sample of star-forming galaxies and to ensure that we can measure reliably the nebular reddening (§3.1), we impose a 3σ S/N cut on the H α and H β emission lines, which removes 28 objects from the integrated sample. We verify that most of these objects are early-type (E/S0) galaxies with effectively zero star formation. However, three galaxies (NGC 1266, UGC 05101, and CGCG 049-057) fail our S/N criterion on H β because they are dusty, infrared-luminous galaxies. All three objects have well-detected H α emission, and in only one do we marginally detect [O II]. Since these galaxies comprise $< 1\%$ of the full integrated sample, and just 4% of objects with $L(\text{IR}) > 10^{11} L_{\odot}$ (§3.2), we do not expect our conclusions to be biased with respect to highly obscured galaxies. However, these types of objects emphasize the need for either H α or infrared observations to ensure a complete census of star formation in galaxies.

We use traditional emission-line diagnostic dia-

grams to differentiate galaxies with nebular emission powered by star formation versus galaxies with an admixture of star formation and AGN activity (Baldwin et al. 1981; Veilleux & Osterbrock 1987; Ho et al. 1997; Kewley et al. 2001a). In Figure 2 we plot the observed [O III]/H β line-ratio as a function of [N II]/H α for the MK05 data (squares) and the NFGS (triangles). For comparison with the integrated line-ratios, we overplot the emission-line sequence traced by individual H II regions (small points) in spiral galaxies (McCall et al. 1985; Zaritsky et al. 1994; van Zee et al. 1998) and dwarf galaxies (Izotov et al. 1994, 1997; Izotov & Thuan 1998). The solid curve in Figure 2 empirically segregates normal star-forming galaxies from AGN based on an analysis of $\sim 10^5$ SDSS galaxies by Kauffmann et al. (2003a). The dashed curve defines the theoretical boundary between AGN and star-forming galaxies presented by Kewley et al. (2001b). We conservatively adopt the Kauffmann et al. (2003a) curve to remove objects with AGN activity, although in §4 we explore the effect of including AGN on our results. Finally, we classify objects without 1σ [O III] $\lambda 5007$ or [N II] $\lambda 6584$ detections as star-forming galaxies using either the condition $\log([\text{N II}]/\text{H}\alpha) < -0.4$ (Tremonti et al. 2004), or using the [S II] $\lambda\lambda 6716, 6731/\text{H}\alpha$ and [O I] $\lambda 6300/\text{H}\alpha$ versus [O III] $\lambda 5007/\text{H}\beta$ diagnostic diagrams and the theoretical boundaries defined by Kewley et al. (2001b). After rejecting another 9 objects that cannot be classified using any of the above methods, our final integrated sample consists of 412 star-forming galaxies.

Figure 2 shows that the sequences formed by H II regions and star-forming galaxies overlap across the full range of emission-line ratios in the [N II]/H α versus [O III]/H β plane (Kennicutt 1992b; Lehnert & Heckman 1994; Kobulnicky et al. 1999; Charlot & Longhetti 2001). Therefore, to first order, techniques developed to analyze the physical properties of individual H II regions may be used to interpret the integrated spectral properties of galaxies (e.g., Kobulnicky et al. 1999; Stasińska & Sodr e 2001; Pilyugin et al. 2004a; Moustakas & Kennicutt 2005b).

In Figure 3 we compare the spectrophotometric properties of the MK05 and NFGS samples. We plot the distributions of the combined sample as dashed, unshaded histograms. We collect B -band photometry for both samples, listed in order of preference, from de Vaucouleurs et al. (1991), LEDA³ (Prugniel & Heraudeau 1998), or by synthesizing photometry directly from the spectra, as described in MK05. These magnitudes have been corrected for foreground Galactic extinction ($R_V = 3.1$; O’Donnell 1994; Schlegel et al. 1998), but not for nebular emission lines or inclination effects since these corrections are challenging or impossible to make at high redshift. Distances for the MK05 sample are based on either primary or secondary measurements when available, or the Mould et al. (2000) multi-attractor linear infall model. Distances for the NFGS sample are based exclusively on the infall model. We assign a fixed 15% uncertainty to objects without a published distance error.

In Figure 3a we plot the B -band luminosity distribu-

³ <http://leda.univ-lyon1.fr>

tions for the MK05 and NFGS samples, using $M_{\odot,B} = +5.42$ mag to convert between $L(B)/L(B)_{\odot}$ and M_B . Despite the significantly different selection criteria, we find the luminosity distributions of the two samples qualitatively similar. The MK05 survey includes a larger number of faint dwarf galaxies ($M_B \gtrsim -16$ mag) and galaxies more luminous than $M_B \simeq -20$ mag relative to the NFGS. The combined distribution, however, is fairly uniform between $M_B \simeq -16$ and -22 mag, and spans the range between ~ -12 mag and ~ -22.5 mag. In Figure 3*b* we plot the distribution of dust extinction at $H\alpha$, $A(H\alpha) = 2.52 E(B-V)$, as determined from the Balmer decrement (§3.1). The median (mean) extinction for the combined sample is 0.51 mag (0.59 ± 0.50 mag), ranging from zero to 2.62 mag in IC 0750, a highly reddened Sab galaxy in the MK05 sample. Figure 3*c* characterizes the metallicity distribution of these samples, using the methodology in §3.4.2 to estimate the gas-phase abundance. The median (mean) metallicity is 8.54 dex (8.50 ± 0.21 dex), and spans the range $7.77 < 12 + \log(O/H) < 8.84$ dex ($0.12 \lesssim Z/Z_{\odot} \lesssim 1.4$). The metallicity distribution of the MK05 sample extends to lower values than the NFGS due to the inclusion of a larger number of low-luminosity galaxies. Finally, in Figure 3*d* we plot the distribution of observed $[O\ III] \lambda 5007/[O\ II] \lambda 3727$ flux ratios for both samples. The $[O\ III]/[O\ II]$ ratio characterizes the hardness of the ionizing radiation field, or the ionization parameter of the photoionized gas (Shields 1990; Kewley & Dopita 2002). In the MK05 sample the median (mean) logarithmic $[O\ III]/[O\ II]$ ratio is -0.33 dex (-0.27 ± 0.32 dex), but spans a factor of ~ 65 in excitation, whereas the NFGS distribution peaks in a narrow range around -0.45 ± 0.20 dex. Although in the local universe low-mass galaxies undergoing a strong burst of star formation typically exhibit the highest $[O\ III]/[O\ II]$ ratios, stronger ionizing radiation fields may be much more common in high-redshift, massive galaxies (e.g., Pettini et al. 2001).

In summary, we find that by combining our survey with the NFGS we achieve wide coverage of the physical parameter space spanned by the $z = 0$ population of star-forming galaxies, from normal galaxies that dominate the mass density, to dwarfs and optical/infrared starbursts that likely dominate at high redshift (e.g., Flores et al. 1999; Hammer et al. 2005; Bell et al. 2005). In §5 we show that the diversity of this sample allows us to construct SFR diagnostics that may be applied at high redshift.

2.2. The SDSS Sample

To complement our sample of galaxies with integrated spectra we culled the SDSS fourth data release (DR4; Adelman-McCarthy 2005) to define a complete sample of nearby star-forming galaxies. We use DR4 galaxies in the SDSS Main Galaxy Sample (Strauss et al. 2002), which have Petrosian r magnitudes between $14.5 < r < 17.77$ mag and r -band Petrosian half-light surface brightnesses $\mu_{50} \leq 24.5$ mag arcsec $^{-2}$ (corrected for foreground Galactic extinction; Schlegel et al. 1998). We only include galaxies having $z > 0.033$ to ensure that $[O\ II] \lambda \lambda 3726, 3729$ lies within the spectral range of the SDSS spectrograph. In addition, we elect to remove galaxies where less than 10% of the r -band light falls in the fiber in order to remove cases of extreme aper-

ture bias, while preserving the approximate magnitude-limited nature of the sample (see also Tremonti et al. 2004). The 10% cut on light fraction removes less than 4% of the sample, whereas a cut at 30% removes over half of the sample and introduces biases which are difficult to quantify. The above requirements result in a parent sample of 360,902 SDSS galaxies.

Emission-line fluxes and equivalent widths for these galaxies have been measured⁴ using a customized continuum fitting code based on the Bruzual & Charlot (2003) populations synthesis models and described by Tremonti et al. (2004) (§2.1). We have compared the results of this code and ISPEC1D and we find excellent agreement among the resulting emission-line flux and equivalent width measurements. To define a sample of star-forming galaxies we impose 3σ detections of the $H\alpha$ and $H\beta$ emission lines, which eliminates $\sim 50\%$ of the parent sample (all early-type), leaving 173,540 emission-line galaxies. Finally, we remove objects contaminated by AGN activity using the methodology described in §2.1, resulting in a sample of 120,846 star-forming galaxies. The mean r -band light fraction for this sample is $25 \pm 9\%$.

In Figure 4 we compare the distributions of spectrophotometric properties for the SDSS and integrated galaxy samples. To facilitate a direct comparison we plot the distributions normalized to the total number of galaxies in each sample. For the SDSS we compute $M_{B,Vega}$ using the Petrosian g_{AB} -band magnitude and $(g-r)_{AB}$ color, and the following relation (M. R. Blanton et al. 2006, in preparation):

$$B_{Vega} = g_{AB} + 0.3915(g-r)_{AB} + 0.087, \quad (1)$$

where the g - and r -band magnitudes have been corrected for foreground Galactic extinction (Schlegel et al. 1998) and k -corrected⁵ to $z = 0$ (Blanton et al. 2003). The standard deviation of the color term in equation (1) is 0.15 mag, which we add in quadrature to the measured photometric uncertainties.

Figure 4*a* shows that the SDSS galaxies provide complete coverage of the bright end of the B -band luminosity distribution, centered on -20.1 mag. By comparison, the integrated sample spans a much broader range in absolute magnitude, uniformly ranging from the most luminous objects in the SDSS to $M_B \simeq -16$ mag, including a handful of $M_B > -16$ mag dwarf galaxies. Throughout our analysis we will attribute many of the differences in physical properties between the integrated and SDSS samples to the different luminosity distributions, although aperture bias in the SDSS observations are also important, as we discuss below.

Figure 4*b* compares the distributions of $A(H\alpha)$ in the SDSS and integrated galaxy samples. The median (mean) extinction in the SDSS is 0.83 mag (0.85 ± 0.41 mag), whereas in the integrated sample $A(H\alpha)$ peaks at zero and decreases almost monotonically to $A(H\alpha) \simeq 2.6$ mag. We attribute the observed differences in these distributions to two effects. First, in the local universe there exists a correlation between luminosity and dust extinction, whereby luminous galaxies contain

⁴ <http://www.mpa-garching.mpg.de/SDSS>

⁵ Using `k-correct` version 4.1.3, which is available at <http://cosmo.nyu.edu/blanton/kcorrect>.

more dust, on average, than less luminous galaxies (§4.1; Buat & Xu 1996; Wang & Heckman 1996; Tully et al. 1998; Adelberger & Steidel 2000; Jansen et al. 2001; Stasińska et al. 2004). Consequently, $A(\text{H}\alpha)$ in the SDSS peaks at higher values both because the mean luminosity of the SDSS sample is larger, and because the SDSS misses less-extincted, lower-luminosity galaxies. In addition, aperture bias in the SDSS may be important. If the centers of spiral galaxies have higher optical depths to dust compared to the optical depth averaged over the whole galaxy (e.g., Valentijn 1994; Jansen et al. 1994), then the mean extinction in a fiber-optic survey of star-forming galaxies will be higher, on average, than the mean extinction of an integrated spectroscopic survey. Kewley et al. (2005), however, find that extinction does not depend on enclosed light fraction based on a comparison of integrated and nuclear spectra in the NFGS.

In Figure 4c we compare the metallicity distributions of the two samples, adopting the empirical abundance calibrations given in §3.4.2. Relative to the integrated galaxy sample, the distribution of oxygen abundances in the SDSS peaks strongly at higher abundance. The median metallicity in the SDSS is $12 + \log(\text{O}/\text{H}) \simeq 8.70$ dex ($Z/Z_{\odot} \simeq 1$), compared to ~ 8.54 dex ($Z/Z_{\odot} \simeq 0.7$) in the integrated sample. We attribute these differences to a combination of two effects: the luminosity-metallicity correlation and aperture effects. Locally, and at high redshift, luminous star-forming galaxies obey a luminosity-metallicity correlation, whereby luminous galaxies are more metal-rich than low-luminosity galaxies (J. Moustakas et al. 2006, in preparation; Skillman et al. 1989; Zaritsky et al. 1994; Richer & McCall 1995; Garnett 2002; Melbourne & Salzer 2002; Tremonti et al. 2004; Kobulnicky et al. 2003; Kobulnicky & Kewley 2004). The median M_B magnitude difference of the two samples is -1.33 mag. Adopting the slope of the B -band luminosity-metallicity correlation found by Tremonti et al. (2004), -0.185 dex mag^{-1} , we predict a median metallicity difference of $+0.25$ dex. This value has the correct sign, and, given all the uncertainties, is roughly consistent with the measured median metallicity difference of $+0.16$ dex. Aperture effects may also drive the SDSS metallicities to higher values, since the centers of spiral galaxies are typically more metal-rich than their outskirts (e.g., McCall et al. 1985; Oey & Kennicutt 1993; Zaritsky et al. 1994; Kennicutt & Garnett 1996; van Zee et al. 1998; Pilyugin et al. 2004b). Tremonti et al. (2004) estimate that aperture bias in the SDSS may lead to an overestimate of the globally averaged metallicity by at least $+0.1$ dex (see also Kewley et al. 2005).

Finally, in Figure 4d we compare the distributions of the observed $[\text{O III}] \lambda 5007/[\text{O II}] \lambda 3727$ ratios in the SDSS and integrated galaxy samples. The median (mean) ionization parameter of the SDSS galaxies is -0.54 dex (-0.52 ± 0.15 dex), lower on average and more narrowly peaked than the distribution of ratios in the integrated galaxy sample. The observed differences are consistent with the higher mean luminosity and metallicity of the SDSS galaxies (Dopita et al. 2000; Kewley et al. 2001a), and with the inclusion of a larger number of extreme starbursts with hard ionizing radiation fields in the integrated galaxy sample.

To summarize, we find significant differences among the SDSS and integrated samples, which is not surprising given the different selection criteria. Although the integrated sample contains $< 1\%$ the number of objects in the SDSS sample, it intentionally spans a broader range of physical properties such as luminosity, metallicity, dust extinction, and ionization. By comparison, the strength of the SDSS sample is its statistical completeness of the bright end of the luminosity function, although aperture bias must be carefully treated. In the following analysis of optical SFR diagnostics we discuss all these effects in detail.

3. ANALYSIS

3.1. Nebular Reddening

To quantify the amount of dust reddening we compute the Balmer decrement, $\text{H}\alpha/\text{H}\beta$, where all the Balmer emission lines have been corrected for underlying stellar absorption as discussed in §2. We define the color excess due to dust reddening, $E(\text{H}\beta\text{-H}\alpha)$, using the relation

$$E(\text{H}\beta\text{-H}\alpha) \equiv -2.5 \log \left[\frac{(\text{H}\alpha/\text{H}\beta)_{\text{int}}}{(\text{H}\alpha/\text{H}\beta)_{\text{obs}}} \right], \quad (2)$$

where $(\text{H}\alpha/\text{H}\beta)_{\text{obs}}$ is the observed decrement and $(\text{H}\alpha/\text{H}\beta)_{\text{int}}$ is the intrinsic Balmer decrement. We assume the case B recombination value $(\text{H}\alpha/\text{H}\beta)_{\text{int}} = 2.86$, which is appropriate for an individual H II region at a typical electron temperature and density (Storey & Hummer 1995). To account for the small variation in $(\text{H}\alpha/\text{H}\beta)_{\text{int}}$ with electron temperature we propagate a 5% systematic uncertainty in $(\text{H}\alpha/\text{H}\beta)_{\text{int}}$ into the total error in $E(\text{H}\beta\text{-H}\alpha)$. To relate $E(\text{H}\beta\text{-H}\alpha)$ to the broad-band color excess, $E(B-V)$, we introduce an attenuation curve, $k(\lambda) \equiv A(\lambda)/E(B-V)$, to obtain the expression

$$E(B-V) \equiv \frac{E(\text{H}\beta\text{-H}\alpha)}{k(\text{H}\beta) - k(\text{H}\alpha)}, \quad (3)$$

where $k(\text{H}\beta)$ and $k(\text{H}\alpha)$ are the values of $k(\lambda)$ at 4861 Å and 6563 Å, respectively (e.g., Calzetti 2001).

In order to de-redden our integrated emission-line fluxes we must assume a functional form for $k(\lambda)$. The most common practice is to neglect radiative transfer effects due to variations in geometry (which, in general, is not a good assumption: Witt et al. 1992; Witt & Gordon 2000), and adopt a Milky Way or LMC/SMC extinction law. Alternatively, Charlot & Fall (2000) advocate a power-law attenuation curve, $k(\lambda) \propto \lambda^{-0.7}$, based on a multi-wavelength analysis of nearby starburst galaxies and simple radiation transfer arguments. Because optical extinction and attenuation curves are similar (unlike in the ultraviolet), we opt for the simplest solution and adopt the O'Donnell (1994) Milky Way extinction curve. Equation (3) then becomes $E(B-V) = 0.874 E(\text{H}\beta\text{-H}\alpha)$.

In §4 we also consider using the $\text{H}\beta/\text{H}\gamma$ Balmer decrement to account for dust extinction, since $\text{H}\gamma \lambda 4340$ is observationally accessible across the same range of redshifts as the emission-line SFR diagnostics considered in this paper (Fig.1). However, obtaining a reliable measurement of $\text{H}\gamma$ is challenging because of its intrinsic weakness and the combined effects of stellar

absorption and dust extinction. In the following, we adopt an intrinsic $H\beta/H\gamma$ ratio of 2.14 assuming an electron temperature of 10,000 K; this ratio varies by just $\pm 3\%$ across a broad range of nebular conditions (Storey & Hummer 1995). Using the O'Donnell (1994) Milky Way extinction curve, the analogous relations to equations (2) and (3) for the $H\beta/H\gamma$ ratio become $E(H\gamma - H\beta) = -2.5 \log(2.14/H\beta/H\gamma)$ and $E(B-V) = 2.05 E(H\gamma - H\beta)$, respectively.

In Figure 5 we compare the reddenings determined using $H\alpha/H\beta$ and $H\beta/H\gamma$ for the MK05 and NFGS samples (squares and triangles with error bars, respectively), and the SDSS (small points without error bars). The *solid* line is the line-of-equality for the two measurements. For this comparison we apply a 7σ S/N cut on $H\gamma$, and we require that $EW(H\beta) > 10 \text{ \AA}$ in emission. We impose this minimum equivalent width because the $H\gamma$ emission-line measurement is very sensitive to the quality of the continuum subtraction. For the SDSS galaxies we find no median systematic offset and a dispersion of 0.15 mag. The $E(B-V)$ measurements based on $H\beta/H\gamma$ for the MK05 and NFGS samples are displaced systematically toward higher reddening by 0.08 and 0.15 mag, respectively, and the residual scatter is significant: 0.22 and 0.38 mag, respectively. We attribute the larger discrepancy between $E(B-V)$ using $H\beta/H\gamma$ and $E(B-V)$ using $H\alpha/H\beta$ in the integrated samples to their lower spectral resolution (~ 8 and $\sim 6 \text{ \AA}$ FWHM, respectively), compared to the SDSS ($\sim 4 \text{ \AA}$). Liang et al. (2004b) discuss in detail the biases inherent to low spectral resolution spectroscopy. Thus, while $H\beta/H\gamma$ offers a direct measurement of the reddening in the absence of $H\alpha$, the errors are formidable ($\gtrsim 50\%$), even in the best case scenario when detailed continuum subtraction can be used and the line S/N and equivalent width are moderately high. Fortunately, at high redshift galaxies are more gas rich and line equivalent widths are generally larger (e.g., Kobulnicky et al. 2003). Thus, using $H\beta/H\gamma$ as a reddening diagnostic in higher-redshift samples may be more reliable (e.g., Flores et al. 2004).

3.2. $H\alpha$ $\lambda 6563$ Star-Formation Rates

The $H\alpha$ $\lambda 6563$ nebular emission line is one of the primary diagnostics used to estimate the SFRs of galaxies in the local universe (Kennicutt 1983, 1992b; Gallego et al. 1995; Kennicutt 1998; Nakamura et al. 2004; Brinchmann et al. 2004). The largest uncertainties affecting $H\alpha$ -based SFRs are due to dust absorption of Lyman-continuum photons within individual H II regions, dust attenuation in the general interstellar medium of the galaxy, and uncertainties in the shape of the initial mass function (Kennicutt 1998). Throughout this paper we adopt the theoretical calibration between the $H\alpha$ luminosity, $L(H\alpha)$, and the SFR, ψ , given by Kennicutt (1998):

$$\psi(H\alpha) = 7.9 \times 10^{-42} \frac{L(H\alpha)}{\text{erg s}^{-1}} \mathcal{M}_{\odot} \text{ yr}^{-1}, \quad (4)$$

where $L(H\alpha)$ has been corrected for underlying stellar absorption and interstellar dust attenuation (see also Kennicutt et al. 1994). This transformation has been computed for solar metallicity, the Salpeter (1955) IMF with lower- and upper-mass cutoffs of 0.1 and $100 \mathcal{M}_{\odot}$,

respectively. Equation (4) also assumes that no Lyman-continuum photons are absorbed by dust, a point that we return to below.

In this paper we adopt the extinction-corrected $H\alpha$ luminosity as our fiducial SFR tracer. However, it is instructive to assess the absolute accuracy of $H\alpha$ as a SFR indicator by comparing it against other independent indicators. Several authors have carried out this exercise using the ultraviolet, infrared, and radio luminosity (Buat & Xu 1996; Cram et al. 1998; Glazebrook et al. 1999; Bell & Kennicutt 2001; Sullivan et al. 2001; Hopkins et al. 2001; Kewley et al. 2002; Buat et al. 2002; Hopkins et al. 2003; Hirashita et al. 2003; Bell 2003). These studies reveal the numerous challenges of deriving absolute SFRs because each indicator is coupled to the true SFR by different physical processes, and they each suffer a variety of systematic uncertainties. Nevertheless, we choose to compare $\psi(H\alpha)$ to the SFR derived from the bolometric infrared luminosity, $L(\text{IR}) \equiv L(8-1000 \mu\text{m})$. The infrared luminosity measures the amount of stellar radiation absorbed and re-emitted by dust grains. Assuming solar metallicity, that the dust re-radiates 100% of the bolometric luminosity, and that star formation has been continuous for the past 10 – 100 Myr, Kennicutt (1998) provides the following transformation given the same IMF used in equation (4):

$$\psi(\text{IR}) = 4.5 \times 10^{-44} \frac{L(\text{IR})}{\text{erg s}^{-1}} \mathcal{M}_{\odot} \text{ yr}^{-1}. \quad (5)$$

The coefficient in equation (5) will be different in galaxies with significant dust heating from old stellar populations, or lower overall dust content (Kennicutt 1998; Bell 2003; Hirashita et al. 2003).

We estimate $L(\text{IR})$ for our integrated galaxy sample using the following procedure. Fluxes from IRAS at 12, 25, 60 and $100 \mu\text{m}$ for our survey have been tabulated by MK05. Ranked in order of preference, these fluxes are from the large optical galaxy catalog (Rice et al. 1988), the IRAS Bright Galaxy Survey (Soifer et al. 1989), or the Faint Source Catalog (Moshir et al. 1990). IRAS fluxes for the NFGS have been gathered from the same references. If no detection is reported at 12 or $25 \mu\text{m}$, we use the empirical ratios (correct to $\pm 30\%$) given in Bell (2003): $S_{\nu}(12 \mu\text{m})/S_{\nu}(100 \mu\text{m}) = 0.0326$ and $S_{\nu}(25 \mu\text{m})/S_{\nu}(60 \mu\text{m}) = 0.131$. We confirm the validity of these ratios for the subset of our sample with detections in all four IRAS bands. To extrapolate the infrared spectral energy distribution beyond $100 \mu\text{m}$, we construct a modified blackbody with dust emissivity proportional to λ^{-1} (Gordon et al. 2000; Bell 2003). We determine the temperature and normalization of the modified blackbody using the $S_{\nu}(60 \mu\text{m})/S_{\nu}(100 \mu\text{m})$ flux ratio for each object. Finally, we integrate numerically between 8 – $1000 \mu\text{m}$ to obtain $L(\text{IR})$. On average, our $L(\text{IR})$ estimates are a factor of 1.84 ± 0.22 (ranging from factors of 1.28 – 3.19) larger than the far-infrared luminosity, $L(\text{FIR}) \equiv L(40-120 \mu\text{m})$ (Helou et al. 1988). We assume a systematic uncertainty of 15% in $L(\text{IR})$ (Bell 2003), which we add in quadrature to the reported IRAS flux uncertainties.

To verify our technique for estimating $L(\text{IR})$, which uses flux measurements in all four IRAS bands, we compare our results against the methods devel-

oped by Dale et al. (2001), Dale & Helou (2002), and Sanders & Mirabel (1996). Dale et al. (2001) present a semi-empirical technique for estimating $L(3-1100 \mu\text{m})$ by arguing that the infrared spectral energy distributions of dusty galaxies can be parameterized in terms of a single parameter, the $S_\nu(60 \mu\text{m})/S_\nu(100 \mu\text{m})$ ratio, which characterizes the relative level of star formation activity in galaxies. Subsequently, Dale & Helou (2002) use new submillimeter observations to show that their original model over-predicts the amount of cold dust emission in quiescent galaxies, and they present an updated semi-empirical relation for deriving $L(3-1100 \mu\text{m})$ based on IRAS fluxes at 25, 60, and 100 μm . Finally, Sanders & Mirabel (1996) present an empirical relation for deriving $L(8-1000 \mu\text{m})$ based on all four IRAS bands. However, because this relation is optimized for luminous- and ultra-luminous infrared galaxies, it tends to over-predict $L(\text{IR})$ in galaxies with a larger amount of cold dust (Dale et al. 2001). With these caveats in mind, we find that our $L(\text{IR})$ values are 19%, 16%, and 7% smaller, respectively, than the three calibrations described above. We attribute part of the difference with the Dale et al. (2001) and Dale & Helou (2002) estimates to the different definitions of $L(\text{IR})$. For example, as much as $\sim 10\%$ of the total infrared energy budget in quiescent systems is emitted at $3-8 \mu\text{m}$ (Dale & Helou 2002, their Table 2). Because we adopt a systematic uncertainty of 15% in our estimate of $L(\text{IR})$, we conclude, therefore, that our results are consistent with these other methods.

In Figure 6 we plot the $\psi(\text{H}\alpha)/\psi(\text{IR})$ ratio against $L(B)$ for our integrated sample, using the observed $\text{H}\alpha$ luminosity in panel (a) and the extinction-corrected $\text{H}\alpha$ luminosity in panel (b). The *solid* line indicates equality of the two SFR measurements. Here and throughout much of our analysis we adopt the B -band luminosity as our preferred independent variable. As we discuss in §4.1, the two dominant sources of scatter in optical SFR diagnostics, dust extinction and metallicity, correlate strongly with $L(B)$. Furthermore, $L(B)$ serves as an observationally convenient surrogate for stellar mass that is available for both our local samples and most high-redshift samples. In panel (b) we also plot the distribution of $S_\nu(60 \mu\text{m})/S_\nu(100 \mu\text{m})$ ratios for the MK05 and NFGS samples, illustrating the higher average level of star formation activity in the MK05 sample.

To first order we find that $\psi(\text{H}\alpha)$ based on the observed $\text{H}\alpha$ luminosity is systematically offset from $\psi(\text{IR})$ by a median (mean) amount -0.27 dex (-0.26 dex), and that the scatter in the ratio is 0.37 dex, or a factor of ~ 2.3 (Fig. 6a). To second order, we observe a strong systematic dependence on $L(B)$ in the sense that $\psi(\text{H}\alpha)/\psi(\text{IR})$ decreases by a factor of ~ 100 over a factor of ~ 3000 increase in $L(B)$. In Figure 6b we show the effect of correcting $\text{H}\alpha$ for extinction using the observed Balmer decrement. The median (mean) systematic difference reduces to 0.00 dex (0.02 dex), and the scatter decreases to 0.22 dex. Moreover, extinction-correcting $\text{H}\alpha$ removes much of the second-order trend seen in panel (a).

Consequently, we find that correcting $\text{H}\alpha$ for extinction using a simple Milky Way extinction curve and the observed Balmer decrement gives $\text{H}\alpha$ SFRs that are consistent with $\psi(\text{IR})$ with a precision of $\pm 70\%$ and no systematic offset, even in many of the most dust-obscured galaxies in our sample (see also Kewley et al. 2002). At

face value, this agreement may seem surprising, given the simple assumptions built into equations (4) and (5). For example, our $\text{H}\alpha$ SFR calibration assumes that none of the Lyman-continuum radiation from massive stars is absorbed by dust. Including this effect, which may be a significant correction (e.g., Inoue et al. 2001), would increase the inferred SFR at a given $\text{H}\alpha$ luminosity. However, the agreement between $\psi(\text{IR})$ and the extinction-corrected $\psi(\text{H}\alpha)$ suggests that Lyman-continuum extinction is not significant for our sample. We note, however, four infrared-luminous galaxies in the MK05 sample (CGCG239-011 W, IRAS 17208-0014, NGC 3628, and UGC 09618 N) which fall significantly below the $\psi(\text{H}\alpha) = \psi(\text{IR})$ line in Figure 6b. Assuming $\psi(\text{IR})$ represents the actual SFR in these objects, the extinction-corrected $\psi(\text{H}\alpha)$ would underestimate the SFR by up to an order-of-magnitude. In addition, $\psi(\text{IR})$ is susceptible to several simplifying assumptions which we have neglected in our comparison. The most important assumption may be that 100% of the bolometric luminosity associated with the current star formation episode is absorbed by dust and re-emitted into the infrared. In fact, at low luminosity ($M_B \gtrsim -19$ mag), we find that $\psi(\text{H}\alpha)/\psi(\text{IR}) > 1$ for our sample in a systematic sense. If the extinction-corrected $\psi(\text{H}\alpha)$ reflects the actual SFR in these objects, then $\psi(\text{IR})$ would under-estimate the SFR by factors of 1.5 – 5.

Clearly, all these effects warrant a more in-depth analysis. However, our emphasis in this paper is to explore rest-frame optical emission-line diagnostics. Consequently, in the remainder of this paper we adopt the $\text{H}\alpha$ luminosity, suitably corrected for stellar absorption and extinction using the observed Balmer decrement, as our fiducial SFR tracer, and we assume equation (4) is the appropriate transformation from luminosity to SFR.

3.3. $\text{H}\beta$ $\lambda 4861$ Star-Formation Rates

Above $z \sim 0.4$, $\text{H}\alpha$ becomes inaccessible to ground-based optical spectrographs. In the search for reliable, self-consistent SFR measurements at all redshifts, the higher-order Balmer lines such as $\text{H}\beta$ offer a promising alternative. The advantages and disadvantages of using $\text{H}\beta$ to measure the SFR were originally discussed by Kennicutt (1992b), who discouraged its use due to the difficulty of accounting for underlying stellar absorption from moderate-resolution spectroscopy of galaxies with $\text{EW}(\text{H}\alpha + [\text{N II}]) \lesssim 50 \text{ \AA}$. However, population synthesis modeling of the stellar continuum ensures accurate removal of the absorption underlying the nebular emission lines (§2; MK05; Tremonti et al. 2004).

As a SFR diagnostic, $\text{H}\beta$, like all the Balmer lines, inherits the same strengths and weaknesses of $\text{H}\alpha$: it is equally sensitive to variations in the IMF and to absorption of Lyman-continuum photons by dust within star-forming regions. In addition, $\text{H}\beta$ suffers more interstellar dust attenuation and is fractionally more sensitive to underlying stellar absorption. For example, assuming that $\text{H}\alpha$ experiences one magnitude of extinction and that stellar absorption is a 20% correction, the observed $\text{H}\beta$ line will be 0.18 times the strength of $\text{H}\alpha$. Despite these uncertainties, when available, $\text{H}\beta$ may be a superior SFR diagnostic than the more commonly used $[\text{O II}] \lambda 3727$ nebular emission line (§3.4).

In Figure 7 we explore the systematic effects of stellar

absorption and dust reddening on $H\beta$ as a precision SFR indicator. This comparison includes all objects having $EW(H\beta) > 5 \text{ \AA}$ in emission. Below this limiting equivalent width, $H\beta$ measurements are very uncertain, even when using population synthesis to subtract the stellar continuum. For reference, in the MK05 and NFGS samples the mean stellar absorption underlying the $H\beta$ emission line is $4.4 \pm 0.6 \text{ \AA}$ and $3.9 \pm 0.5 \text{ \AA}$, respectively.

Figure 7a plots the observed $H\beta/H\alpha$ ratio without corrections for dust reddening or stellar absorption at $H\beta$. The *dashed* line in panels (a) and (b) indicates the intrinsic Balmer decrement, $\log(H\beta/H\alpha)_{\text{int}} = -0.46$ dex (see §3.1). By definition, galaxies whose $H\alpha$ and $H\beta$ fluxes have been corrected for reddening using the $H\alpha/H\beta$ ratio would lie along this line, and $H\beta$ would mirror $H\alpha$ as a star formation tracer. We find that the observed $H\beta/H\alpha$ ratio varies systematically with $L(B)$ due to the combined effects of stellar absorption and reddening, and that the median (mean) ratio is -0.84 dex (-0.86 ± 0.22 dex). In Figure 7b we show the effect of correcting $H\beta$ for underlying stellar absorption. The data shift toward the intrinsic ratio in a luminosity-dependent way because, locally, luminous/massive galaxies have, on average, lower emission-line equivalent widths. The dependence on $L(B)$ becomes less pronounced, the median (mean) ratio increases to -0.53 dex (-0.54 dex), and the scatter reduces to just 0.07 dex. The residual dependence of $(H\beta/H\alpha)_{\text{obs}}$ on $L(B)$ reflects the luminosity-dust correlation, which we discuss in more detail in §4.1. The low scatter in this figure is due to the $H\alpha/H\beta$ ratio’s sensitivity to variations in reddening.

Finally, in Figure 7c we plot the ratio of the observed $H\beta$ luminosity, $L(H\beta)_{\text{obs}}$, corrected for stellar absorption, to $\psi(H\alpha)$, versus $L(B)$. Below $L(B) \lesssim 3 \times 10^9 L(B)_{\odot}$, the median ratio is nearly constant at ~ -0.4 dex, and the scatter ranges from 0.06 to 0.13 dex, or 15 – 35%. Toward higher luminosity, the median ratio decreases progressively (reaching a minimum of ~ -0.9 dex), while the scatter increases systematically from 0.13 dex near $\sim 3 \times 10^9 L(B)_{\odot}$, to 0.20 dex ($\pm 60\%$) at $\sim 10^{11} L(B)_{\odot}$. In §4.2 we parameterize the observed non-linear dependence of $L(H\beta)_{\text{obs}}/\psi(H\alpha)$ on $L(B)$ and discuss it in more detail. Finally, we note that if we do not correct $H\beta$ for stellar absorption in Figure 7c, the trend with luminosity steepens (since the correction is more important for luminous galaxies), the median $H\beta$ SFR conversion factor is $\sim 70\%$ lower, and the scatter increases to 0.36 dex, or $\pm 130\%$. We find that even applying a simple statistical correction of $4 \pm 1 \text{ \AA}$ reduces the scatter in $L(H\beta)_{\text{obs}}/\psi(H\alpha)$ to ~ 0.24 dex, although the systematic trend with blue luminosity remains.

The SDSS sample provides the opportunity to investigate the same empirical correlations explored above using more than two orders-of-magnitude more galaxies. In Figure 8 we plot the $H\beta/H\alpha$ ratio as a function of $L(B)$ for the SDSS. In order to accommodate the large number of data points, each panel displays the logarithm of the number of galaxies in a 100×100 square grid. The trends exhibited by the SDSS galaxies are very similar to those observed in Figure 7 using the integrated sample. Once again, we find that correcting $H\beta$ for stellar absorption reduces both the luminosity dependence and the scatter in the observed $H\alpha/H\beta$ ratio (compare Figs. 8a and 8b). For reference, the mean $H\beta$

absorption correction for the SDSS sample is $2.4 \pm 0.6 \text{ \AA}$. The median $(H\beta/H\alpha)_{\text{obs}}$ ratios in Figures 8a and 8b are systematically lower by 0.07 dex than the corresponding panels in Figure 7 due to the higher mean extinction and near-absence of any galaxies less luminous than $M_B \simeq -18$ mag in the SDSS sample (Fig. 4). Finally, Figure 8c shows the transformation between $L(H\beta)_{\text{obs}}$ and $\psi(H\alpha)$ as a function of $L(B)$. The median conversion factor varies from -0.65 dex around $\sim 3 \times 10^9 L(B)_{\odot}$, to -0.95 dex near $\sim 10^{11} L(B)_{\odot}$, while the dispersion at fixed luminosity is fairly constant at ~ 0.23 dex, or $\pm 70\%$.

In conclusion, we find that both variations in dust reddening and stellar absorption limit the precision of $L(H\beta)_{\text{obs}}$ as a quantitative SFR indicator. Correcting $H\beta$ for underlying stellar absorption either statistically or using population synthesis modeling reduces the uncertainty in $\psi(H\beta)$ substantially and should not be neglected. Finally, we find that dust reddening introduces an average error of 0.1 – 0.25 dex in $\psi(H\beta)$, depending on the luminosity distribution of the sample. In §4.2 we attempt to improve the statistical precision of $L(H\beta)_{\text{obs}}$ as a SFR indicator by parameterizing $L(H\beta)_{\text{obs}}/\psi(H\alpha)$ in terms of $L(B)$.

3.4. [O II] $\lambda 3727$ Star-Formation Rates

As we discuss in §1, the [O II] $\lambda 3727$ nebular emission line is frequently used as a qualitative and quantitative tracer of star formation in galaxies (e.g., Songaila et al. 1994; Hammer et al. 1997; Hogg et al. 1998; Hippelein et al. 2003; Teplitz et al. 2003). SFRs based on [O II], however, are subject to considerable systematic uncertainties due to variations in dust reddening, chemical abundance, and ionization among star-forming galaxies. In this section we explore these systematic effects using empirical correlations in order to understand the limitations of [O II] as a SFR indicator.

3.4.1. Variations in Dust Reddening

We begin our analysis by studying the effects of dust reddening on the [O II]/ $H\alpha$ flux ratio. In Figure 9 we plot [O II]/ $H\alpha$ versus $L(B)$ for the integrated spectroscopic sample. Figure 9a shows the observed [O II]/ $H\alpha$ ratio, $([O II]/H\alpha)_{\text{obs}}$, uncorrected for dust reddening. As shown by Jansen et al. (2001), the observed ratio varies systematically with luminosity in the sense that more luminous galaxies have, on average, lower [O II]/ $H\alpha$ ratios. We find a median (mean) logarithmic ratio of -0.17 dex (-0.21 ± 0.22 dex), corresponding to a linear ratio $([O II]/H\alpha)_{\text{obs}} \simeq 0.68$ and a scatter of $\pm 65\%$. For comparison, Kennicutt (1992b) obtains a median line-ratio of 0.45 ± 0.26 based on a smaller sample of normal luminous galaxies. Figure 9b shows the reddening-corrected [O II]/ $H\alpha$ ratio, $([O II]/H\alpha)_{\text{cor}}$, versus $L(B)$. Correcting both [O II] and $H\alpha$ for dust reddening removes almost all the luminosity dependence seen in panel (a), increases the median (mean) ratio to 0.00 dex (-0.01 dex), and reduces the scatter to 0.12 dex. Consequently, we find that even with an optimal reddening correction (i.e., using $H\alpha/H\beta$), the scatter in [O II]/ $H\alpha$ is $\sim 32\%$, which, in the absence of any other corrections, places a lower limit on the uncertainty in [O II] SFRs. However, if $H\alpha$ were available to make this dust correction then $H\alpha$ should be used in place of [O II] to

derive the SFR. A Spearman rank correlation test on the data in Figure 9b yields a correlation coefficient of -0.18 ; the probability of obtaining this coefficient by chance is $< 1\%$. In §3.4.2 we show that metallicity, which also correlates with luminosity (see §4.1), drives this residual correlation. Finally, in Figure 9c we plot the $L([\text{O II}]_{\text{obs}})/\psi(\text{H}\alpha)$ ratio versus $L(B)$. We find that the median $[\text{O II}]$ SFR transformation varies systematically with blue luminosity, from $0.02 - 0.05$ dex below $3 \times 10^9 L(B)_{\odot}$, to -0.67 dex near $\sim 10^{11} L(B)_{\odot}$. This luminosity dependence is driven by the combined effects of reddening and metallicity, which we discuss in detail below, and parameterize in §4.3. In the absence of any other information, however, SFRs based on the observed $[\text{O II}]$ luminosity are susceptible to a ~ 0.39 dex uncertainty, or a factor of ~ 2.5 .

Figure 10 plots the correlation between $[\text{O II}]/\text{H}\alpha$ and $L(B)$ for the SDSS sample. The mean and median ratios of the SDSS galaxies are systematically lower than the corresponding ratios for the integrated sample (Fig. 9). These differences are partly due to the narrower optical luminosity distribution in the SDSS sample (Fig. 4a): the low-luminosity galaxies in the integrated sample act to elevate the median ratio. However, even at fixed luminosity the distribution of $[\text{O II}]/\text{H}\alpha$ in the SDSS is shifted to lower values. For example, the median (mean) $([\text{O II}]/\text{H}\alpha)_{\text{cor}}$ ratio around $(2 - 5) \times 10^{10} L(B)_{\odot}$ is -0.22 dex (-0.22 ± 0.15 dex), compared to -0.04 dex (-0.06 ± 0.12 dex) in the integrated sample. Finally, comparing Figures 9b and 10b, we find that the reddening correction applied to the SDSS galaxies is much less effective at removing the luminosity dependence of the $[\text{O II}]/\text{H}\alpha$ ratio than for the galaxies with integrated spectroscopy. We explore this point next.

In Figure 11 we show the observed $[\text{O II}]/\text{H}\alpha$ flux ratio as a function of $E(\text{H}\beta\text{-H}\alpha)$ for the integrated sample and the SDSS. Confirming Jansen et al. (2001), we find that $([\text{O II}]/\text{H}\alpha)_{\text{obs}}$ correlates tightly with reddening (see also Aragon-Salamanca et al. 2002; Kewley et al. 2004). In the integrated sample $([\text{O II}]/\text{H}\alpha)_{\text{obs}}$ decreases by an order-of-magnitude over a factor of ~ 2.5 change in $E(\text{H}\beta\text{-H}\alpha)$. Following Jansen et al. (2001), we overplot the predicted reddening at $[\text{O II}]$ and $\text{H}\alpha$ for the O’Donnell (1994) Galactic extinction curve (*solid* line), and the Charlot & Fall (2000) attenuation curve (*dashed* line). Other reddening curves in this wavelength regime (e.g., for the Small Magellanic Cloud; Gordon et al. 2003) are very similar to the two curves plotted. We define the intercept of these curves to be $\log([\text{O II}]/\text{H}\alpha)_{\text{obs}} = 0.0$ dex for the integrated sample, corresponding approximately to the intrinsic (de-reddened) flux ratio of the data (see Fig. 9b). The slope of the relation between $([\text{O II}]/\text{H}\alpha)_{\text{obs}}$ and $E(\text{H}\beta\text{-H}\alpha)$ is remarkably consistent with the expected reduction in flux between 3727 \AA and 6563 \AA due to a simple foreground extinction curve. The SDSS galaxies, by comparison, exhibit a more complex relationship between reddening and observed $[\text{O II}]/\text{H}\alpha$ ratio (Fig. 11, *right*). The *solid* and *dashed* lines show the same two extinction curves described above, this time normalized to $\log([\text{O II}]/\text{H}\alpha)_{\text{obs}} = -0.16$ dex (see Fig. 10c). The SDSS sample exhibits a much larger range in $[\text{O II}]/\text{H}\alpha$ ratio at fixed reddening. Within $E(\text{H}\beta\text{-H}\alpha) = 0.4 \pm 0.05$ mag, the total range in $([\text{O II}]/\text{H}\alpha)_{\text{obs}}$ spans a factor of ~ 11 ,

compared to a factor of ~ 3.5 in the integrated sample. In §3.4.2 we show that these differences arise because the reddening-corrected $[\text{O II}]/\text{H}\alpha$ ratio correlates with oxygen abundance, which affects the SDSS sample to a greater extent.

Before investigating the metallicity sensitivity of $[\text{O II}]$, we turn our attention to an interesting set of outliers in Figure 11 (*left*). In the integrated sample we find galaxies with widely varying $[\text{O II}]/\text{H}\alpha$ ratios, -0.8 dex $\lesssim \log([\text{O II}]/\text{H}\alpha)_{\text{obs}} \lesssim 0.1$ dex, but very little dust reddening, $E(\text{H}\beta\text{-H}\alpha) \lesssim 0.2$ mag. These objects are the low-luminosity, low-metallicity galaxies in our sample, which exhibit low $[\text{O II}]/\text{H}\alpha$ ratios because they are deficient in heavy elements such as oxygen. Although obtaining high-quality spectroscopy of the high-redshift counterparts to these low-luminosity objects is very difficult (see, e.g., §5), their existence indicates that any $[\text{O II}]$ -based SFR calibration must be applied carefully to chemically unevolved objects, which may be much more common at high redshift (e.g., Maier et al. 2005). We do not identify a corresponding branch of extremely low-metallicity galaxies in the SDSS sample, which is consistent with its luminosity distribution and the study by Tremonti et al. (2004).

3.4.2. Variations in Oxygen Abundance

In the preceding analysis we have shown that the observed $[\text{O II}]/\text{H}\alpha$ ratio correlates very tightly with reddening in the integrated sample and less well in the SDSS sample. To investigate this difference and the origin of the residual scatter, we study how variations in metallicity affect the $[\text{O II}]/\text{H}\alpha$ ratio. One widely used abundance indicator is the R_{23} parameter (Pagel et al. 1978), given by

$$R_{23} \equiv \frac{[\text{O II}] \lambda 3727 + [\text{O III}] \lambda \lambda 4959, 5007}{\text{H}\beta \lambda 4861}, \quad (6)$$

where each emission line must be corrected for dust reddening (but see Kobulnicky & Phillips 2003). Observations of H II regions and photoionization modeling reveal that R_{23} depends on the oxygen abundance, although the relationship is not monotonic (Edmunds & Pagel 1984; Skillman 1989; McGaugh 1991; Kobulnicky et al. 1999; Pilyugin 2000, 2001; Kewley & Dopita 2002). In addition, R_{23} depends on the ionization parameter, particularly at low metallicity (e.g., Kobulnicky et al. 1999), and possibly even at high metallicity (Pilyugin 2001). Recent observations have also shown that the theoretical calibration of R_{23} is discrepant by $0.2 - 0.5$ dex relative to electron-temperature abundance measurements, and may require revision to lower abundances (J. Moustakas et al., 2006, in preparation; Pilyugin 2001; Kennicutt et al. 2003; Garnett et al. 2004; Bresolin et al. 2004). Unfortunately, we cannot use R_{23} to probe the metallicity sensitivity of $[\text{O II}]$ because it depends explicitly on the $[\text{O II}]$ intensity. To emphasize this point, we adopt $\text{H}\alpha/\text{H}\beta = 2.86$ as the de-reddened Balmer decrement and rewrite equation (6) as

$$\log \left(\frac{[\text{O II}] \lambda 3727}{\text{H}\alpha} \right) = \log(R_{23}) - \log \left(1 + \frac{[\text{O III}] \lambda \lambda 4959, 5007}{[\text{O II}] \lambda 3727} \right) - \log(2.86). \quad (7)$$

This equation shows that $\log([\text{O II}]/\text{H}\alpha)$ and $\log(R_{23})$ are linearly proportional with a slope of unity and an intercept that depends weakly on the $[\text{O III}]/[\text{O II}]$ ratio. Due to this covariance, therefore, we argue that R_{23} should not be used to quantify the $[\text{O II}]$ metallicity dependence.

Fortunately, there are several other strong-line abundance diagnostics that do not rely on the $[\text{O II}]$ emission-line flux. One such indicator is the $([\text{O III}]/\text{H}\beta)/([\text{N II}]/\text{H}\alpha)$ ratio (Alloin et al. 1979; Pagel et al. 1979; Dutil & Roy 1999; Pettini & Pagel 2004). A recent empirical calibration between $([\text{O III}]/\text{H}\beta)/([\text{N II}]/\text{H}\alpha)$ and the oxygen abundance is given by Pettini & Pagel (2004):

$$12 + \log(\text{O}/\text{H}) = 8.73 - 0.32 \log \left(\frac{[\text{O III}] \lambda 5007 / \text{H}\beta \lambda 4861}{[\text{N II}] \lambda 6584 / \text{H}\alpha \lambda 6563} \right). \quad (8)$$

Equation (8) is only appropriate in the range $-1.0 \lesssim \log \{([\text{O III}]/\text{H}\beta)/([\text{N II}]/\text{H}\alpha)\} \lesssim 1.9$ dex, or $8.12 \lesssim 12 + \log(\text{O}/\text{H}) < 9.05$ dex. Below $12 + \log(\text{O}/\text{H}) \simeq 8.12$ dex, therefore, we adopt an empirical calibration based on the $[\text{N II}] \lambda 6584 / \text{H}\alpha$ ratio (Pettini & Pagel 2004):

$$12 + \log(\text{O}/\text{H}) = 8.9 + 0.59 \log([\text{N II}] \lambda 6584 / \text{H}\alpha). \quad (9)$$

Note that equation (9) should not be applied at high metallicity because $[\text{N II}]/\text{H}\alpha$ converges to an approximately constant value in star-forming galaxies (see, e.g., Fig. 2). Due to their small wavelength separation, both $([\text{O III}]/\text{H}\beta)/([\text{N II}]/\text{H}\alpha)$ and $[\text{N II}]/\text{H}\alpha$ are insensitive to dust reddening, and therefore equations (8) and (9) can be applied to the observed emission-line fluxes.

In Figure 12 we plot the reddening-corrected $[\text{O II}]/\text{H}\alpha$ ratio as a function of oxygen abundance for the integrated sample, H II regions, and the SDSS sample. The H II region comparison is valuable because H II regions span a broader range of $[\text{O II}]/\text{H}\alpha$ flux ratios and abundances relative to both our galaxy samples. Not unexpectedly, we find that $([\text{O II}]/\text{H}\alpha)_{\text{cor}}$ varies with metallicity. Heavy elements, particularly oxygen, are an important source of radiative cooling in H II regions because they have collisionally excited energy levels that are well-populated at $\sim 10,000$ K (Osterbrock 1989). Figure 12, therefore, reflects the behavior of oxygen cooling with metallicity.

In order to characterize the dependence of $[\text{O II}]/\text{H}\alpha$ on oxygen abundance we divide Figure 12 into a metal-poor regime, $12 + \log(\text{O}/\text{H}) < 8.15$ dex, an intermediate-metallicity regime, $8.15 < 12 + \log(\text{O}/\text{H}) < 8.7$ dex, and a metal-rich regime, $12 + \log(\text{O}/\text{H}) > 8.7$ dex. In §3.4.1 we identified the most metal-poor galaxies in the integrated spectroscopic sample as outliers in the correlation between $([\text{O II}]/\text{H}\alpha)_{\text{obs}}$ and dust reddening (Fig. 11, left). In Figure 12 (left) we see that their $([\text{O II}]/\text{H}\alpha)_{\text{cor}}$ ratios obey an almost linear dependence on oxygen abundance, rising by a factor of ~ 5 over a factor of ~ 2.5 increase in metallicity. In the SDSS there are only 57 galaxies in this part of the diagram, all with metallicities around ~ 8.1 dex. In the intermediate-metallicity regime $([\text{O II}]/\text{H}\alpha)_{\text{cor}}$ plateaus to a median (mean) value of 0.04 dex (0.03 ± 0.07 dex) in the integrated sample, and to 0.01 dex (0.00 ± 0.11 dex) in the SDSS. In this

regime we find $\sim 75\%$ of the integrated spectroscopic sample and $\sim 50\%$ of the SDSS galaxies. The weak metallicity dependence and small scatter ($\pm 15 - 35\%$) of the reddening-corrected $[\text{O II}]/\text{H}\alpha$ ratio in the metallicity interval $12 + \log(\text{O}/\text{H}) = 8.15 - 8.7$ dex constitutes one of the principal results of this paper. Finally, above $12 + \log(\text{O}/\text{H}) = 8.7$ dex we find that $([\text{O II}]/\text{H}\alpha)_{\text{cor}}$ decreases by a factor of ~ 1.6 in the integrated sample and by more than a factor of ~ 3 in the SDSS over a very short interval in metallicity, ~ 0.2 dex. In this regime the median (mean) ratio of the integrated sample is -0.13 dex (-0.12 ± 0.11 dex) compared with -0.24 dex (-0.24 ± 0.13 dex) in the SDSS. We conclude, therefore, that correcting $[\text{O II}]/\text{H}\alpha$ for extinction in the SDSS sample (Fig. 10b) marginally decreases the scatter because of the steep metallicity dependence of $([\text{O II}]/\text{H}\alpha)_{\text{cor}}$ for $12 + \log(\text{O}/\text{H}) > 8.7$ dex.

To better understand Figure 12 we turn to photoionization models. Recently, Kewley et al. (2001a) have studied the variation of optical emission-line ratios as a function of metallicity, ionization parameter, ionizing spectral energy distribution, and star-formation history using a large grid of photoionization model calculations. We use these models to plot in Figure 12 the theoretical $[\text{O II}]/\text{H}\alpha$ ratio as a function of oxygen abundance for six values of the ionization parameter, $U \propto (n_e f^2 Q)^{1/3}$, where n_e is the electron density, f is the filling fraction, and Q is the rate of photoionizing photons injected into the gas by massive stars. These theoretical curves have been computed using input spectral energy distributions for evolved star-clusters from STARBURST 99 (Leitherer et al. 1999), which are themselves based on the metallicity-dependent stellar atmospheres from Lejeune et al. (1997) and the Geneva⁶ stellar evolutionary tracks. For this comparison we have adopted the 8 Myr continuous star-formation history models from Kewley et al. (2001a) based on the Salpeter (1955) IMF, evaluated between 0.1 and $120 M_{\odot}$.

We find very good correspondence between the observed and the theoretical metallicity dependence of $[\text{O II}]/\text{H}\alpha$. In the metal-poor regime, the models show that both a reduction in the heavy-element abundance and a hardening of the ionizing radiation field, toward higher values of U , drive the rapid decline in $[\text{O II}]/\text{H}\alpha$. The plateau in the intermediate-metallicity regime, and the subsequent decline in $[\text{O II}]/\text{H}\alpha$ at high metallicity, is due to the increasing importance of nebular cooling via the infrared fine-structure lines and a consequent weakening of the $[\text{O II}]$ line-flux. Finally, according to the models, the scatter in $[\text{O II}]/\text{H}\alpha$ at fixed metallicity arises from differences in ionization parameter. For example, around $12 + \log(\text{O}/\text{H}) = 8.4 \pm 0.1$ dex the total variation in ionization parameter in the integrated sample is a factor of ~ 10 ($-3.8 \lesssim \log U \lesssim -2.9$ dex), which results in the measured $\sim 15\%$ scatter in the observed $[\text{O II}]/\text{H}\alpha$ ratio at fixed metallicity.

3.4.3. Summary of Physical Sources of Scatter in $[\text{O II}]/\text{H}\alpha$

The empirical correlations shown in Figures 9-12 enable us to evaluate the importance of dust extinction, metallicity, and ionization on the $L([\text{O II}]_{\text{obs}})/\psi$ ratio.

⁶ http://obswww.unige.ch/~mowlavi/evol/stev_database.html

Figure 11 shows that dust reddening in the integrated sample accounts for most of the variation in the observed $[\text{O II}]/\text{H}\alpha$ ratio, in accord with the findings of Jansen et al. (2001). However, the same is not true for the SDSS. We reconcile this discrepancy in Figure 12, where we plot the reddening-corrected $[\text{O II}]/\text{H}\alpha$ ratio as a function of metallicity. Both the integrated and SDSS samples map out similar sequences, which agree well with the theoretical models by Kewley et al. (2001a). We find that most of the integrated sample galaxies have metallicities in the range $12 + \log(\text{O}/\text{H}) = 8.15 - 8.7$ dex, where the metallicity dependence of the $[\text{O II}]/\text{H}\alpha$ ratio is weak, while the majority of SDSS galaxies have $12 + \log(\text{O}/\text{H}) > 8.7$ dex, where the correlation becomes steep. Thus, for the SDSS sample, metallicity dominates over reddening as a source of the scatter in the $[\text{O II}]/\text{H}\alpha$ ratio, whereas it is only of minor significance for the less metal-rich integrated sample. We note that galaxies occupy a fairly narrow range in ionization parameter, so this contributes minimally to the observed spread in $[\text{O II}]/\text{H}\alpha$. From a practical standpoint, we are unlikely to measure accurately metallicity, ionization, and dust attenuation at high redshift. Therefore, in §4.3 we focus on the empirical correlation between $L([\text{O II}]_{\text{obs}}/\psi$ and $L(B)$. The well-known correlations between luminosity, metallicity, and reddening (see §4.1), and the wide availability of $L(B)$ measurements of high-redshift galaxies, motivate this choice.

3.5. $[\text{O III}] \lambda 5007$ Star-Formation Rates

Kennicutt (1992b) investigated the $[\text{O III}] \lambda 5007$ nebular emission line as a quantitative SFR diagnostic and concluded that the large dispersion in the $[\text{O III}]/\text{H}\alpha$ ratio among star-forming galaxies precluded its suitability for lookback studies. Nevertheless, the observed $[\text{O III}]$ luminosity, $L([\text{O III}]_{\text{obs}})$, has been used in the literature to estimate a crude SFR (e.g., Teplitz et al. 2000). Therefore, we use our integrated and SDSS spectra of star-forming galaxies to assess the systematic uncertainties in $[\text{O III}]$ -based SFRs.

In Figure 13 we plot the $L([\text{O III}]_{\text{obs}}/\psi(\text{H}\alpha)$ ratio versus $L(B)$ for the integrated sample and the SDSS sample. The median (mean) $L([\text{O III}]_{\text{obs}}/\psi(\text{H}\alpha)$ ratio in the integrated sample is -0.65 dex (-0.68 ± 0.58 dex), or -0.95 dex (-0.94 ± 0.52 dex) if we only consider the most luminous galaxies in our sample ($M_B \lesssim -18.3$ mag). In the SDSS the median (mean) ratio is lower, -1.21 dex (-1.16 ± 0.42 dex), which is consistent with the higher average metallicity of the SDSS galaxies. Variations in excitation and chemical abundance dominate over reddening as physical sources of scatter in the observed $L([\text{O III}]_{\text{obs}}/\psi(\text{H}\alpha)$ ratio. For example, correcting $[\text{O III}]$ for reddening reduces the SFR uncertainty by $\lesssim 15\%$. With no additional corrections, therefore, converting the observed $[\text{O III}]$ luminosity into a SFR is subject to a factor of 3–4 uncertainty (1σ), considerably worse than $\text{H}\beta$ (§3.3), $[\text{O II}]$ (§3.4), or even the U -band luminosity (§3.6).

3.6. U -Band Star-Formation Rates

In the preceding analysis we have focused exclusively on empirically calibrating nebular emission lines as quantitative SFR diagnostics. Here, we consider the U -band luminosity ($\lambda_{\text{eff}} \simeq 3600 \text{ \AA}$) as a SFR indicator. Our

objective is to provide a fiducial for evaluating the efficiency of spectroscopy as a means of deriving galaxy SFRs. Observationally, the U -band continuum is accessible to ground-based spectroscopy at similar redshifts as $[\text{O II}] \lambda 3727$ (Fig. 1). The primary advantage of the U -band over the more commonly used far-UV luminosity ($\lambda\lambda 1250 - 2500 \text{ \AA}$; Kennicutt 1998) as a SFR tracer is that it suffers less dust attenuation. However, the U -band luminosity also depends on the recent star-formation history of the galaxy, and its sensitivity as a SFR indicator may be compromised by evolved ($\gtrsim 100$ Myr) stellar populations (Kennicutt 1998; Cram et al. 1998; Hopkins et al. 2003).

In Figure 14 we plot the U -band-to- $\text{H}\alpha$ luminosity ratio, $L(U)/L(\text{H}\alpha)$, versus $D_n(4000)$, the amplitude of the 4000- \AA break (Balogh et al. 1999; Kauffmann et al. 2003b) for the integrated spectroscopic sample. The 4000- \AA break characterizes the luminosity-weighted age of the stellar population, is relatively insensitive to dust reddening, and depends weakly on stellar metallicity only at ages $\gtrsim 1$ Gyr (Bruzual 1983; Kauffmann et al. 2003b). Here, we utilize $D_n(4000)$ to characterize the effect of intermediate-age and older stellar populations on U -band SFRs. To ensure that $L(U)$ and $L(\text{H}\alpha)$ originate from the same physical region, we synthesize the U -band magnitude directly from our spectra using the Bessell (1990) U -band filter curve and the Lejeune et al. (1997) theoretical spectrum of Vega tied to the Hayes (1985) Vega zero-point. Due to the blue wavelength cutoff of the integrated spectra ($\sim 3600 \text{ \AA}$), we use the best-fitting stellar continuum (§2.1) to extrapolate the data blueward to $\sim 3000 \text{ \AA}$. The error in this extrapolation is significantly smaller than physical sources of scatter in the $L(U)/L(\text{H}\alpha)$ ratio. We adopt a fixed 15% uncertainty in our synthesized U -band magnitudes. Finally, we correct $D_n(4000)$ for nebular emission-line contamination from $[\text{O II}] \lambda 3727$, $[\text{Ne III}] \lambda 3869$, and the high-order Balmer lines, but not the U -band magnitudes.

Figure 14a plots the observed $L(U)/L(\text{H}\alpha)$ luminosity ratio for our integrated sample. We find that $[L(U)/L(\text{H}\alpha)]_{\text{obs}}$ increases systematically by a factor of ~ 2 between $D_n(4000) = 1.1$ and 1.5. We interpret the observed trend as a sequence in star-formation history, from continuous star formation at low values of $L(U)/L(\text{H}\alpha)$ and $D_n(4000)$, to an increasing fraction of old-to-young stellar populations at large values of $L(U)/L(\text{H}\alpha)$ and $D_n(4000)$. At fixed $D_n(4000)$, the typical scatter in $[L(U)/L(\text{H}\alpha)]_{\text{obs}}$ is 0.18 dex, which we attribute to differential reddening. In addition, observations suggest that the stellar continuum experiences a fraction of the dust attenuation suffered by star-forming regions (MK05; Calzetti et al. 1994; Kennicutt et al. 1994; Mayya & Prabhu 1996; Calzetti 1997; Charlot & Fall 2000; Poggianti & Wu 2000; Poggianti et al. 2001; Stasińska & Sodr e 2001; Zaritsky et al. 2002). Therefore, variations in this fraction among the galaxies in our sample contributes additional scatter to the observed $L(U)/L(\text{H}\alpha)$ ratio. Finally, we note that the median (mean) $[L(U)/L(\text{H}\alpha)]_{\text{obs}}$ ratio for the integrated sample is 1.99 dex (1.98 ± 0.24 dex).

In Figure 14b we plot the $L(U)_{\text{obs}}/\psi(\text{H}\alpha)$ ratio versus $D_n(4000)$. Converting $\text{H}\alpha$ to an extinction-corrected SFR flattens the observed trend with $D_n(4000)$ and in-

creases the typical dispersion to 0.33 dex. A Spearman rank test yields a correlation coefficient of 0.09 for these data. The probability of obtaining this correlation by chance is 6%, indicating that variations in star-formation history among the galaxies in our sample contribute systematically to the scatter in $L(U)_{\text{obs}}/\psi(\text{H}\alpha)$, particularly for $D_n(4000) \gtrsim 1.4$. However, at fixed $D_n(4000)$, the typical scatter is 0.31 dex, which accounts for nearly all of the measured dispersion in $L(U)_{\text{obs}}/\psi(\text{H}\alpha)$. We conclude, therefore, that differences in reddening among the galaxies in our sample dominate the factor of ~ 2.1 uncertainty in converting the observed U -band luminosity into a SFR.

Next, in Figure 15 we plot the $L(U)/L(\text{H}\alpha)$ luminosity ratio as a function of $D_n(4000)$ for the SDSS sample. As before, we correct $D_n(4000)$ for emission-line contamination, but not the U -band magnitude. We estimate the U -band magnitude (on the Vega system) from the SDSS u_{AB} -band fiber magnitude (Abazajian et al. 2004) and $(u-g)_{\text{AB}}$ color according to the following relation (M. R. Blanton et al. 2006, in preparation):

$$U_{\text{Vega}} = u_{\text{AB}} - 0.0140(u-g)_{\text{AB}} - 0.841, \quad (10)$$

where the SDSS magnitudes have been corrected for foreground Galactic extinction and k -corrected to $z = 0$ as in §2.2. In this equation the standard deviation of the color term is 0.25 mag, which we add in quadrature to the formal photometric uncertainties.

Using our SDSS sample we confirm in Figure 15 the general trends in $L(U)/L(\text{H}\alpha)$ versus $D_n(4000)$ seen in the integrated galaxy sample. Figure 15*b* demonstrates that variations in dust reddening effectively scramble the observed correlation between $[L(U)/L(\text{H}\alpha)]_{\text{obs}}$ and $D_n(4000)$ (Fig. 15*a*), except at large values of $D_n(4000)$ where an increasing contribution from evolved stellar populations begins to dominate the scatter arising from reddening variations. Neglecting this effect, however, we find that the conversion from $L(U)_{\text{obs}}$ to a SFR in the SDSS sample is approximately constant, and susceptible to an uncertainty of ~ 0.3 dex, or a factor of ~ 2 , comparable to the SFR uncertainty based on the integrated sample.

4. RESULTS

4.1. Empirical Star-Formation Rate Calibrations

In the preceding analysis we have compared the $\text{H}\beta$ $\lambda 4861$, $[\text{O II}]$ $\lambda 3727$, $[\text{O III}]$ $\lambda 5007$, and U -band luminosities against the extinction-corrected $\text{H}\alpha$ luminosity to evaluate their suitability as quantitative SFR diagnostics. We find that dust reddening affects all four diagnostics at some level; it is the dominant source of uncertainty for $\text{H}\beta$ (corrected for stellar absorption) and the U -band. We find that variations in reddening, oxygen abundance, and ionization parameter generate significant scatter in $[\text{O II}]$ as a SFR indicator, although reddening is the dominant effect, at least in the integrated sample. Finally, we find that SFRs based on the $[\text{O III}]$ $\lambda 5007$ line are susceptible to uncertainties that are factors of 2 – 4 higher than any of the other diagnostics considered due to the extreme sensitivity of the $[\text{O III}]$ $\lambda 5007/\text{H}\alpha$ ratio on oxygen abundance and excitation. Consequently we do not discuss $[\text{O III}]$ $\lambda 5007$ as a quantitative SFR indicator any further.

In our analysis we have relied on two highly complementary samples: an integrated spectroscopic sample of 412 galaxies, and 120,846 galaxies drawn from the SDSS. The integrated sample covers the broadest possible range of galaxy luminosity, metallicity, and dust extinction to provide the greatest lever-arm on systematic trends in SFR indicators with these properties. The SDSS galaxies provide a near-complete magnitude-limited sample which is ideal for evaluating the intrinsic dispersion in SFR indicators as a function of galaxy properties. Figures 7-15 show qualitative agreement between the two samples in the systematic trends in SFR diagnostics with luminosity, extinction, and metallicity. However a quantitative comparison reveals differences consistent with the spatial undersampling of the SDSS galaxies. As highlighted in §2.2, the SDSS fiber-spectra sample the central regions of galaxies ($\sim 25\%$ of the total light) which are dustier and more metal rich. The effects of aperture bias are most pronounced on the $[\text{O II}]$ SFR calibration because of its sensitivity to both metallicity and dust. For M_B^* galaxies the $L([\text{O II}]_{\text{obs}})/\psi(\text{H}\alpha)$ ratio is ~ 2 times lower in the SDSS than in our spatially integrated spectra. The net effect is that calibrations derived from the SDSS and applied to spatially unresolved spectra of distant galaxies could be in error by a factor of two. Consequently, we elect to use only the integrated sample to develop quantitative SFR calibrations for high-redshift applications.

To first order, Figures 7*c*, 9*c*, and 14*c* provide the median L_{obs}/ψ conversion factor needed to transform, respectively, the observed $\text{H}\beta$, $[\text{O II}]$, and U -band luminosity into an estimate of the SFR. The scatter in the observed ratios is 70 – 150%. We have demonstrated that each of these conversions depends on some combination of metallicity, dust attenuation, and recent star-formation history. To create precision SFR calibrations, it is desirable to account directly for this dependence on physical properties. However, from a practical standpoint, measuring these properties for high-redshift galaxies is very difficult. To circumvent this shortcoming as much as possible, we choose to parameterize our SFR calibrations as a function of B -band luminosity, $L(B)$. Mounting evidence shows that many galaxy attributes, including metallicity, dust attenuation, and star formation history, correlate strongly with stellar mass (e.g., Tremonti et al. 2004; Kauffmann et al. 2003c; Brinchmann et al. 2004). Blue luminosity is an imperfect surrogate for stellar mass, because star-forming galaxies can exhibit a wide range of mass-to-light ratios (e.g., Bell & de Jong 2001). However, $L(B)$ is a direct observable which is available for our local sample and virtually all intermediate- and high-redshift samples. In Figure 16 we plot the observed correlations between luminosity, dust extinction, and metallicity using the integrated sample, and in §5 we discuss how evolutionary changes in these underlying correlations might impact our locally derived empirical SFR calibrations.

Finally, we consider two other effects on our empirical SFR calibrations. At intermediate redshift, the complete set of emission-line diagnostic diagrams used in §2.1 to remove type 2 AGN from our sample generally are unavailable. Therefore, since AGN are likely to contaminate optical/UV selected samples of distant star-forming galaxies, we consider their distribution and effect on each SFR diagnostic. Furthermore, observations

show that the characteristic infrared luminosity of star-forming galaxies increases as a function of redshift (e.g., Flores et al. 1999; Chary & Elbaz 2001; Hammer et al. 2005; Bell et al. 2005). Consequently, we divide our sample into three broad categories based on infrared luminosity: $L(\text{IR}) > 10^{11} L_{\odot}$; $L(\text{IR}) < 10^{11} L_{\odot}$; and galaxies undetected at either 60 or 100 μm with IRAS (see §3.2). The set of objects without IRAS detections are either bona-fide dust-poor galaxies below IRAS’s sensitivity limits, or individual galaxies in an interacting system that are unresolved by the IRAS beam ($5' \times 2'$ at 60 μm).

4.2. $H\beta$ $\lambda 4861$

Figure 7 and §3.3 demonstrate the importance of accounting for stellar absorption underlying the $H\beta$ nebular emission line. Therefore, in the following section we assume that $H\beta$ has been suitably absorption-corrected, either statistically or using population synthesis modeling of the stellar continuum (e.g., Savaglio et al. 2005). Furthermore, as in §3.3, we only consider objects having $\text{EW}(H\beta) > 5 \text{ \AA}$ in emission to ensure a well-measured $H\beta$ line-flux.

In Figure 17 we plot the $\psi/L(H\beta)_{\text{obs}}$ ratio versus $L(B)$, using various symbols to characterize the infrared luminosity of each galaxy, and the relative positions of AGN and star-forming galaxies. The large open circles with error bars give the median, 25%, and 75% quartile of the $\psi/L(H\beta)_{\text{obs}}$ ratio in 0.5 dex bins of luminosity. Including or excluding AGN has no significant effect on these statistics. In Table 1 we list these quartiles, and the mean, median, and standard deviation of the distribution in each luminosity bin. We recommend interpolating between bins of $L(B)$ to obtain the relevant conversion factor from $L(H\beta)_{\text{obs}}$ to ψ . Minus a constant offset, Figure 17 is equivalent to Figure 16 (*left*) since we use the observed $H\alpha/H\beta$ ratio to estimate the nebular reddening (see §3.1). However, because we are interested in SFRs rather than reddening values, to generate this figure we correct $H\alpha$ for extinction, convert it into a SFR using equation (4), and divide by $L(H\beta)_{\text{obs}}$ to obtain the conversion factor from $L(H\beta)_{\text{obs}}$ to ψ as a function of $L(B)$.

We find that the logarithmic $\psi/L(H\beta)_{\text{obs}}$ ratio increases non-linearly with increasing luminosity, and that the distribution of $\psi/L(H\beta)_{\text{obs}}$ at fixed luminosity is highly asymmetric, particularly above $\sim 3 \times 10^8 L(B)_{\odot}$. This behavior reflects the average increase in the dust content of galaxies of increasing luminosity/mass, and the large variation in dust extinction at fixed luminosity (e.g., Buat & Xu 1996; Wang & Heckman 1996). Infrared-luminous galaxies constitute a large fraction of the most significant outliers, deviating by factors of 1.5 – 3 from the median relation. Finally, the AGN in our sample tend to be optically luminous, and therefore also exhibit a large variation in $\psi/L(H\beta)_{\text{obs}}$, although to first order these AGN exhibit a similar distribution in $\psi/L(H\beta)_{\text{obs}}$ as our star-forming sample. However, since an unknown fraction of the Balmer emission in these objects arises from the nucleus, applying the median SFR conversion factor listed in Table 1 to a sample of AGN may lead to spurious results.

In Figure 18 we compare $\psi(H\beta)$ estimated using two different methods against $\psi(H\alpha)$. In panel (*a*) we correct $L(H\beta)_{\text{obs}}$ for extinction using the measured $H\beta/H\gamma$ ratio, and we apply equation (4) assuming $L(H\beta) =$

$L(H\alpha)/2.86$. As in §3.1, we restrict the sample plotted in Figure 18*a* to objects having $\text{EW}(H\beta) > 10 \text{ \AA}$ in emission and $\text{S/N}(H\gamma) > 7$. We find that $\psi(H\beta)$ computed in this way over-estimates the true SFR by a median (mean) amount 0.12 dex (0.16 dex). The scatter is 0.26 dex, or $\pm 80\%$. As shown in Figure 5 and discussed in §3.1, the measured $H\beta/H\gamma$ ratio in our integrated sample over-estimates systematically the reddening measured from $H\alpha/H\beta$, which leads to the observed systematic in Figure 18*a*. In Figure 18*b* we compare $\psi(H\beta)$ derived using Table 1 (see also Fig. 17) against $\psi(H\alpha)$. We find a median (mean) residual of -0.00 dex (-0.03 ± 0.15 dex). Our empirical calibration, therefore, yields SFRs based on $L(H\beta)_{\text{obs}}$ with a precision of $\pm 40\%$ (1σ), although individual star-forming galaxies deviate from the median relation by up to a factor of ~ 4 . In §5 we test whether these results apply at intermediate redshift.

4.3. $[O \text{ II}] \lambda 3727$

In §3.4 we show that converting $L([O \text{ II}])_{\text{obs}}$ into a SFR is subject to considerable uncertainty. The total range in $\psi/L([O \text{ II}])_{\text{obs}}$ spans more than a factor of ~ 50 with a scatter of a factor of ~ 2.5 . We have shown that this scatter arises from variations in dust reddening, metallicity, and ionization among star-forming galaxies. Here we attempt to account for these systematic effects by deriving an $[O \text{ II}]$ SFR calibration that uses $L(B)$ as the independent variable. The observed correlations between $L(B)$, attenuation, and metallicity (Fig. 16) motivate our empirical $[O \text{ II}]$ SFR calibration. In §5 we discuss how evolutionary changes in the luminosity-dust and luminosity-metallicity correlations at intermediate redshift may affect our results.

In Figure 19 we plot the $\psi/L([O \text{ II}])_{\text{obs}}$ ratio versus $L(B)$ for the AGN and star-forming galaxies in our sample. The large open circles with error bars indicate the median $\psi/L([O \text{ II}])_{\text{obs}}$ ratio in 0.5 dex wide luminosity bins and the 25% and 75% quartiles. In Table 2 we give these statistics, as well as the mean and standard deviation of the data in each bin for the star-forming galaxies. Given a B -band luminosity and an observed $[O \text{ II}]$ luminosity we recommend interpolating the column which gives the median conversion factor to estimate the SFR. Below $\sim 10^9 L(B)_{\odot}$ ($M_B \gtrsim -17$ mag), where reddening effects are negligible, the metallicity distribution of these objects determines the median $\psi/L([O \text{ II}])_{\text{obs}}$ ratio, as we discuss in §3.4.2. With increasing luminosity, the $\psi/L([O \text{ II}])_{\text{obs}}$ ratio increases monotonically because of the combined effects of extinction of metallicity. However, as Figure 12 (*left*) demonstrates, metallicity effects only become important above solar metallicity, $12 + \log(O/H) \simeq 8.7$ dex. Therefore, variations in dust reddening primarily drive this trend in luminosity. Most of the AGN in our sample overlap the sequence traced by star-forming galaxies, although several infrared-luminous AGN deviate by factors of 5 – 15 from the median relation.

In Figure 20 we derive $\psi([O \text{ II}])$ using four different techniques and compare the results against $\psi(H\alpha)$. For this comparison we ensure that the Salpeter IMF defined in §3.2 is used throughout. In Figure 20*a* we compare $\psi(H\alpha)$ against the widely used Kennicutt (1998) $[O \text{ II}]$ SFR calibration, which is an average of the calibrations published by Gallagher et al. (1989) and Kennicutt

(1992b). We find that the Kennicutt (1998) calibration underestimates $\psi([\text{O II}])$ by a median (mean) -0.13 dex (-0.20 dex), and that the scatter in $\psi([\text{O II}])/\psi(\text{H}\alpha)$ is 0.39 dex, or a factor of ~ 2.5 . The residual dependence on $\psi(\text{H}\alpha)$ occurs because Kennicutt (1998) adopt a mean $[\text{O II}]/\text{H}\alpha$ ratio measured from the Kennicutt (1992b) sample, and a constant $A(\text{H}\alpha) = 1$ mag to derive their $\psi([\text{O II}])$ calibration. Our analysis has shown, however, that these are poor approximations given the wide variation in extinction properties among star-forming galaxies.

Next we attempt to correct $L([\text{O II}])_{\text{obs}}$ for dust extinction using the $\text{H}\beta/\text{H}\gamma$ decrement. This panel only includes galaxies satisfying $\text{EW}(\text{H}\beta) > 10 \text{ \AA}$ in emission and $\text{S/N}(\text{H}\gamma) > 7$ (see 3.1). To obtain an estimate of $\psi([\text{O II}])$, we assume a fixed intrinsic flux ratio $[\text{O II}]/\text{H}\alpha = 1$, and apply equation (4). Figure 20b compares $\psi([\text{O II}])$ derived this way against $\psi(\text{H}\alpha)$. We find that $\psi([\text{O II}])$ over-estimates $\psi(\text{H}\alpha)$ by a median (mean) 0.12 dex (0.19 dex), with a scatter of 0.41 dex, or a factor of 2.5. The systematic offset is a direct consequence of the fact that for our sample the $\text{H}\beta/\text{H}\gamma$ ratio tends to over-estimate the reddening derived using $\text{H}\alpha/\text{H}\beta$. To remove the systematic we would have to adopt an intrinsic $[\text{O II}]/\text{H}\alpha$ ratio of 1.3, which is a poor assumption, on average (e.g., Fig. 12, *left*).

In Figure 20c we estimate $\psi([\text{O II}])$ using the methodology developed by Kewley et al. (2004), and plot the results against $\psi(\text{H}\alpha)$. For this comparison we follow the recommended, six-step method outlined in §6.1 of their paper. First, we derive the reddening-corrected $[\text{O II}]$ luminosity using their equation (18), and apply their equation (16) to estimate $E(B-V)$. Next, we compute the reddening-corrected R_{23} ratio and apply it to their equation (11) to determine the oxygen abundance, $12 + \log(\text{O}/\text{H})$. Kewley et al. (2004) recommend the Zaritsky et al. (1994) R_{23} abundance calibration. Finally, armed with an estimate of the metallicity for each galaxy, we apply their equation (10) to obtain the reddening- and abundance-corrected $\psi([\text{O II}])$. The results of our comparison do not change if we instead utilize their theoretical $\psi([\text{O II}])$ calibration [their equation (15)]. We find a median (mean) residual of 0.10 dex (0.08 dex) and a scatter of 0.33 dex between their $\psi([\text{O II}])$ and $\psi(\text{H}\alpha)$. This technique removes much of the systematic dependence on $\psi(\text{H}\alpha)$ seen in panel (a) because they use a luminosity-dependent extinction correction. However, as these authors emphasize, the applicability of this empirical reddening correlation has not been tested on high-redshift samples. Finally, we note that their methodology relies on measuring at least three nebular emission lines, $[\text{O II}]$, $[\text{O III}]$, and $\text{H}\beta$. In this case, we recommend using $\text{H}\beta$ to estimate the SFR since it provides a more reliable measurement of the SFR than $[\text{O II}]$ (see §4.2).

Finally, Figure 20d compares $\psi(\text{H}\alpha)$ against our empirical calibration of $\psi([\text{O II}])$ using the median conversion factors in Table 2 (see also Fig. 19). We find a median (mean) residual systematic of 0.02 dex (-0.02 dex) and a scatter of 0.28 dex, or $\pm 90\%$. Although this method for deriving $\psi([\text{O II}])$ should be applied carefully to individual galaxies, which deviate by up to a factor ~ 10 from the mean relation, our calibration should be useful

for computing the statistical star formation properties of sufficiently large galaxy samples.

4.4. *U-band*

In §3.6 we studied the relative effects of dust reddening and the presence of evolved stellar populations on the *U*-band luminosity as a quantitative SFR indicator. We found that reddening variations dominate the systematic uncertainty in $L(U)_{\text{obs}}$ as a SFR indicator across a wide range of star-formation histories and luminosity-weighted ages, as characterized by the 4000-Å break. From the median and standard deviation of the data in Figure 14b we derive the following *U*-band SFR calibration:

$$\psi(U) = (1.4 \pm 1.1) \times 10^{-43} \frac{L(U)_{\text{obs}}}{\text{erg s}^{-1}} \mathcal{M}_{\odot} \text{ yr}^{-1}. \quad (11)$$

This calibration is difficult to compare with previous results because for the first time it has been derived empirically using the extinction-corrected $\text{H}\alpha$ luminosity. Equation (11) implicitly includes the effects of dust attenuation so that it can be applied to high-redshift samples without spectroscopic information. Cram et al. (1998) derive an approximate *U*-band SFR calibration by bootstrapping the far-UV (2500 Å) calibration from Cowie et al. (1997) to $\sim 3600 \text{ \AA}$ neglecting dust reddening and assuming extended, continuous star formation. This extrapolation is subject to considerable uncertainty given the potentially large variation in star-formation histories among galaxies, and the significant effects of dust reddening. Hopkins et al. (2003) present an empirical *u*-band SFR calibration for the SDSS, roughly corrected for aperture bias, using the radio (1.4 GHz) luminosity as their fiducial SFR tracer (Bell 2003). However, this calibration also requires *u*-band luminosities that have been corrected for dust attenuation.

Although we experimented with a second-order *U*-band SFR calibration parameterized in terms of $L(B)$, we conclude that the significant scatter in $\psi/L(U)_{\text{obs}}$ does not justify such a calibration. However, for high-redshift surveys that target the bright end of the optical luminosity function, we provide the median transformation from $L(U)_{\text{obs}}$ to SFR for galaxies brighter than $\sim 3 \times 10^9 L(B)_{\odot}$ ($M_B \lesssim -18.3$ mag):

$$\psi(U) = (1.8 \pm 1.0) \times 10^{-43} \frac{L(U)_{\text{obs}}}{\text{erg s}^{-1}} \mathcal{M}_{\odot} \text{ yr}^{-1}. \quad (12)$$

5. APPLICATIONS AT INTERMEDIATE REDSHIFT

In this paper we have developed a set of empirical SFR calibrations for the $\text{H}\beta$ and $[\text{O II}]$ nebular emission lines, and for the *U*-band luminosity. However, these calibrations are built on empirical correlations obeyed by star-forming galaxies in the local universe (e.g., Fig. 16) that must be tested at intermediate and high redshift. For example, the luminosity-metallicity correlation has been shown to evolve in a mass-dependent way by $z \sim 1$ (J. Moustakas et al., 2006, in preparation; Lilly et al. 2003; Kobulnicky et al. 2003; Kobulnicky & Kewley 2004; Liang et al. 2004a; Maier et al. 2004, 2005; Savaglio et al. 2005; Shapley et al. 2005). Therefore, it is crucial to quantify how evolutionary changes in galaxy

properties as a function of redshift might affect our locally derived SFR calibrations.

Testing our local calibrations requires a complete set of optical emission-line measurements, including $H\alpha$, $H\beta$, $[O\ III]$, and $[O\ II]$, of a statistically significant sample of intermediate-redshift galaxies spanning a broad range of luminosity or stellar mass. In practice, obtaining all these nebular diagnostics for individual high-redshift galaxies is extremely challenging. Nevertheless, several intermediate-redshift samples recently have become available that facilitate some simple comparisons. Where necessary, we convert absolute magnitudes to our adopted cosmology and onto the Vega system assuming $B_{AB} - B_{Vega} = -0.09$ mag (M. R. Blanton et al. 2006, in preparation).

First we assess whether the luminosity-dust correlation holds at intermediate redshift by plotting the observed $H\alpha/H\beta$ ratio versus $L(B)$ in Figure 21. For this comparison we use different symbols to distinguish starburst galaxies from AGN in our local sample. We compile the relevant intermediate-redshift flux measurements from Maier et al. (2005), Shapley et al. (2005), Savaglio et al. (2005), and Liang et al. (2004a) for star-forming galaxies at a median redshift 0.7, 1.4, 0.9, and 0.7, respectively. Maier et al. (2005) and Shapley et al. (2005) measure $H\alpha$ and $H\beta$ in their respective intermediate-redshift samples, while Savaglio et al. (2005) and Liang et al. (2004a) only measure $H\beta$ and $H\gamma$. Therefore, to include the data from the latter two samples in this comparison, we use the observed $H\beta/H\gamma$ ratio to predict the reddened $H\alpha/H\beta$ ratio assuming case B recombination and the O'Donnell (1994) extinction curve. The *solid* line in Figure 21 indicates the intrinsic $H\alpha/H\beta$ ratio. The $H\alpha/H\beta$ ratio of every object below this line is unphysical, either due to measurement error or uncertainties in the stellar absorption correction. Stellar absorption corrections to the Balmer lines of the intermediate-redshift galaxies have been applied either statistically, or are negligible due to large emission-line equivalent widths.

Overall, we find qualitative agreement between the local and the intermediate-redshift luminosity-dust relation. As expected, most of the intermediate-redshift galaxies overlap the bright end of the local relation, where galaxies experience the highest dust attenuation, on average. Several of the Maier et al. (2005) galaxies and two of the objects from Shapley et al. (2005) have $H\alpha/H\beta$ ratios that are consistent with zero reddening. We find, however, that nearly half the Liang et al. (2004a) sample and several galaxies from the other samples have $\log(H\alpha/H\beta)_{obs} \gtrsim 0.8$ dex. The amount of reddening implied by this Balmer decrement, $E(B-V) \gtrsim 0.8$ mag, assuming the optical Milky Way extinction curve applies at intermediate redshift, is larger than any value measured in our local sample of star-forming galaxies. We postulate three possibilities to explain the position of these galaxies relative to the local sample: (1) they are AGN; (2) measurement uncertainties; or (3) a substantial fraction of intermediate-redshift star-forming galaxies are dustier than the most highly obscured nearby galaxies in our sample.

To explore the possibility that these objects host AGN we note the position of one highly obscured AGN in the MK05 sample, IC 1623 B. The reddening implied by this object's $H\alpha/H\beta$ ratio, $E(B-V) \simeq 1.5$ mag, is

larger than any of the intermediate-redshift galaxies. Although we do not have a measurement of IC 1623 B's infrared luminosity, from its highly reddened optical continuum (MK05) and large Balmer decrement we infer that it must be significant. Therefore, the intermediate-redshift galaxies with the largest $H\alpha/H\beta$ ratios may be highly obscured galaxies hosting an AGN. On the basis of their $[N\ II]/H\alpha$ ratios and the Kewley et al. (2001b) classification scheme (e.g., Fig. 2), all the objects studied by Maier et al. (2005) and Shapley et al. (2005) are star-forming galaxies. However, adopting the Kauffmann et al. (2003a) empirical boundary we would re-classify as an AGN one of the Maier et al. (2005) galaxies with $\log(H\alpha/H\beta)_{obs} > 0.8$ dex. An additional 5 galaxies from Maier et al. (2005) and 2 from Shapley et al. (2005) with $\log(H\alpha/H\beta)_{obs} < 0.8$ dex are AGN on the basis of the Kauffmann et al. (2003a) classification scheme. Consequently, without additional $[N\ II]/H\alpha$ measurements for these samples we cannot exclude the hypothesis that some of these objects are AGN.

Alternatively, measurement errors may explain the position of at least some of the intermediate-redshift galaxies with Balmer decrements in excess of what we observe in our $z \sim 0$ sample. The Balmer decrements of the Savaglio et al. (2005) and Liang et al. (2004a) galaxies, in particular, are consistent (within the errors) with having been drawn from the distribution of local galaxies. However, all four intermediate-redshift samples have at least one galaxy with $\log(H\alpha/H\beta)_{obs} > 0.8$ dex. Therefore, we conclude that measurement error cannot explain the position of *all* the intermediate-redshift galaxies on this diagram.

Finally, we consider that intermediate-redshift star-forming galaxies may experience more dust obscuration than any of the galaxies in our local galaxy sample. For example, 75% of the galaxies from Liang et al. (2004a) have $L(IR) > 10^{11} L_{\odot}$ because they were selected on the basis of their 15 μm flux. We note, however, that the MK05 sample includes ~ 100 infrared-selected galaxies and a handful of ultra-luminous infrared galaxies (ULIRGs; $L(IR) > 10^{12} L_{\odot}$; Sanders & Mirabel 1996). Adopting a standard Milky Way extinction curve, the Balmer decrements of the most obscured intermediate-redshift galaxies imply V -band optical depths of 2 – 4. For comparison, a V -band optical depth of unity corresponds to $H\alpha/H\beta = 4.1$ (O'Donnell 1994). Different dust geometries other than the assumed screen model (e.g., Calzetti 2001) would underestimate the true extinction since the observed nebular emission lines are always weighted toward the lines-of-sight with the lowest obscuration (e.g., Witt et al. 1992; Calzetti et al. 1994; Witt & Gordon 2000). Finally, from a multi-wavelength analysis of distant galaxies, Flores et al. (1999) estimate that the global extinction at $z < 1$ is in the range $E(B-V) = 0.15 - 0.3$ mag, and that highly obscured star-forming galaxies constitute $< 1\%$ of galaxies up to $z = 1$. If, however, high-redshift star-forming galaxies typically suffer $E(B-V) > 0.8$ mag of dust reddening, then the empirical $H\beta$ SFR calibration developed in §4.2 would systematically underestimate the true SFR by a factor of 1.5 – 3. In summary, some combination of the possibilities outlined above may result in the displacement of intermediate-redshift galaxies to larger $H\alpha/H\beta$ ratios than our local sample. A more detailed compari-

son awaits $H\alpha$, $[N\ II]$, and $H\beta$ measurements for a larger number of intermediate- and high-redshift galaxies.

Next we test the evolution in the observed $[O\ II]/H\alpha$ ratio as a function of $L(B)$ between $z \sim 0$ and $z \sim 1$. In Figure 22 we plot measurements presented by Maier et al. (2005), Tresse et al. (2002), Hicks et al. (2002), and Glazebrook et al. (1999) for galaxies at median redshifts 0.7, 0.7, 1.1, and 0.8, respectively. For the Glazebrook et al. (1999) sample we obtain $L(B)$ from Hammer et al. (1997). Based on this comparison we find that the local $[O\ II]/H\alpha$ - $L(B)$ relation for star-forming galaxies qualitatively holds at intermediate redshift. Nearly all of the intermediate-redshift points overlap with the bright end of the nearby galaxy $[O\ II]/H\alpha$ sequence. Several of the Maier et al. (2005) galaxies and one of the objects from Tresse et al. (2002) have $([O\ II]/H\alpha)_{\text{obs}} > 1$, which is higher than any nearby star-forming galaxy at the same luminosity. The position of these galaxies contradicts the expectation that they are either highly extinguished, or have extremely low or high oxygen abundances (Fig. 12). However, several AGN in our local sample exhibit similarly enhanced $[O\ II]/H\alpha$ ratios, which suggests qualitatively that these intermediate-redshift galaxies harbor an active nucleus. At the other extreme, we find a handful of objects with significantly lower $[O\ II]/H\alpha$ ratios than we observe in our local sample. The most severely discrepant points are from the study by Hicks et al. (2002) of $H\alpha$ -selected galaxies (McCarthy et al. 1999) at $z = 0.8 - 1.5$. Hicks et al. (2002) discuss in detail the displacement of their galaxies to lower $[O\ II]/H\alpha$ ratios than observed locally, and conclude that they must be experiencing up to $E(B-V) = 0.6$ mag more reddening. Alternatively, these objects may be metal-rich ($Z > Z_{\odot}$) and have ionization parameters that are an order-of-magnitude higher than nearby star-forming galaxies of comparable luminosity (e.g., Fig. 12). If the low $[O\ II]/H\alpha$ ratios exhibited by the Hicks et al. (2002) sample are typical for intermediate- and high-redshift galaxies then the empirical SFR calibration presented in §4.3 may systematically underestimate the true SFR by a factor of 3 – 10.

In Figure 23 we compare the ionization properties of nearby and intermediate-redshift galaxies by plotting the observed $[O\ III]/[O\ II]$ ratio versus $L(B)$. We take the observed oxygen emission-line measurements for galaxies at median redshifts of 0.7, 0.8, 0.7, and 0.7 from Maier et al. (2005), Savaglio et al. (2005), Liang et al. (2004a), and Lilly et al. (2003), respectively. We note that $E(B-V) = 0.3$ mag of reddening increases an object’s observed $[O\ III]/[O\ II]$ ratio by 0.14 dex on this plot. To indicate roughly how $[O\ III]/[O\ II]$ translates into a measure of the ionization parameter, $\log U$, we use the Kewley et al. (2001a) photoionization models for starburst galaxies assuming solar metallicity. We find that the ionization properties of the intermediate-redshift galaxies are broadly consistent with local star-forming galaxies. Several of the intermediate-redshift points from Liang et al. (2004a) and Lilly et al. (2003) exhibit higher ionization parameters than the typical galaxy in our local sample, although both AGN contamination and reddening may enhance the observed $[O\ III]/[O\ II]$ ratio. The average ionization parameter of the intermediate-redshift galaxies may be slightly higher than locally, although at present we do not consider this difference significant

given the systematic effects of reddening.

To summarize, we find that the excitation, metal abundance, and dust attenuation properties of our local sample of star-forming galaxies are broadly consistent with galaxies at $z \sim 1$, although individual intermediate-redshift galaxies may deviate significantly from the median spectral sequences defined locally. A more in-depth comparison of the physical properties of high-redshift galaxies awaits measurements of the complete set of rest-frame optical emission-line diagnostics, from $H\alpha$ to $[O\ II]$, for larger samples of distant galaxies.

6. CONCLUSIONS

We have used integrated optical spectrophotometry for 412 star-forming galaxies at $z \sim 0$, and fiber-aperture spectrophotometry for 120,846 SDSS galaxies at $z \sim 0.1$, to investigate the $H\alpha$ $\lambda 6563$, $H\beta$ $\lambda 4861$, $[O\ II]$ $\lambda 3727$, and $[O\ III]$ $\lambda 5007$ nebular emission lines and the U -band luminosity as quantitative SFR indicators. The integrated sample enables us to study SFR diagnostics across the broadest possible range in optical/infrared luminosity, metallicity, dust extinction, and excitation. A comparison dataset drawn from the SDSS provides a near-complete magnitude-limited sample which is ideal for evaluating the intrinsic dispersion in SFR indicators.

We find that the $H\alpha$ luminosity, when corrected for dust extinction using the $H\alpha/H\beta$ Balmer decrement and the O’Donnell Milky Way extinction curve, reliably measures the SFR even in highly obscured infrared galaxies. The precisions of the observed $H\beta$, $[O\ II]$, and U -band luminosities as SFR diagnostics are limited to factors of ~ 1.7 , ~ 2.5 , and ~ 2.1 , respectively, because of variations in dust reddening among star-forming galaxies. Correcting $H\beta$ for underlying stellar absorption, even statistically, improves its precision as a SFR indicator significantly. The reddening-corrected $[O\ II]/H\alpha$ ratio depends weakly on changes in metallicity over a wide range in oxygen abundance, $12 + \log(O/H) = 8.15 - 8.7$ dex ($Z/Z_{\odot} = 0.3 - 1.0$). In this metallicity interval we find that galaxies occupy a narrow range in ionization parameter ($-3.8 \lesssim \log U \lesssim -2.9$ dex). By contrast, below $12 + \log(O/H) = 8.15$ dex and above $12 + \log(O/H) = 8.7$ dex, this ratio depends steeply on oxygen abundance. We find that the scatter in $[O\ III]$ $\lambda 5007$ as a SFR indicator is a factor of 3 – 4 due to its sensitivity to oxygen abundance and ionization, considerably worse than any of the other empirical diagnostics considered. Finally, our analysis reveals that dust reddening dominates the systematic uncertainty in the U -band luminosity as a SFR tracer over variations in star-formation history among the galaxies in our sample.

Through a quantitative comparison of optical emission-line diagnostics from integrated and fiber-aperture spectrophotometry, we conclude that SFR calibrations derived from SDSS observations and applied to spatially unresolved spectra of distant galaxies are susceptible to a factor of ~ 2 systematic uncertainty due to spatial undersampling (aperture bias) in the SDSS spectrophotometry. We develop empirical SFR calibrations for $H\beta$ and $[O\ II]$ parameterized in terms of the B -band luminosity, motivated by the observed correlations between luminosity, dust reddening, and oxygen abundance obeyed by local galaxies. These calibrations remove the luminosity-dependent systematic bias in $H\beta$ and $[O\ II]$ SFRs and re-

duce the scatter to $\pm 40\%$ and $\pm 90\%$, respectively. However, individual galaxies may deviate by up to a factor of ~ 4 and ~ 10 from the median $H\beta$ and $[O\ II]$ SFR calibrations, respectively. Finally, we compare the relations between luminosity and reddening, ionization, and $[O\ II]/H\alpha$ ratio for our local, $z \sim 0$ galaxies to those of galaxies observed at $z \sim 1$ and find broad agreement, although some intermediate-redshift galaxies may be more dust-obscured than any of the star-forming galaxies in our local sample. We conclude that optical emission-line measurements for larger samples of intermediate- and high-redshift galaxies are needed to test the applicability of our locally derived empirical SFR calibrations to distant galaxies.

The authors would like to thank the anonymous referee for comments that improved the clarity of the paper. J. M. would also like to acknowledge conversations with Daniel Eisenstein, Janice Lee, Amy Stutz, and Dennis Zaritsky on various aspects of the paper. The data analysis for this project relied heavily on IDL routines written by David Schlegel, Scott Burles, and Doug Finkbeiner, and on the IDL Astronomy User's Library, which is main-

tained by Wayne Landsman at the Goddard Space Flight Center. Funding for this project has been provided by NSF grant AST-0307386, NASA grant NAG5-8326, and a SINGS grant, provided by NASA through JPL contract 1224769. Funding for the creation and distribution of the SDSS Archive has been provided by the Alfred P. Sloan Foundation, the Participating Institutions, the National Aeronautics and Space Administration, the National Science Foundation, the U.S. Department of Energy, the Japanese Monbukagakusho, and the Max Planck Society. The SDSS Web site is <http://www.sdss.org>. The SDSS is managed by the Astrophysical Research Consortium (ARC) for the Participating Institutions. The Participating Institutions are The University of Chicago, Fermilab, the Institute for Advanced Study, the Japan Participation Group, The Johns Hopkins University, the Korean Scientist Group, Los Alamos National Laboratory, the Max-Planck-Institute for Astronomy (MPIA), the Max-Planck-Institute for Astrophysics (MPA), New Mexico State University, University of Pittsburgh, University of Portsmouth, Princeton University, the United States Naval Observatory, and the University of Washington.

REFERENCES

- Abazajian, K., et al. 2004, *AJ*, 128, 502
 Adelberger, K. L., & Steidel, C. C. 2000, *ApJ*, 544, 218
 Adelman-McCarthy, J. K. 2005, *ArXiv Astrophysics e-prints*
 Allende Prieto, C., Lambert, D. L., & Asplund, M. 2001, *ApJ*, 556, L63
 Alloin, D., Collin-Souffrin, S., Joly, M., & Vigroux, L. 1979, *A&A*, 78, 200
 Aragon-Salamanca, A., Alonso-Herrero, A., Gallego, J., Garcia-Dabo, C. E., Perez-Gonzalez, P. G., Zamorano, J., & de Paz, A. G. 2002, *ArXiv Astrophysics e-prints*
 Baldwin, J. A., Phillips, M. M., & Terlevich, R. 1981, *PASP*, 93, 5
 Balogh, M. L., Morris, S. L., Yee, H. K. C., Carlberg, R. G., & Ellingson, E. 1999, *ApJ*, 527, 54
 Barbaro, G., & Poggianti, B. M. 1997, *A&A*, 324, 490
 Bell, E. F. 2003, *ApJ*, 586, 794
 Bell, E. F., & de Jong, R. S. 2001, *ApJ*, 550, 212
 Bell, E. F., & Kennicutt, R. C. 2001, *ApJ*, 548, 681
 Bell, E. F., Papovich, C., Wolf, C., Le Floc'h, E., Caldwell, J. A. R., Barden, M., Egami, E., McIntosh, D. H., Meisenheimer, K., Pérez-González, P. G., Rieke, G. H., Rieke, M. J., Rigby, J. R., & Rix, H. 2005, *ApJ*, 625, 23
 Bessell, M. S. 1990, *PASP*, 102, 1181
 Blanton, M. R., Brinkmann, J., Csabai, I., Doi, M., Eisenstein, D., Fukugita, M., Gunn, J. E., Hogg, D. W., & Schlegel, D. J. 2003, *AJ*, 125, 2348
 Bresolin, F., Garnett, D. R., & Kennicutt, R. C. 2004, *ApJ*, 615, 228
 Brinchmann, J., Charlot, S., White, S. D. M., Tremonti, C., Kauffmann, G., Heckman, T., & Brinkmann, J. 2004, *MNRAS*, 351, 1151
 Broadhurst, T. J., Ellis, R. S., & Shanks, T. 1988, *MNRAS*, 235, 827
 Bruzual, G. 1983, *ApJ*, 273, 105
 Bruzual, G., & Charlot, S. 2003, *MNRAS*, 344, 1000
 Buat, V., Boselli, A., Gavazzi, G., & Bonfanti, C. 2002, *A&A*, 383, 801
 Buat, V., Deharveng, J. M., & Donas, J. 1989, *A&A*, 223, 42
 Buat, V., & Xu, C. 1996, *A&A*, 306, 61
 Calzetti, D. 1997, in *American Institute of Physics Conference Series*, 403+
 Calzetti, D. 2001, *PASP*, 113, 1449
 Calzetti, D., Kinney, A. L., & Storchi-Bergmann, T. 1994, *ApJ*, 429, 582
 Carter, B. J., Fabricant, D. G., Geller, M. J., Kurtz, M. J., & McLean, B. 2001, *ApJ*, 559, 606
 Charlot, S., & Fall, S. M. 2000, *ApJ*, 539, 718
 Charlot, S., & Longhetti, M. 2001, *MNRAS*, 323, 887
 Charlot, S., Kauffmann, G., Longhetti, M., Tresse, L., White, S. D. M., Maddox, S. J., & Fall, S. M. 2002, *MNRAS*, 330, 876
 Chary, R., & Elbaz, D. 2001, *ApJ*, 556, 562
 Colless, M., Ellis, R. S., Taylor, K., & Hook, R. N. 1990, *MNRAS*, 244, 408
 Condon, J. J. 1992, *ARA&A*, 30, 575
 Couch, W. J., & Sharples, R. M. 1987, *MNRAS*, 229, 423
 Cowie, L. L., Hu, E. M., Songaila, A., & Egami, E. 1997, *ApJ*, 481, L9+
 Cram, L., Hopkins, A., Mobasher, B., & Rowan-Robinson, M. 1998, *ApJ*, 507, 155
 Dale, D. A., & Helou, G. 2002, *ApJ*, 576, 159
 Dale, D. A., Helou, G., Contursi, A., Silbermann, N. A., & Kolhatkar, S. 2001, *ApJ*, 549, 215
 David, L. P., Jones, C., & Forman, W. 1992, *ApJ*, 388, 82
 de Vaucouleurs, G., de Vaucouleurs, A., Corwin, H. G., Buta, R. J., Paturel, G., & Fouque, P. 1991, *Third Reference Catalogue of Bright Galaxies (Volume 1-3, XII, 2069 pp. 7 figs.)*. Springer-Verlag Berlin Heidelberg New York
 Dopita, M. A., Kewley, L. J., Heisler, C. A., & Sutherland, R. S. 2000, *ApJ*, 542, 224
 Dressler, A. 1984, *ARA&A*, 22, 185
 Dutil, Y., & Roy, J. 1999, *ApJ*, 516, 62
 Edmunds, M. G., & Pagel, B. E. J. 1984, *MNRAS*, 211, 507
 Flores, H., Hammer, F., Elbaz, D., Cesarsky, C. J., Liang, Y. C., Fadda, D., & Gruel, N. 2004, *A&A*, 415, 885
 Flores, H., Hammer, F., Thuan, T. X., Césarsky, C., Desert, F. X., Omont, A., Lilly, S. J., Eales, S., Crampton, D., & Le Fèvre, O. 1999, *ApJ*, 517, 148
 Freedman, W. L., Madore, B. F., Gibson, B. K., Ferrarese, L., Kelson, D. D., Sakai, S., Mould, J. R., Kennicutt, R. C., Ford, H. C., Graham, J. A., Huchra, J. P., Hughes, S. M. G., Illingworth, G. D., Macri, L. M., & Stetson, P. B. 2001, *ApJ*, 553, 47
 Gallagher, J. S., Hunter, D. A., & Bushouse, H. 1989, *AJ*, 97, 700
 Gallego, J., Zamorano, J., Aragon-Salamanca, A., & Rego, M. 1995, *ApJ*, 455, L1+
 Garnett, D. R. 2002, *ApJ*, 581, 1019
 Garnett, D. R., Kennicutt, R. C., & Bresolin, F. 2004, *ApJ*, 607, L21
 Glazebrook, K., Blake, C., Economou, F., Lilly, S., & Colless, M. 1999, *MNRAS*, 306, 843
 Gordon, K. D., Clayton, G. C., Misselt, K. A., Landolt, A. U., & Wolff, M. J. 2003, *ApJ*, 594, 279
 Gordon, K. D., Clayton, G. C., Witt, A. N., & Misselt, K. A. 2000, *ApJ*, 533, 236

- Guzman, R., Gallego, J., Koo, D. C., Phillips, A. C., Lowenthal, J. D., Faber, S. M., Illingworth, G. D., & Vogt, N. P. 1997, *ApJ*, 489, 559
- Hammer, F., Flores, H., Elbaz, D., Zheng, X. Z., Liang, Y. C., & Cesarsky, C. 2005, *A&A*, 430, 115
- Hammer, F., Flores, H., Lilly, S. J., Crampton, D., Le Fevre, O., Rola, C., Mallen-Ornelas, G., Schade, D., et al. 1997, *ApJ*, 481, 49
- Hayes, D. S. 1985, in *IAU Symp. 111: Calibration of Fundamental Stellar Quantities*, 225–249
- Helou, G., Khan, I. R., Malek, L., & Boehmer, L. 1988, *ApJS*, 68, 151
- Hicks, E. K. S., Malkan, M. A., Teplitz, H. I., McCarthy, P. J., & Yan, L. 2002, *ApJ*, 581, 205
- Hippelein, H., Maier, C., Meisenheimer, K., Wolf, C., Fried, J. W., von Kuhlmann, B., Kümmel, M., Phleps, S., & Röser, H.-J. 2003, *A&A*, 402, 65
- Hirashita, H., Buat, V., & Inoue, A. K. 2003, *A&A*, 410, 83
- Ho, L. C., Filippenko, A. V., & Sargent, W. L. W. 1997, *ApJS*, 112, 315
- Hogg, D. W., Cohen, J. G., Blandford, R., & Pahre, M. A. 1998, *ApJ*, 504, 622
- Holweger, H. 2001, in *AIP Conf. Proc. 598: Joint SOHO/ACE workshop "Solar and Galactic Composition"*, 23–
- Hopkins, A. M. 2004, *ApJ*, 615, 209
- Hopkins, A. M., Connolly, A. J., Haarsma, D. B., & Cram, L. E. 2001, *AJ*, 122, 288
- Hopkins, A. M., Miller, C. J., Nichol, R. C., Connolly, A. J., Bernardi, M., Gómez, P. L., Goto, T., Tremonti, C. A., et al. 2003, *ApJ*, 599, 971
- Inoue, A. K., Hirashita, H., & Kamaya, H. 2001, *ApJ*, 555, 613
- Izotov, Y. I., & Thuan, T. X. 1998, *ApJ*, 500, 188
- Izotov, Y. I., Thuan, T. X., & Lipovetsky, V. A. 1994, *ApJ*, 435, 647
- . 1997, *ApJS*, 108, 1
- Jansen, R. A., Fabricant, D., Franx, M., & Caldwell, N. 2000a, *ApJS*, 126, 331
- Jansen, R. A., Franx, M., & Fabricant, D. 2001, *ApJ*, 551, 825
- Jansen, R. A., Franx, M., Fabricant, D., & Caldwell, N. 2000b, *ApJS*, 126, 271
- Jansen, R. A., Knapen, J. H., Beckman, J. E., Peletier, R. F., & Hes, R. 1994, *MNRAS*, 270, 373
- Kauffmann, G., Heckman, T. M., Tremonti, C., Brinchmann, J., Charlot, S., White, S. D. M., Ridgway, S. E., Brinkmann, J., et al. 2003a, *MNRAS*, 346, 1055
- Kauffmann, G., Heckman, T. M., White, S. D. M., Charlot, S., Tremonti, C., Brinchmann, J., Bruzual, G., Peng, E. W., et al. 2003b, *MNRAS*, 341, 33
- Kauffmann, G., Heckman, T. M., White, S. D. M., Charlot, S., Tremonti, C., Peng, E. W., Seibert, M., Brinkmann, J., et al. 2003c, *MNRAS*, 341, 54
- Kennicutt, R. C. 1983, *ApJ*, 272, 54
- . 1992a, *ApJS*, 79, 255
- . 1992b, *ApJ*, 388, 310
- . 1998, *ARA&A*, 36, 189
- Kennicutt, R. C., Bresolin, F., & Garnett, D. R. 2003, *ApJ*, 591, 801
- Kennicutt, R. C., & Garnett, D. R. 1996, *ApJ*, 456, 504
- Kennicutt, R. C., Tamblyn, P., & Congdon, C. E. 1994, *ApJ*, 435, 22
- Kewley, L. J., & Dopita, M. A. 2002, *ApJS*, 142, 35
- Kewley, L. J., Dopita, M. A., Sutherland, R. S., Heisler, C. A., & Trevena, J. 2001a, *ApJ*, 556, 121
- Kewley, L. J., Geller, M. J., & Jansen, R. A. 2004, *AJ*, 127, 2002
- Kewley, L. J., Geller, M. J., Jansen, R. A., & Dopita, M. A. 2002, *AJ*, 124, 3135
- Kewley, L. J., Heisler, C. A., Dopita, M. A., & Lumsden, S. 2001b, *ApJS*, 132, 37
- Kewley, L. J., Jansen, R. A., & Geller, M. J. 2005, *PASP*, 117, 227
- Kim, D.-C., Sanders, D. B., Veilleux, S., Mazzarella, J. M., & Soifer, B. T. 1995, *ApJS*, 98, 129
- Kobulnicky, H. A., Kennicutt, R. C., & Pizagno, J. L. 1999, *ApJ*, 514, 544
- Kobulnicky, H. A., & Kewley, L. J. 2004, *ArXiv Astrophysics e-prints*
- Kobulnicky, H. A., & Phillips, A. C. 2003, *ApJ*, 599, 1031
- Kobulnicky, H. A., Willmer, C. N. A., Phillips, A. C., Koo, D. C., Faber, S. M., Weiner, B. J., Sarajedini, V. L., Simard, L., et al. 2003, *ApJ*, 599, 1006
- Lehnert, M. D., & Heckman, T. M. 1994, *ApJ*, 426, L27
- Leitherer, C., Schaerer, D., Goldader, J. D., Delgado, R. M. G., Robert, C., Kune, D. F., de Mello, D. F., Devost, D., et al. 1999, *ApJS*, 123, 3
- Lejeune, T., Cuisinier, F., & Buser, R. 1997, *A&AS*, 125, 229
- Liang, Y. C., Hammer, F., Flores, H., Elbaz, D., Marcillac, D., & Cesarsky, C. J. 2004a, *A&A*, 423, 867
- Liang, Y. C., Hammer, F., Flores, H., Gruel, N., & Assémat, F. 2004b, *A&A*, 417, 905
- Lilly, S. J., Carollo, C. M., & Stockton, A. N. 2003, *ApJ*, 597, 730
- Lilly, S. J., Le Fevre, O., Hammer, F., & Crampton, D. 1996, *ApJ*, 460, L1+
- Madau, P., Ferguson, H. C., Dickinson, M. E., Giavalisco, M., Steidel, C. C., & Fruchter, A. 1996, *MNRAS*, 283, 1388
- Maier, C., Lilly, S. J., Carollo, M., Stockton, A., & Brodwin, M. 2005, *ArXiv Astrophysics e-prints*
- Maier, C., Meisenheimer, K., & Hippelein, H. 2004, *A&A*, 418, 475
- Markarian, B. E., Lipovetsky, V. A., Stepanian, J. A., Erastova, L. K., & Shapovalova, A. I. 1989, *Soobshcheniya Spetsial'noj Astrofizicheskoy Observatorii*, 62, 5
- Mayya, Y. D., & Prabhu, T. P. 1996, *AJ*, 111, 1252
- McCall, M. L., Rybski, P. M., & Shields, G. A. 1985, *ApJS*, 57, 1
- McCarthy, P. J., Yan, L., Freudling, W., Teplitz, H. I., Malumuth, E. M., Weymann, R. J., Malkan, M. A., Fosbury, R. A. E., Gardner, J. P., Storrie-Lombardi, L. J., Thompson, R. I., Williams, R. E., & Heap, S. R. 1999, *ApJ*, 520, 548
- McGaugh, S. S. 1991, *ApJ*, 380, 140
- Melbourne, J., & Salzer, J. J. 2002, *AJ*, 123, 2302
- Moshir, M., Kopan, G., Conrow, T., McCallon, H., Hacking, P., Gregorich, D., Rohrbach, G., Melnyk, M., et al. 1990, *BAAS*, 22, 1325
- Mouhcine, M., Lewis, I., Jones, B., Lamareille, F., Maddox, S. J., & Contini, T. 2005, *MNRAS*, 362, 1143
- Mould, J. R., Huchra, J. P., Freedman, W. L., Kennicutt, R. C., Ferrarese, L., Ford, H. C., Gibson, B. K., Graham, J. A., et al. 2000, *ApJ*, 529, 786
- Moustakas, J., & Kennicutt, R. C. 2005a, *ApJS*, in press (astro-ph/0511729)
- . 2005b, *ApJ*, submitted (astro-ph/0511730)
- Nakamura, O., Fukugita, M., Brinkmann, J., & Schneider, D. P. 2004, *AJ*, 127, 2511
- O'Donnell, J. E. 1994, *ApJ*, 422, 158
- Oey, M. S., & Kennicutt, R. C. 1993, *ApJ*, 411, 137
- Osterbrock, D. E. 1989, *Astrophysics of gaseous nebulae and active galactic nuclei* (Research supported by the University of California, John Simon Guggenheim Memorial Foundation, University of Minnesota, et al. Mill Valley, CA, University Science Books, 1989, 422 p.)
- Pagel, B. E. J., Edmunds, M. G., Blackwell, D. E., Chun, M. S., & Smith, G. 1979, *MNRAS*, 189, 95
- Pagel, B. E. J., Edmunds, M. G., Fosbury, R. A. E., & Webster, B. L. 1978, *MNRAS*, 184, 569
- Pettini, M., & Pagel, B. E. J. 2004, *MNRAS*, 348, L59
- Pettini, M., Shapley, A. E., Steidel, C. C., Cuby, J., Dickinson, M., Moorwood, A. F. M., Adelberger, K. L., & Giavalisco, M. 2001, *ApJ*, 554, 981
- Pilyugin, L. S. 2000, *A&A*, 362, 325
- . 2001, *A&A*, 369, 594
- Pilyugin, L. S., Contini, T., & Vilchez, J. M. 2004a, *A&A*, 423, 427
- Pilyugin, L. S., Vilchez, J. M., & Contini, T. 2004b, *A&A*, 425, 849
- Poggianti, B. M., Bressan, A., & Franceschini, A. 2001, *ApJ*, 550, 195
- Poggianti, B. M., & Wu, H. 2000, *ApJ*, 529, 157
- Prugniel, P., & Heraudeau, P. 1998, *A&AS*, 128, 299
- Rice, W., Lonsdale, C. J., Soifer, B. T., Neugebauer, G., Koplan, E. L., Lloyd, L. A., de Jong, T., & Habing, H. J. 1988, *ApJS*, 68, 91
- Richer, M. G., & McCall, M. L. 1995, *ApJ*, 445, 642
- Rosa-González, D., Terlevich, E., & Terlevich, R. 2002, *MNRAS*, 332, 283
- Salpeter, E. E. 1955, *ApJ*, 121, 161
- Sanders, D. B., & Mirabel, I. F. 1996, *ARA&A*, 34, 749

- Savaglio, S., Glazebrook, K., Le Borgne, D., Juneau, S., Abraham, R., Chen, H. ., Crampton, D., McCarthy, P., Carlberg, R., Marzke, R., Roth, K., Jorgensen, I., & Murowinski, R. 2005, *ArXiv Astrophysics e-prints*
- Schlegel, D. J., Finkbeiner, D. P., & Davis, M. 1998, *ApJ*, 500, 525
- Shapley, A. E., Coil, A., Ma, C.-P., & Bundy, K. 2005, *ArXiv Astrophysics e-prints*
- Shields, G. A. 1990, *ARA&A*, 28, 525
- Skillman, E. D. 1989, *ApJ*, 347, 883
- Skillman, E. D., Kennicutt, R. C., & Hodge, P. W. 1989, *ApJ*, 347, 875
- Soifer, B. T., Boehmer, L., Neugebauer, G., & Sanders, D. B. 1989, *AJ*, 98, 766
- Somerville, R. S., & Primack, J. R. 1999, *MNRAS*, 310, 1087
- Songaila, A., Cowie, L. L., Hu, E. M., & Gardner, J. P. 1994, *ApJS*, 94, 461
- Spergel, D. N., Verde, L., Peiris, H. V., Komatsu, E., Nolta, M. R., Bennett, C. L., Halpern, M., Hinshaw, G., Jarosik, N., Kogut, A., Limon, M., Meyer, S. S., Page, L., Tucker, G. S., Weiland, J. L., Wollack, E., & Wright, E. L. 2003, *ApJS*, 148, 175
- Stasińska, G., Mateus, A., Sodr e, L., & Szczerba, R. 2004, *A&A*, 420, 475
- Stasińska, G., & Sodr e, L. 2001, *A&A*, 374, 919
- Steidel, C. C., Adelberger, K. L., Giavalisco, M., Dickinson, M., & Pettini, M. 1999, *ApJ*, 519, 1
- Storey, P. J., & Hummer, D. G. 1995, *MNRAS*, 272, 41
- Strauss, M. A., Weinberg, D. H., Lupton, R. H., Narayanan, V. K., Annis, J., Bernardi, M., Blanton, M., Burles, S., et al. 2002, *AJ*, 124, 1810
- Sullivan, M., Mobasher, B., Chan, B., Cram, L., Ellis, R., Treyer, M., & Hopkins, A. 2001, *ApJ*, 558, 72
- Teplitz, H. I., Collins, N. R., Gardner, J. P., Hill, R. S., & Rhodes, J. 2003, *ApJ*, 589, 704
- Teplitz, H. I., Malkan, M. A., Steidel, C. C., McLean, I. S., Becklin, E. E., Figer, D. F., Gilbert, A. M., Graham, J. R., Larkin, J. E., Levenson, N. A., & Wilcox, M. K. 2000, *ApJ*, 542, 18
- Tremonti, C. A., Heckman, T. M., Kauffmann, G., Brinchmann, J., Charlot, S., White, S. D. M., Seibert, M., Peng, E. W., et al. 2004, *ApJ*, 613, 898
- Tresse, L., Maddox, S. J., Le F evre, O., & Cuby, J.-G. 2002, *MNRAS*, 337, 369
- Tully, R. B., Pierce, M. J., Huang, J., Saunders, W., Verheijen, M. A. W., & Witchalls, P. L. 1998, *AJ*, 115, 2264
- Tully, R. B., Verheijen, M. A. W., Pierce, M. J., Huang, J., & Wainscoat, R. J. 1996, *AJ*, 112, 2471
- Turner, A. M. 1998, Ph.D. Thesis
- Valentijn, E. A. 1994, *MNRAS*, 266, 614
- van Zee, L., Salzer, J. J., Haynes, M. P., O'Donoghue, A. A., & Balonek, T. J. 1998, *AJ*, 116, 2805
- Veilleux, S., Kim, D.-C., & Sanders, D. B. 1999, *ApJ*, 522, 113
- Veilleux, S., Kim, D.-C., Sanders, D. B., Mazzarella, J. M., & Soifer, B. T. 1995, *ApJS*, 98, 171
- Veilleux, S., & Osterbrock, D. E. 1987, *ApJS*, 63, 295
- Wang, B., & Heckman, T. M. 1996, *ApJ*, 457, 645
- Witt, A. N., & Gordon, K. D. 2000, *ApJ*, 528, 799
- Witt, A. N., Thronson, H. A., & Capuano, J. M. 1992, *ApJ*, 393, 611
- York, D. G., et al. 2000, *AJ*, 120, 1579
- Zaritsky, D., Harris, J., Thompson, I. B., Grebel, E. K., & Massey, P. 2002, *AJ*, 123, 855
- Zaritsky, D., Kennicutt, R. C., & Huchra, J. P. 1994, *ApJ*, 420, 87

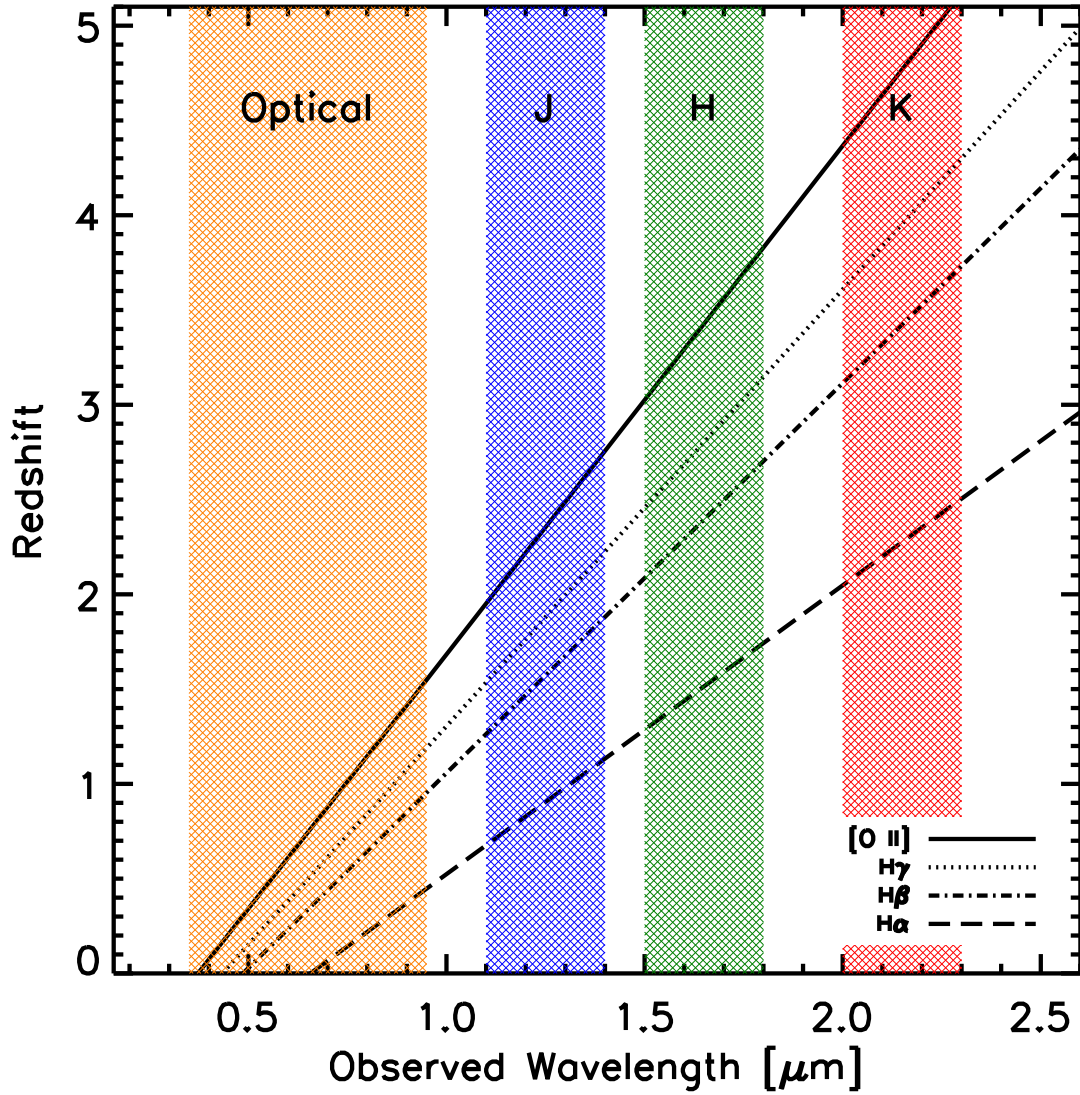


FIG. 1.— Diagram illustrating the redshifts at which $H\alpha$ $\lambda 6563$, $H\beta$ $\lambda 4861$, $H\gamma$ $\lambda 4340$, and $[O II]$ $\lambda 3727$ are observable from the ground in the optical (3500 – 9500 Å) and through the JHK near-infrared atmospheric windows.

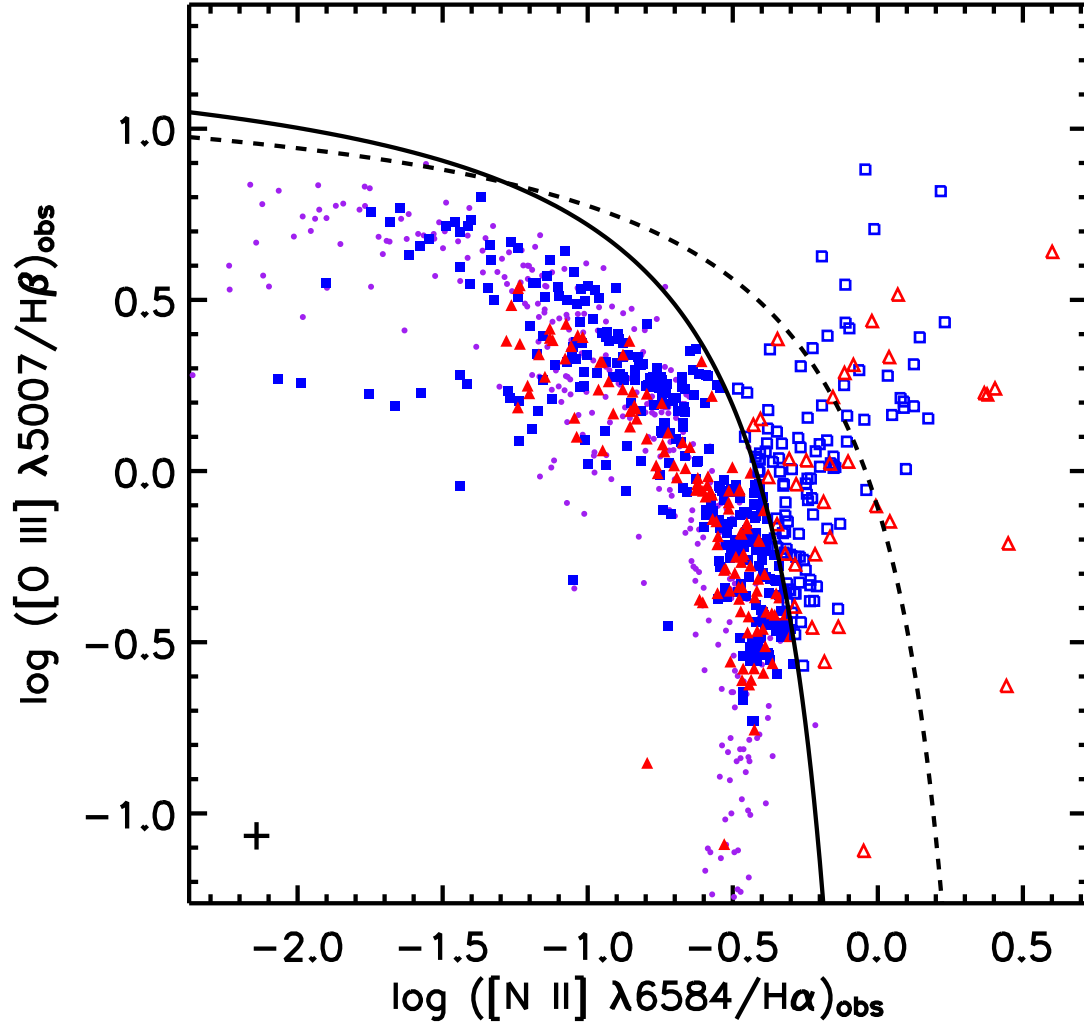


FIG. 2.— Emission-line diagnostic diagram showing the observed $([\text{O III}] \lambda 5007 / \text{H}\beta)_{\text{obs}}$ flux ratio versus $([\text{N II}] \lambda 6584 / \text{H}\alpha)_{\text{obs}}$ for the MK05 survey (squares), the NFGS (triangles), and individual H II regions (small points). (Each sample has been colored blue, red, and purple, respectively, in the electronic edition of the journal). We classify objects into star-forming galaxies (filled symbols) and AGN (open symbols) using the *solid* curve defined empirically by Kauffmann et al. (2003a). For comparison the *dashed* line shows the theoretical division between star-forming galaxies and galaxies with AGN activity obtained by Kewley et al. (2001b). We plot the average uncertainty in the data as a cross in the lower-left part of the diagram.

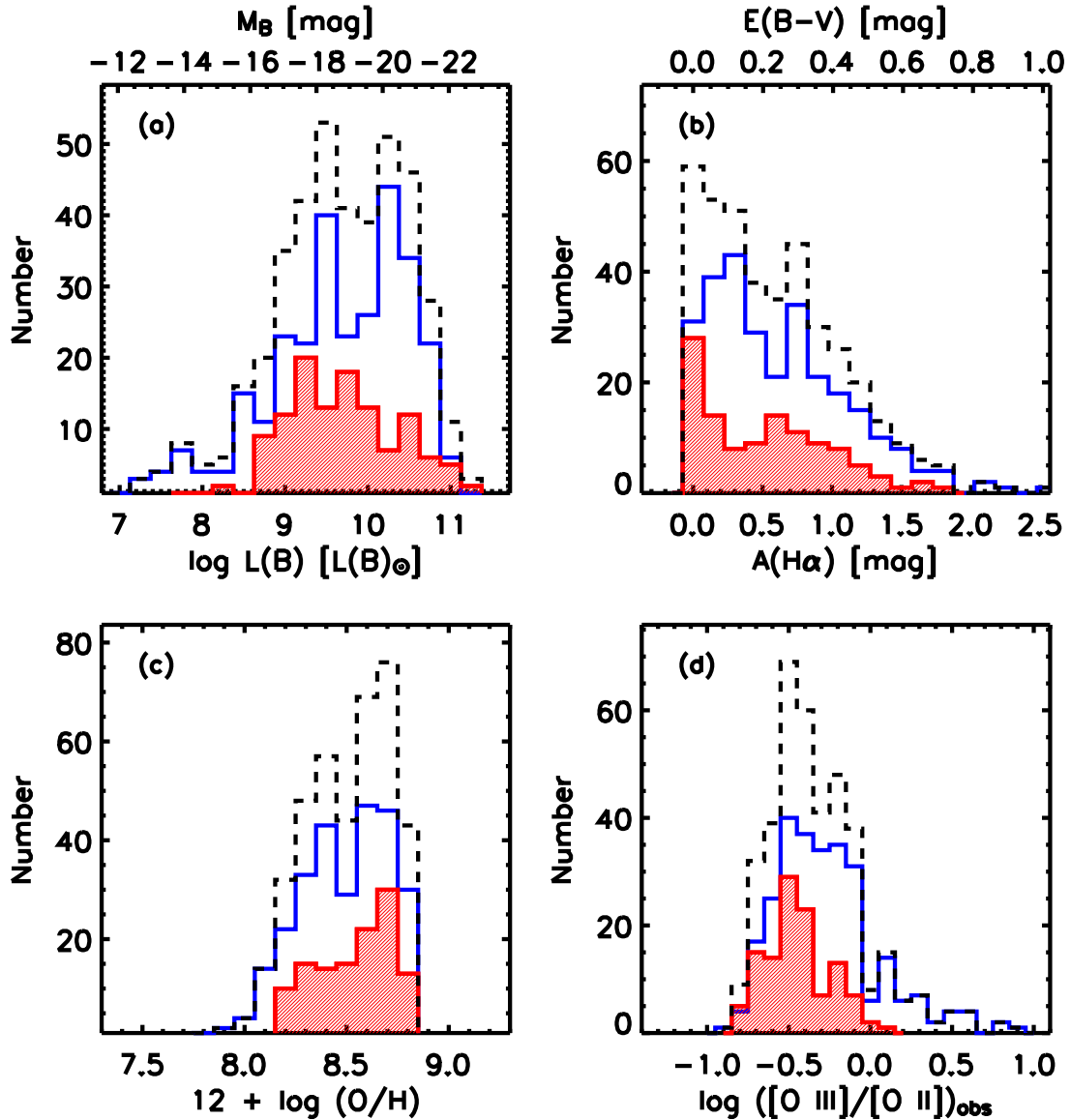


FIG. 3.— Distribution of spectrophotometric properties for the MK05 survey (unshaded histogram) and the NFGS (shaded histogram) (shown in blue and red, respectively, in the electronic edition). The *dashed* histogram shows the distribution for the combined integrated galaxy sample. (a) Distribution of B -band luminosity, $L(B)$, where $M_{\odot, B} = +5.42$ mag can be used to convert from $L(B)$ to M_B . (b) Distribution of $H\alpha$ extinction as derived from the $H\alpha/H\beta$ Balmer decrement and adopting the O’Donnell (1994) Milky Way extinction curve. (c) Distribution of gas-phase oxygen abundance, $12 + \log(O/H)$, determined using the methodology described in §3.4.2. (d) Distribution of the observed $([O\ III] \lambda 5007/[O\ II] \lambda 3727)_{\text{obs}}$ flux ratio, which is indicative of the hardness of the ionizing radiation field. See §2.1 for more details.

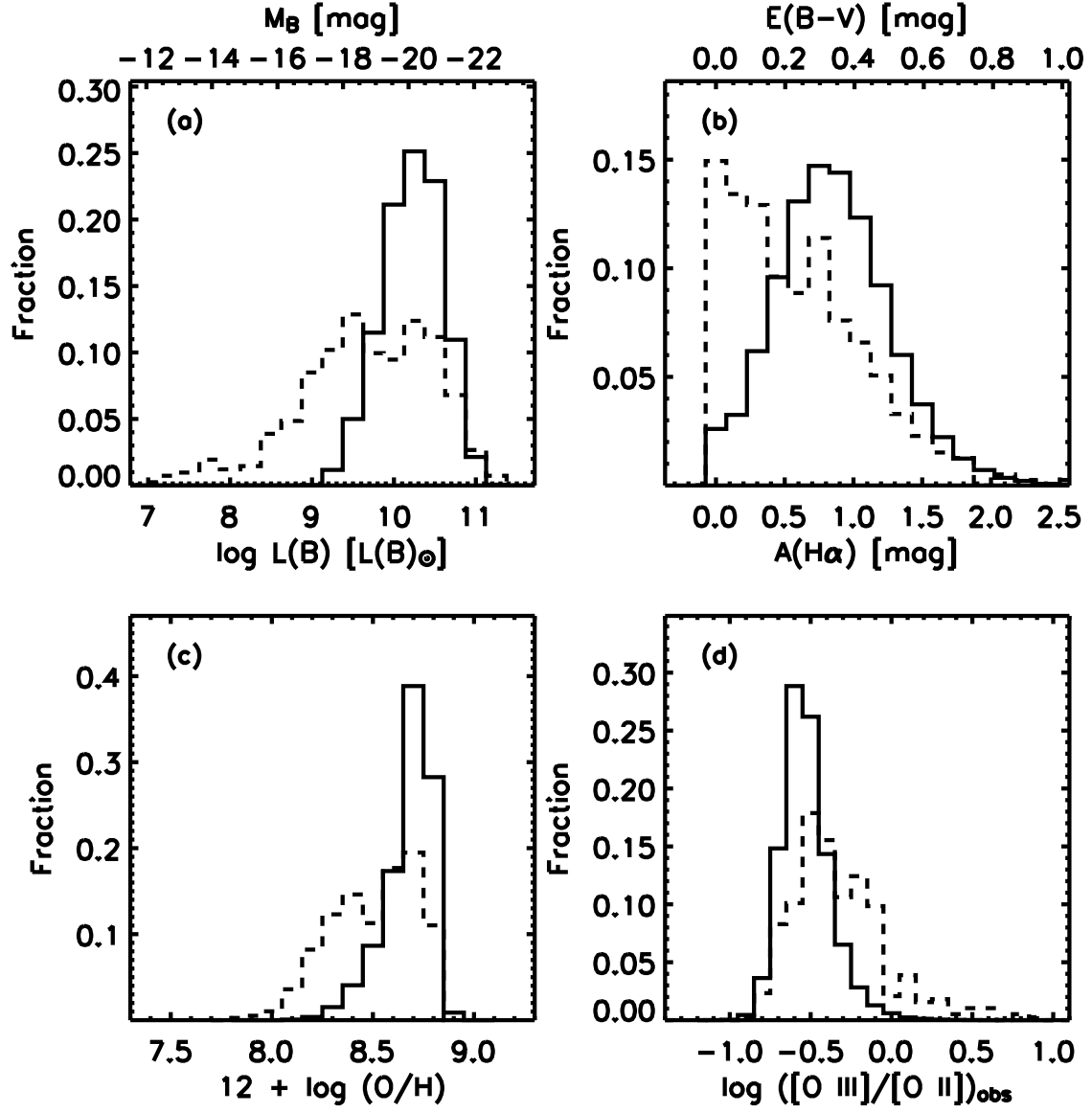


FIG. 4.— Distribution of spectrophotometric properties for the SDSS and integrated galaxy samples, plotted as *solid* and *dashed* histograms, respectively. See Figure 3 and §2.2 for additional details.

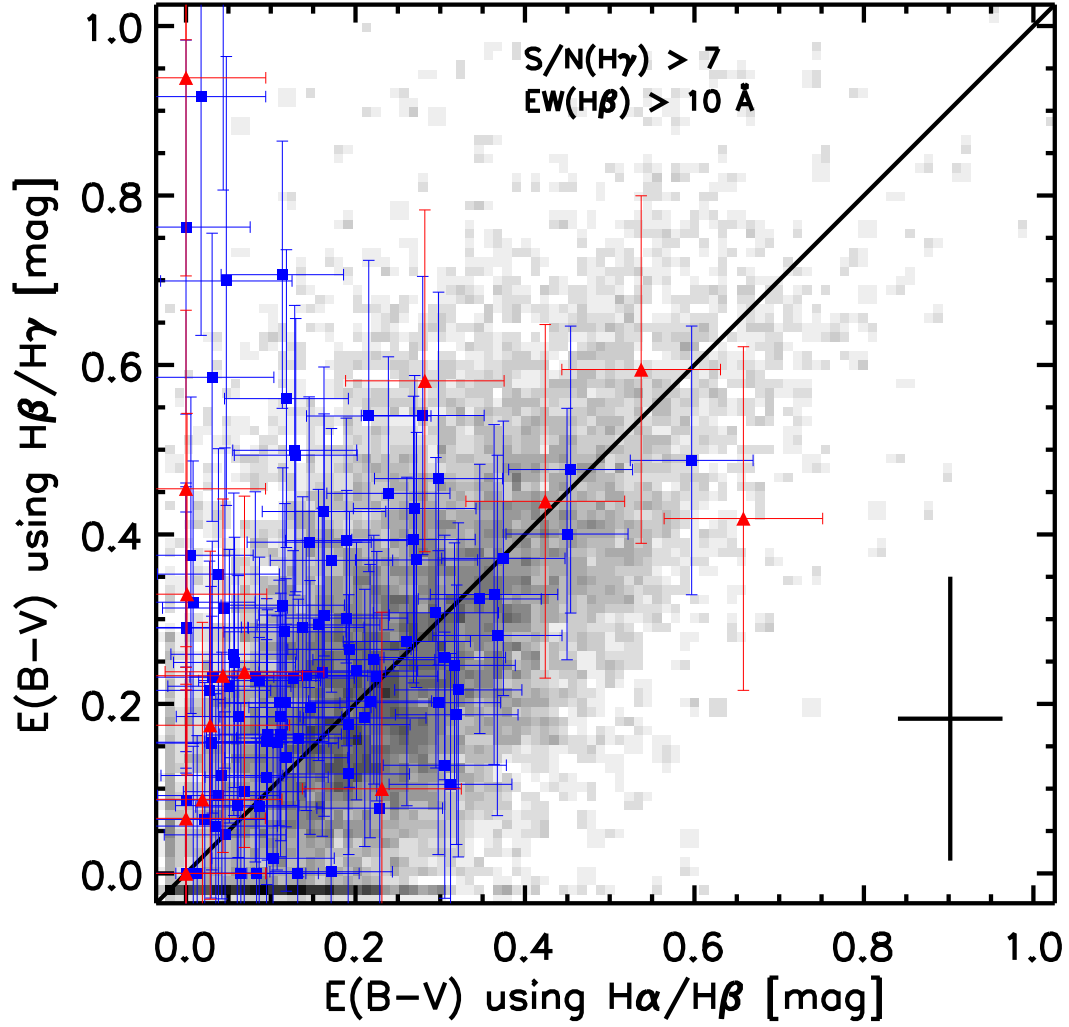


FIG. 5.— Comparison of the reddening values derived using the $H\alpha/H\beta$ and the $H\beta/H\gamma$ Balmer decrements for the MK05 sample (squares with error bars), the NFGS (triangles with error bars), and the SDSS (small points without error bars) (plotted in blue, red, and black, respectively, in the electronic edition). The *solid* line indicates equality of the two reddening estimates. We only include galaxies with $S/N(H\gamma) > 7$ and $EW(H\beta) > 10 \text{ \AA}$ in emission. The cross shows the median error of the SDSS data.

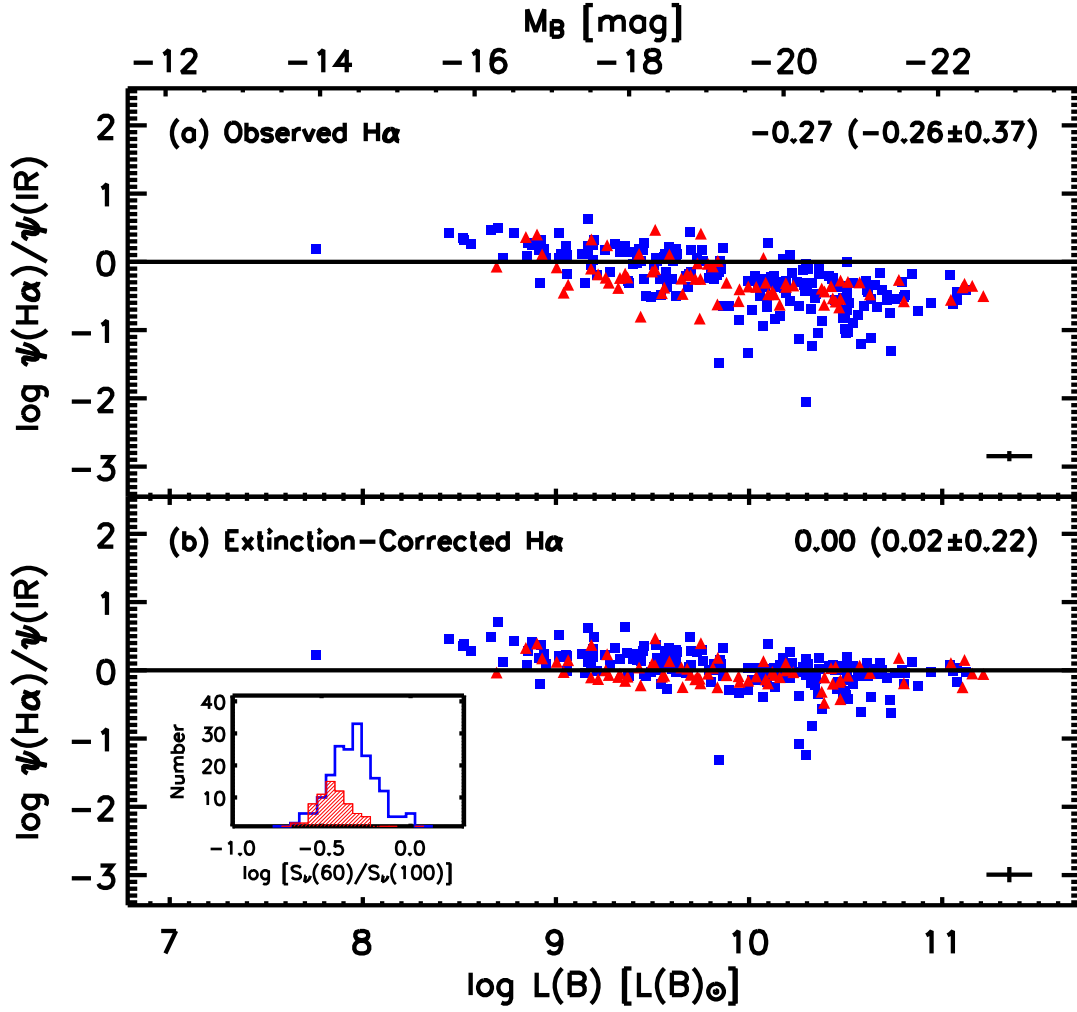


FIG. 6.— Logarithmic ratio of the $H\alpha$ and infrared SFRs, $\psi(H\alpha)/\psi(IR)$, versus the B -band luminosity, $L(B)$ using (a) the observed $H\alpha$ luminosity and (b) the extinction-corrected $H\alpha$ luminosity. The solid line indicates equality of the two SFR indicators. The symbols are defined in Figure 2. The cross in the lower-right of each panel indicates the average measurement uncertainty in the data, and the legend gives the median logarithmic ratio and, in parenthesis, the mean and standard deviation. The inset in panel (b) shows the distribution of $S_\nu(60\ \mu\text{m})/S_\nu(100\ \mu\text{m})$ flux ratios for the MK05 and NFGS samples as *unshaded* and *shaded* histograms, respectively (shown in blue and red, respectively, in the electronic edition).

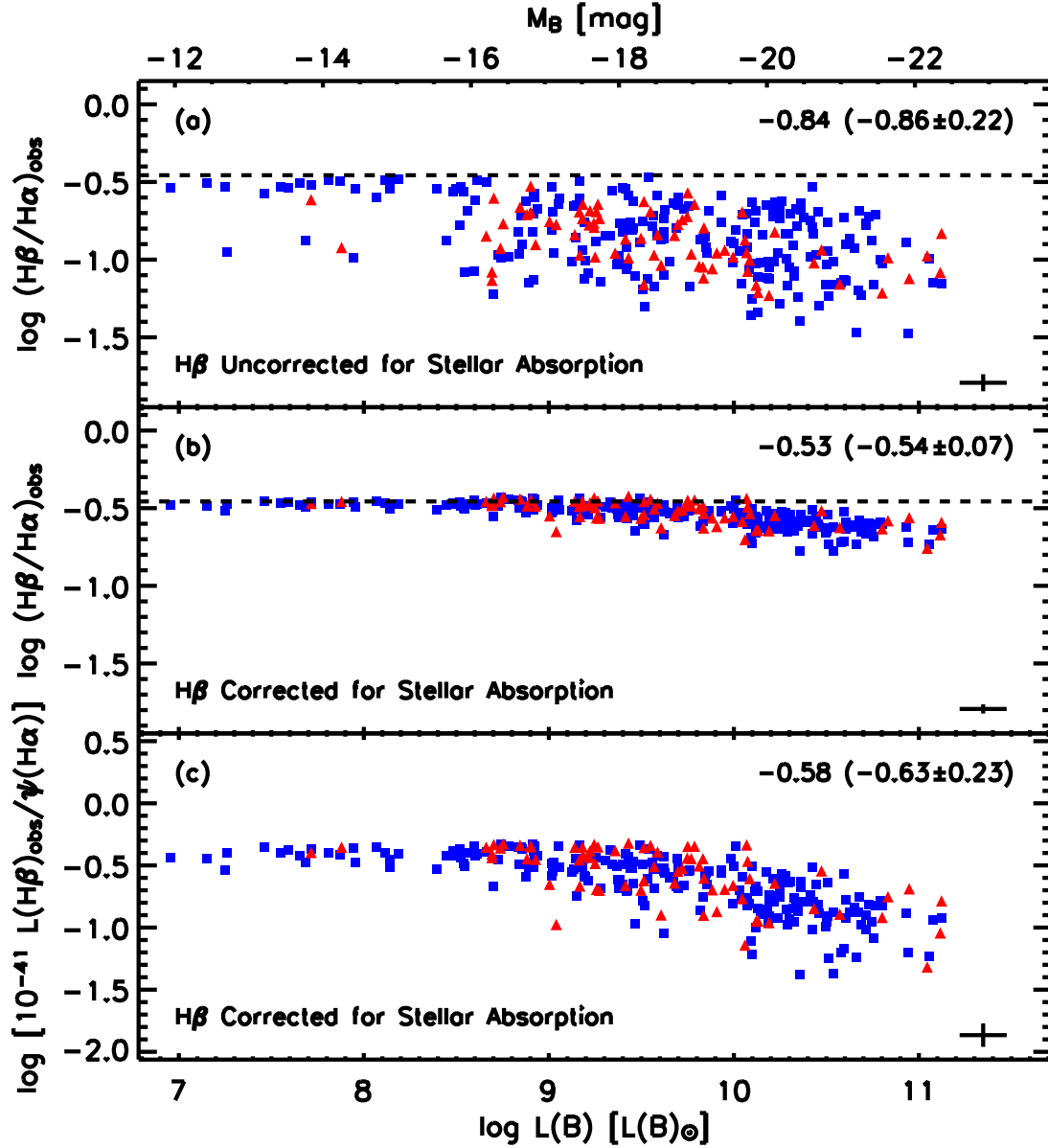


FIG. 7.— Variation in the $\text{H}\beta/\text{H}\alpha$ ratio versus the B -band luminosity, $L(B)$, for all galaxies in the integrated sample having $\text{EW}(\text{H}\beta) > 5 \text{ \AA}$ in emission. The *dashed* line in panels (a) and (b) indicates the intrinsic Balmer decrement, $\log (\text{H}\beta/\text{H}\alpha)_{\text{int}} \simeq -0.46$ dex (see §3.1). The symbols are defined in Figure 2. The cross in the lower-right of each panel indicates the average measurement uncertainty in the data, and the legend gives the median logarithmic ratio and, in parenthesis, the mean and standard deviation. (a) Observed $\text{H}\beta/\text{H}\alpha$ ratio without an $\text{H}\beta$ stellar absorption correction. (b) Identical to panel (a) except that $\text{H}\beta$ is now corrected for underlying stellar absorption. (c) Ratio of the observed $\text{H}\beta$ luminosity, $L(\text{H}\beta)_{\text{obs}}$, to the $\text{H}\alpha$ star-formation rate, $\psi(\text{H}\alpha)$, in units of $10^{-41} \mathcal{M}_\odot \text{ yr}^{-1}/(\text{erg s}^{-1})$.

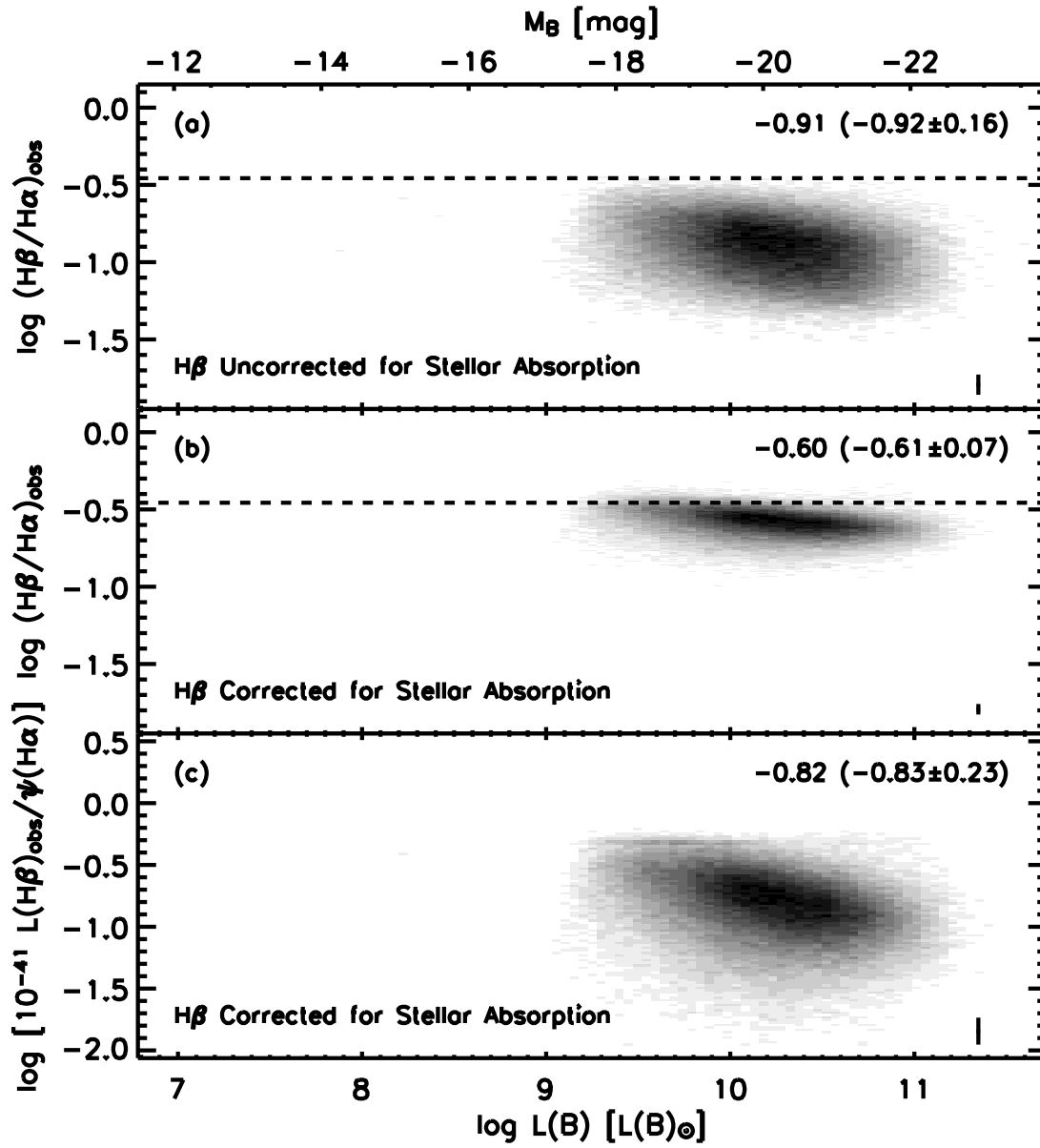


FIG. 8.— Same as Figure 7 but for the SDSS sample.

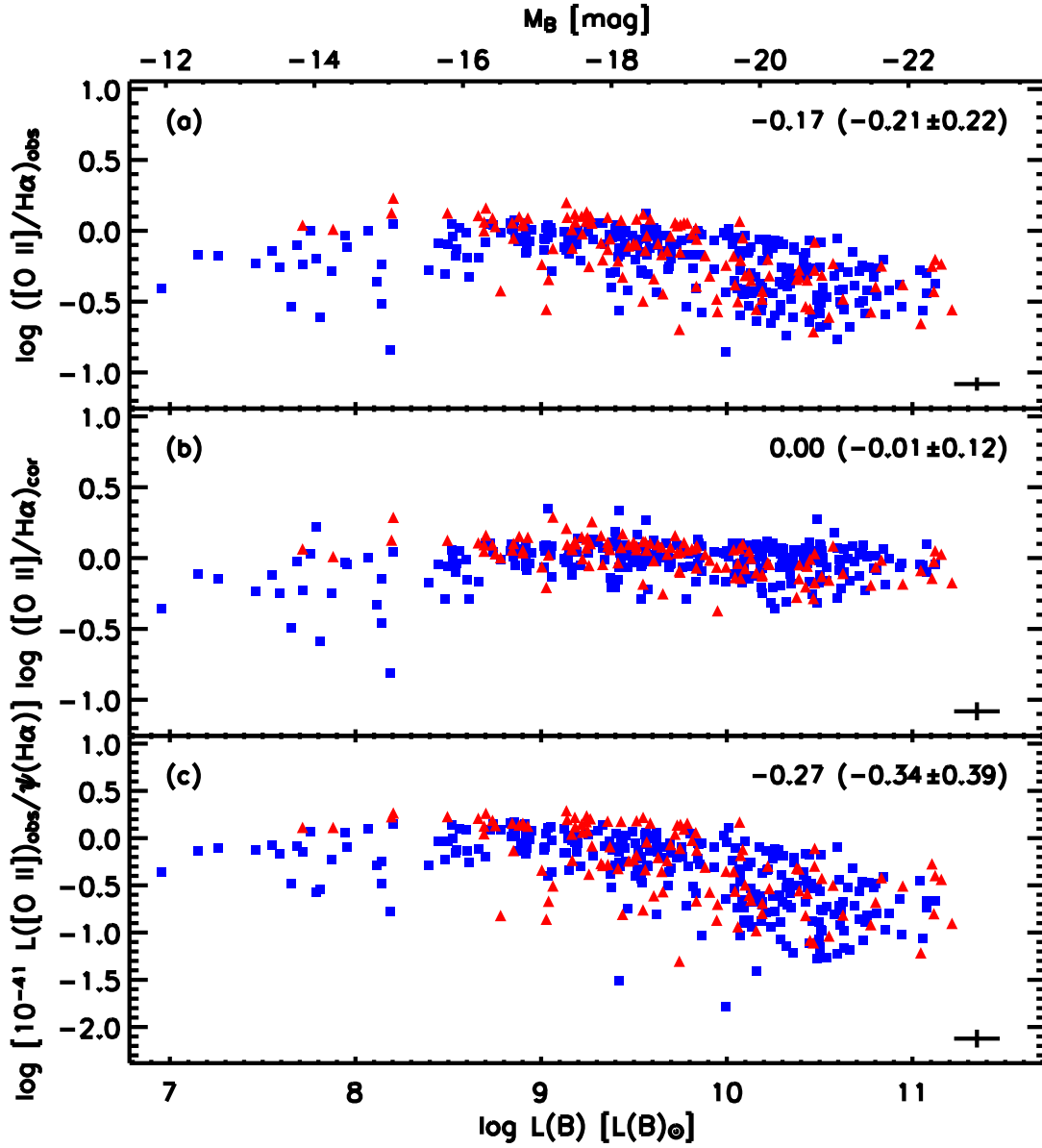


FIG. 9.— Dependence of the $[\text{O II}]/\text{H}\alpha$ ratio on the B -band luminosity, $L(B)$, in the integrated sample. The points have been coded as in Figure 2. The cross in the lower-right of each panel indicates the average measurement uncertainty in the data, and the legend gives the median logarithmic ratio and, in parenthesis, the mean and standard deviation. (a) Observed $[\text{O II}]/\text{H}\alpha$ ratio uncorrected for dust reddening. (b) Reddening-corrected $[\text{O II}]/\text{H}\alpha$ ratio. (c) Ratio of the observed $[\text{O II}]$ luminosity, $L([\text{O II}]_{\text{obs}})$, to the $\text{H}\alpha$ star-formation rate, $\psi(\text{H}\alpha)$, in units of $10^{-41} \mathcal{M}_{\odot} \text{yr}^{-1}/(\text{erg s}^{-1})$.

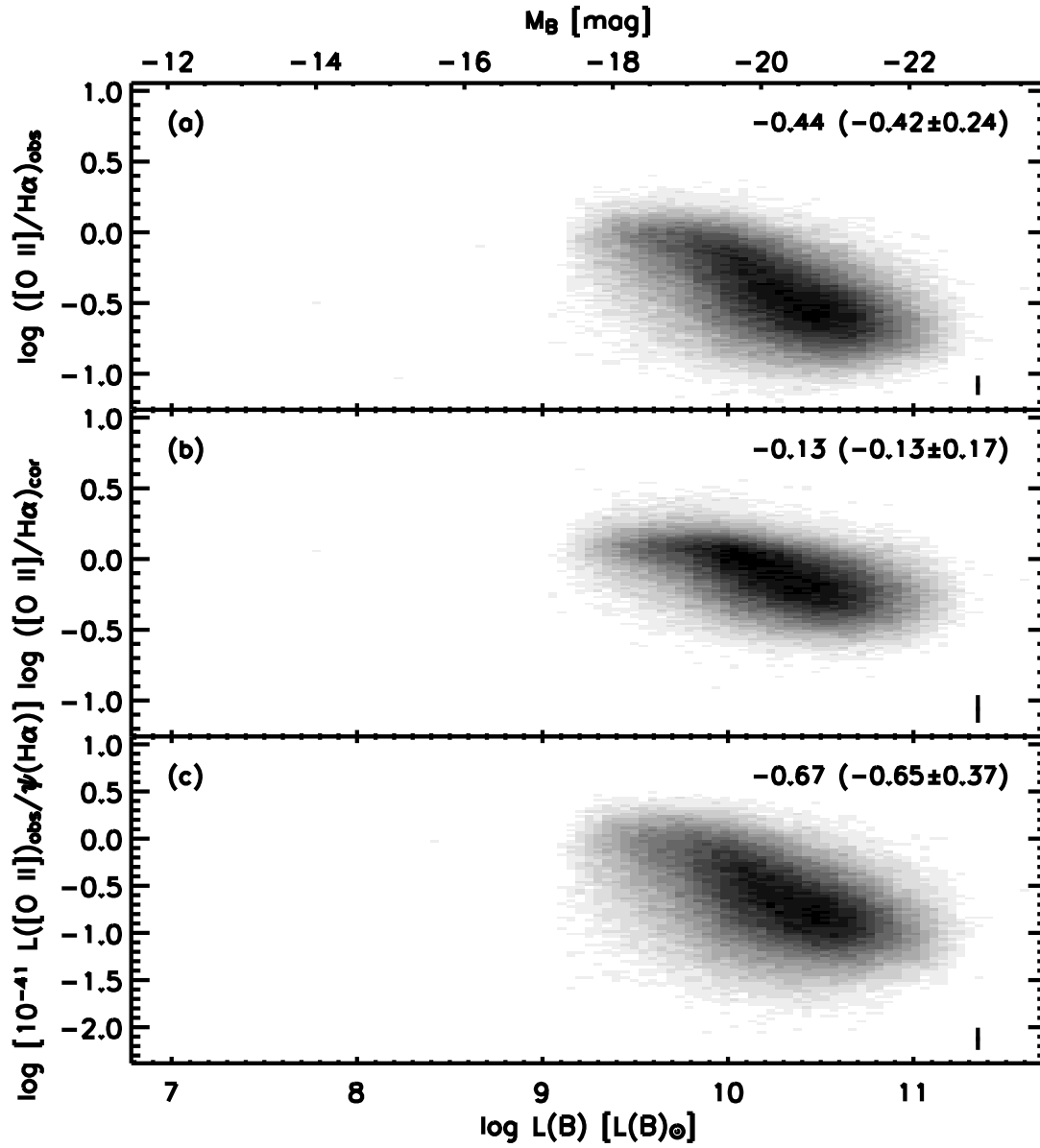


FIG. 10.— Same as Figure 9 but for the SDSS sample.

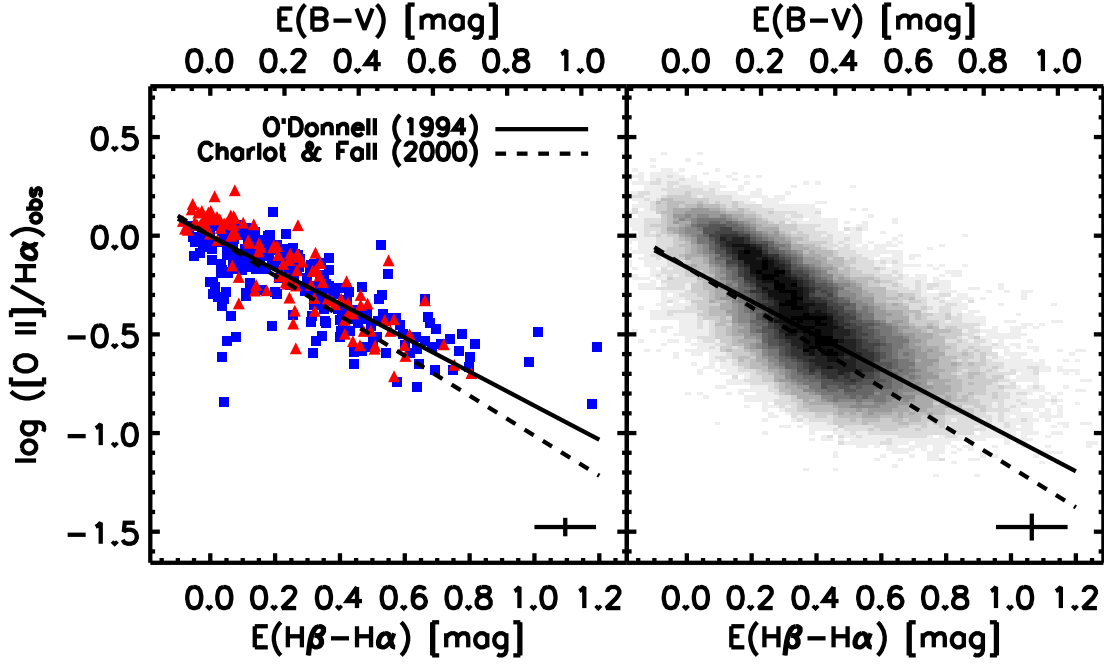


FIG. 11.— Correlation between the observed $[\text{O II}]/\text{H}\alpha$ ratio and the nebular reddening, $E(\text{H}\beta\text{-H}\alpha)$, for the integrated sample (*left*) and the SDSS (*right*). Refer to Figure 2 for the meaning of the symbols. The cross in the lower-right part of each panel indicates the average measurement uncertainty in the data. We plot the O'Donnell (1994) Galactic extinction curve and the Charlot & Fall (2000) dust attenuation law as *solid* and *dashed* lines, respectively, in both panels. In the left panel we set the normalization of the reddening curves to $\log([\text{O II}]/\text{H}\alpha)_{\text{obs}} = 0.00$ dex, and to $\log([\text{O II}]/\text{H}\alpha)_{\text{obs}} = -0.16$ dex in the right panel.

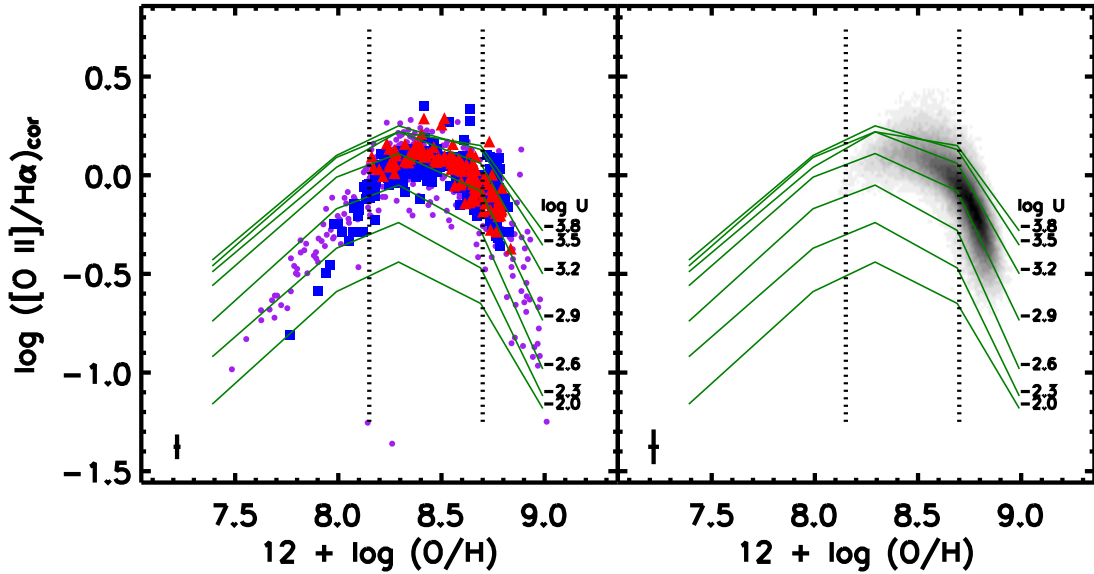


FIG. 12.— Reddening-corrected $[\text{O II}]/\text{H}\alpha$ ratio versus the nebular oxygen abundance, $12 + \log(\text{O}/\text{H})$, for the integrated sample and H II regions (*left*), as coded in Figure 2, and the SDSS sample (*right*). The curves show the results of detailed photoionization modeling by Kewley et al. (2001a) for six values of the ionization parameter, $-3.8 < \log U < -2.0$. The vertical dotted lines divide each panel into three metallicity regimes: $12 + \log(\text{O}/\text{H}) < 8.15$ dex, $8.15 < 12 + \log(\text{O}/\text{H}) < 8.7$ dex, and $12 + \log(\text{O}/\text{H}) > 8.7$ dex. The cross in the lower-left part of each panel indicates the typical measurement uncertainty, excluding any systematic errors in the adopted abundance calibration.

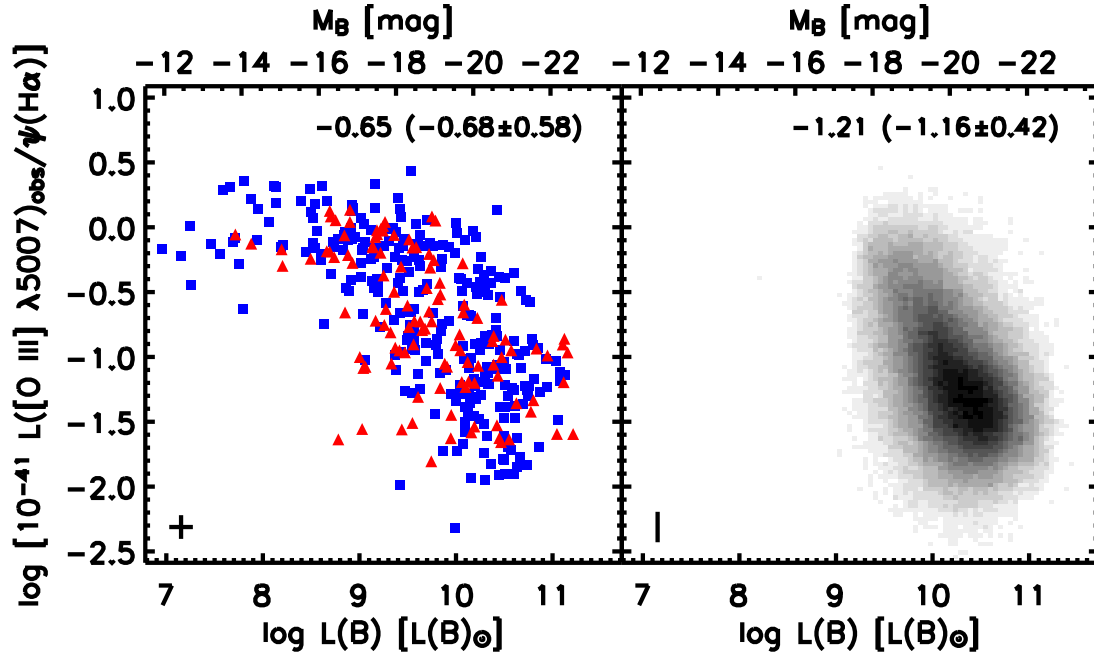


FIG. 13.— Ratio of the observed [O III] $\lambda 5007$ luminosity, $(L([\text{O III}] \lambda 5007))_{\text{obs}}$, to the $\text{H}\alpha$ star-formation rate, $\psi(\text{H}\alpha)$, versus the B -band luminosity, $L(B)$, for the integrated sample (*left*) and the SDSS (*right*). The symbols in the left panel are defined in Figure 2. The cross in the lower-left corner indicates the average measurement uncertainty in the data, and the legend gives the median logarithmic ratio and, in parenthesis, the mean and standard deviation.

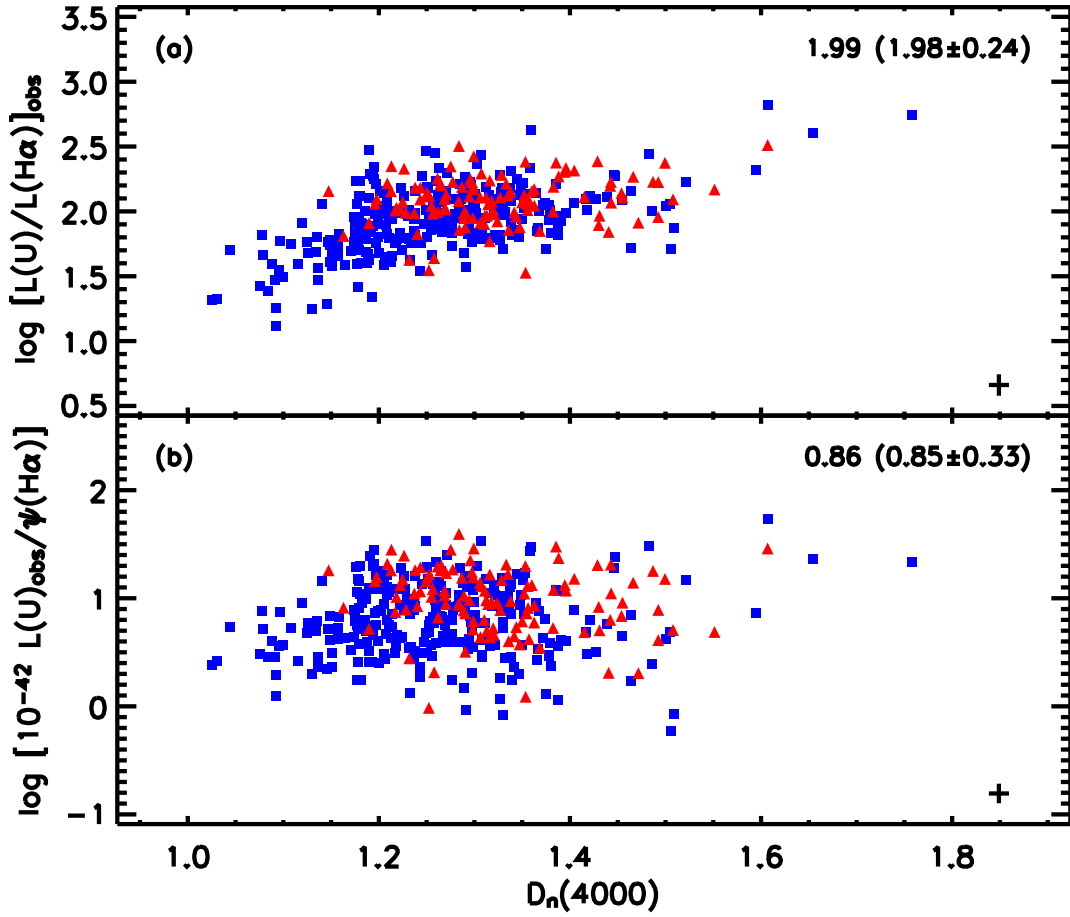


FIG. 14.— Logarithmic U -band to $H\alpha$ luminosity ratio versus the 4000-Å break, $D_n(4000)$. Figure 2 defines the symbols used, and the cross in the lower-right indicates the average measurement uncertainty in the data. The legend gives the median logarithmic ratio and, in parenthesis, the mean and standard deviation. (a) Observed $L(U)/L(H\alpha)$ ratio. (b) Ratio of the observed U -band luminosity, $L(U)_{\text{obs}}$, to the $H\alpha$ star-formation rate, $\psi(H\alpha)$, in units of $10^{-42} \mathcal{M}_{\odot} \text{ yr}^{-1}/(\text{erg s}^{-1})$.

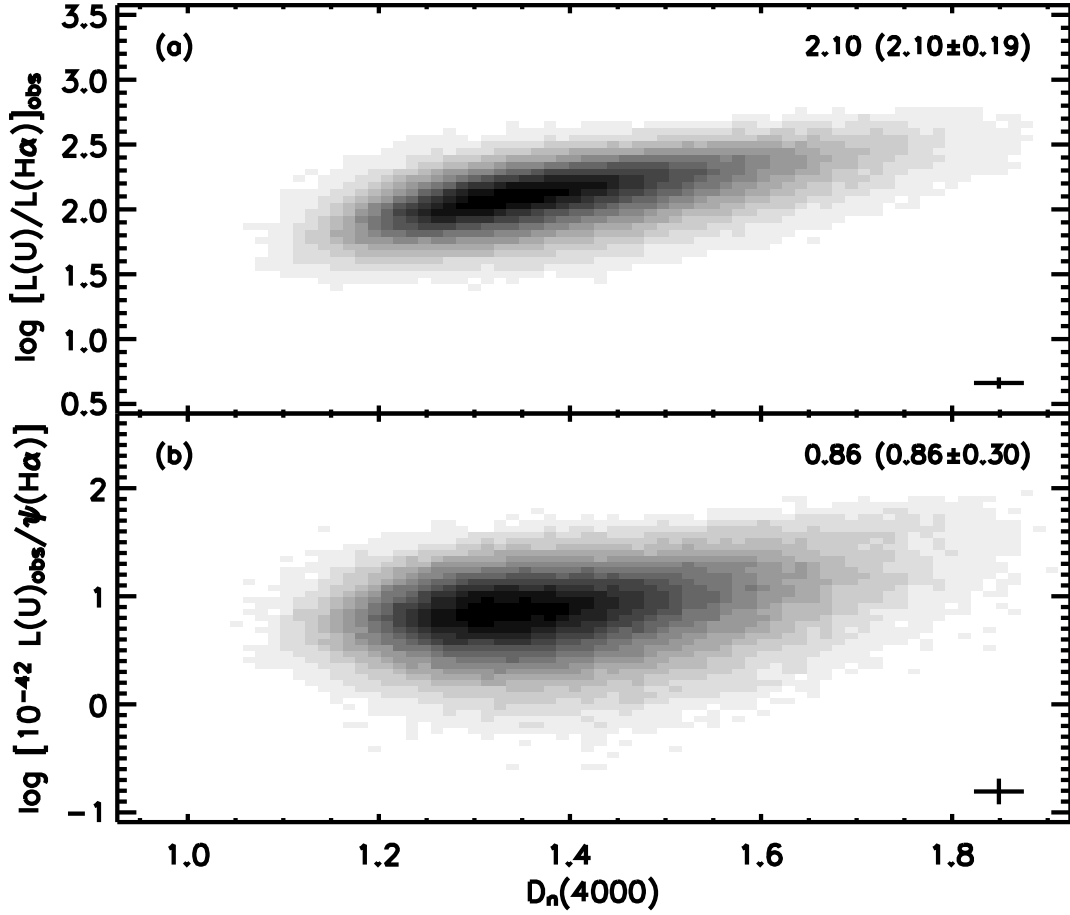


FIG. 15.— Same as Figure 14 but for the SDSS sample.

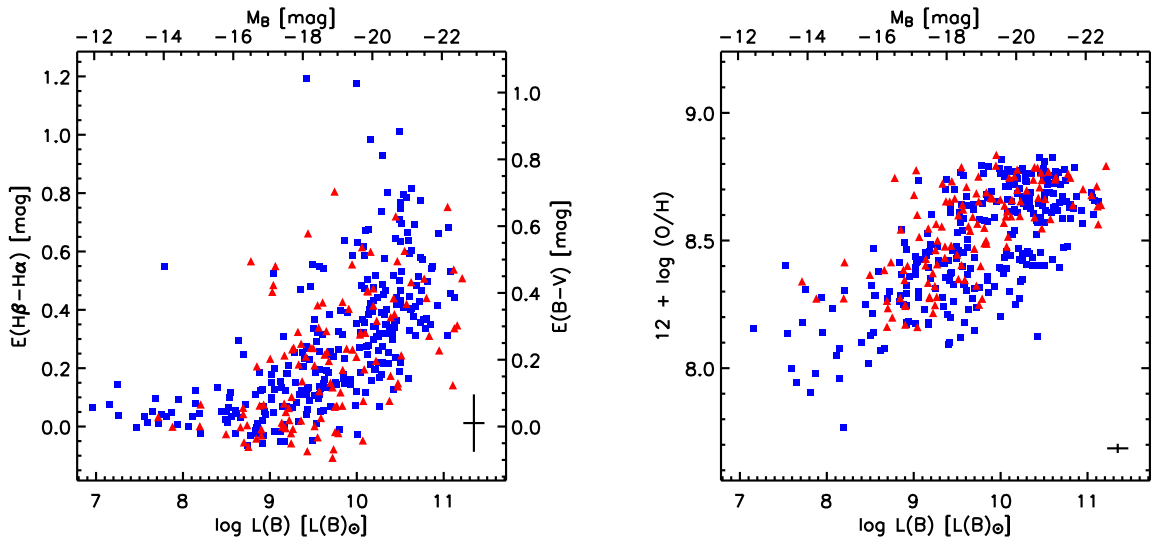


FIG. 16.— Empirical correlations between luminosity and dust extinction (*left*), and between luminosity and oxygen abundance (*right*). Figure 2 defines the symbols. The cross in the lower-right corner of each figure shows the average measurement uncertainty of the data, excluding any systematic error.

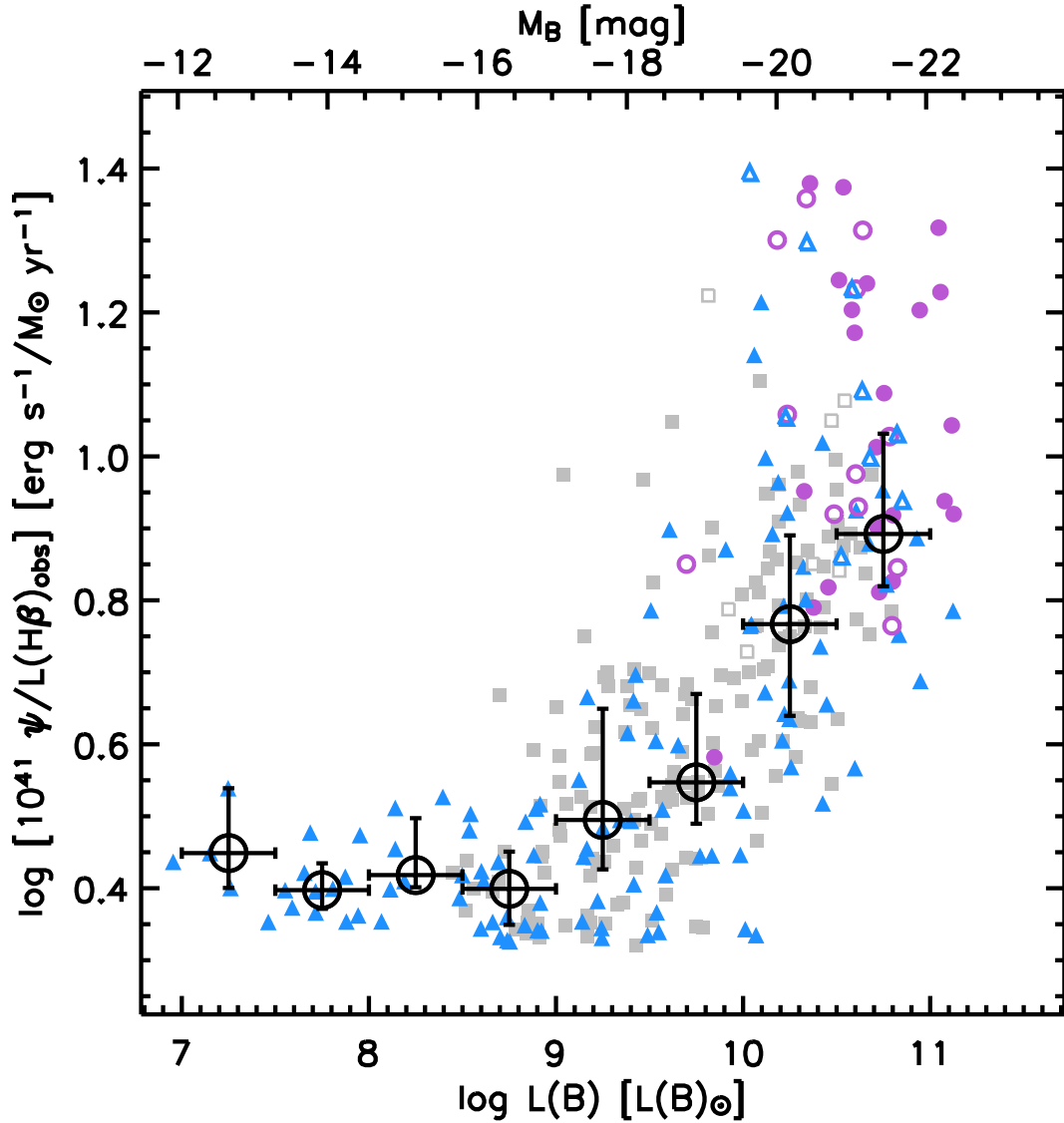


FIG. 17.— Empirical $H\beta$ $\lambda 4861$ SFR calibration. The symbols indicate the infrared luminosity of each galaxy: circular symbols indicate $L(\text{IR}) > 10^{11} L_{\odot}$; squares indicate $L(\text{IR}) < 10^{11} L_{\odot}$; and triangles do not have a measured infrared luminosity. (These symbols are colored purple, grey, and blue, respectively, in the electronic edition.) Open and filled symbols indicate the AGN and star-forming galaxies in each category, respectively, as classified in §2.1. The large open circles give the median $\psi/L(H\beta)_{\text{obs}}$ ratio in 0.5 dex luminosity bins, and the lower and upper error bars give the 25% and 75% quartile of the distribution in each bin, respectively. One galaxy, IC 1623 B, an AGN without a measured infrared luminosity, does not appear on this plot because it deviates significantly from the rest of the sample. Its blue luminosity is $\sim 10^{10} L(B)_{\odot}$ and its logarithmic $\psi/L(H\beta)_{\text{obs}}$ ratio is $\sim 2.5 \times 10^{41} \text{ erg s}^{-1}/(\mathcal{M}_{\odot} \text{ yr}^{-1})$.

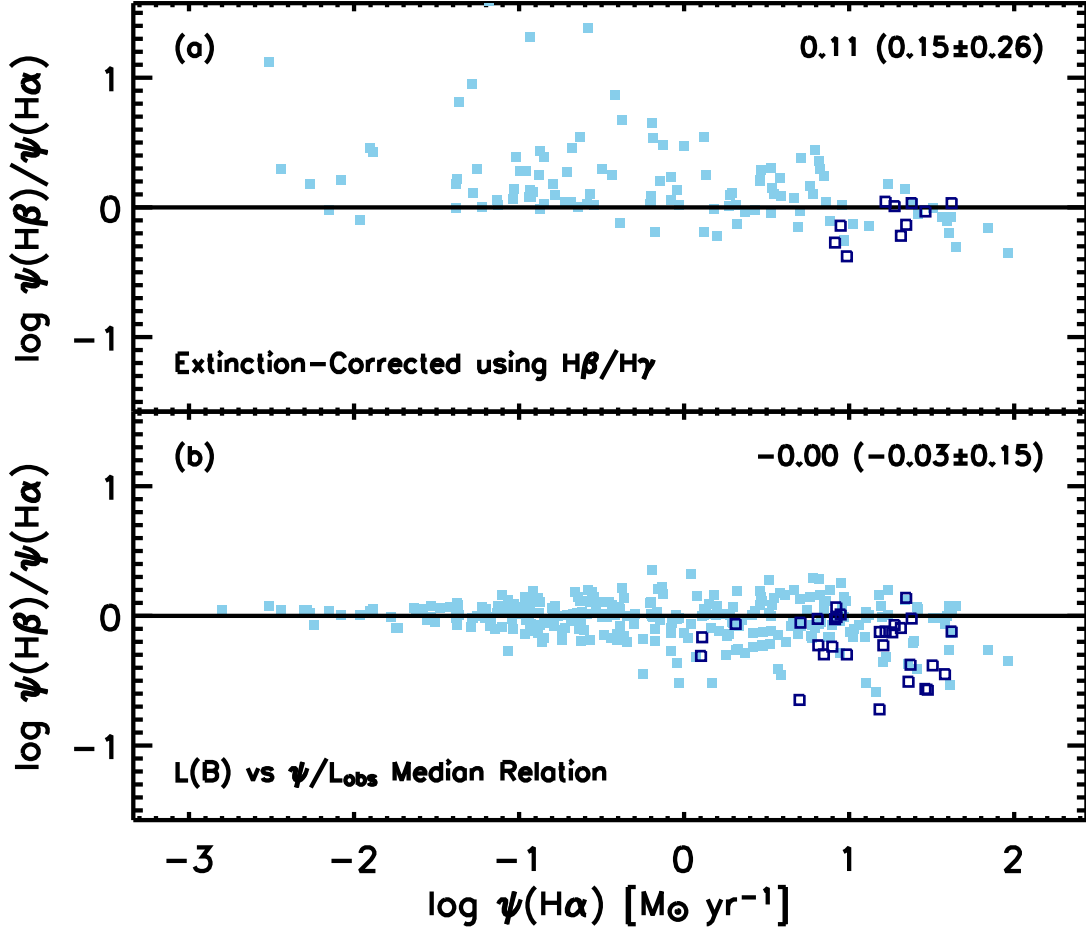


FIG. 18.— Comparison of $\psi(\text{H}\beta)$ derived using two different methods versus $\psi(\text{H}\alpha)$. Filled and open symbols indicate star-forming galaxies and AGN, respectively, as classified in §2.1 (colored light blue and dark blue, respectively, in the electronic edition). (a) $\psi(\text{H}\beta)$ derived using the $\text{H}\beta/\text{H}\gamma$ ratio to correct for dust extinction and applying equation (4) assuming $L(\text{H}\beta) = L(\text{H}\alpha)/2.86$. As discussed in §4.2, we only include galaxies having $\text{EW}(\text{H}\beta) > 10 \text{ \AA}$ in emission and $\text{S}/\text{N}(\text{H}\gamma) > 7$. (b) $\psi(\text{H}\beta)$ obtained using the empirical SFR calibration developed in §4.2 for all galaxies having $\text{EW}(\text{H}\beta) > 5 \text{ \AA}$ in emission.

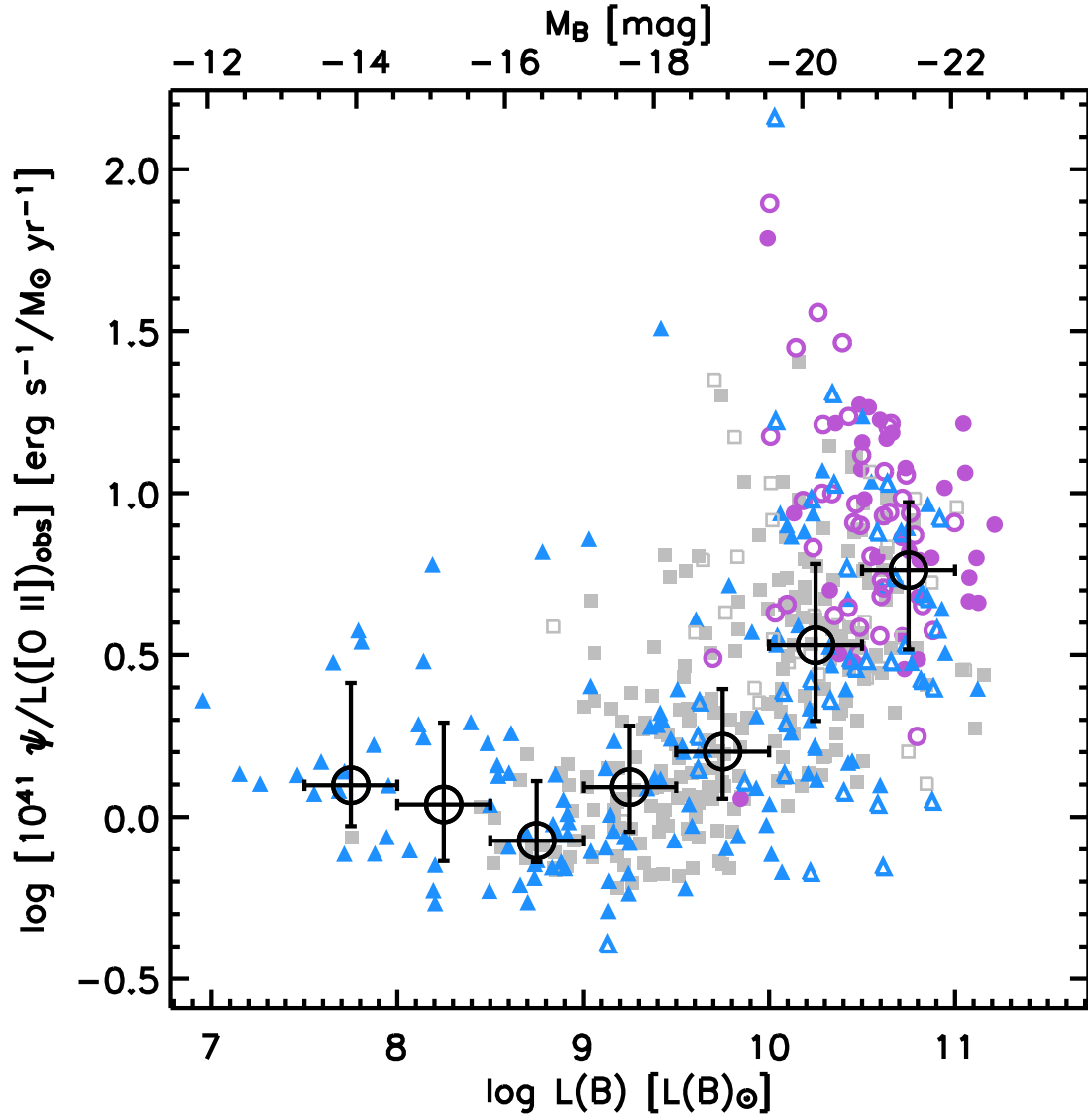


FIG. 19.— Empirical [O II] $\lambda 3727$ SFR calibration. The symbols have been defined in Figure 17. The large open circles give the median $\psi/L([\text{O II}])_{\text{obs}}$ ratio in 0.5 dex luminosity bins, and the lower and upper error bars give the 25% and 75% quartile of the distribution in each bin, respectively.

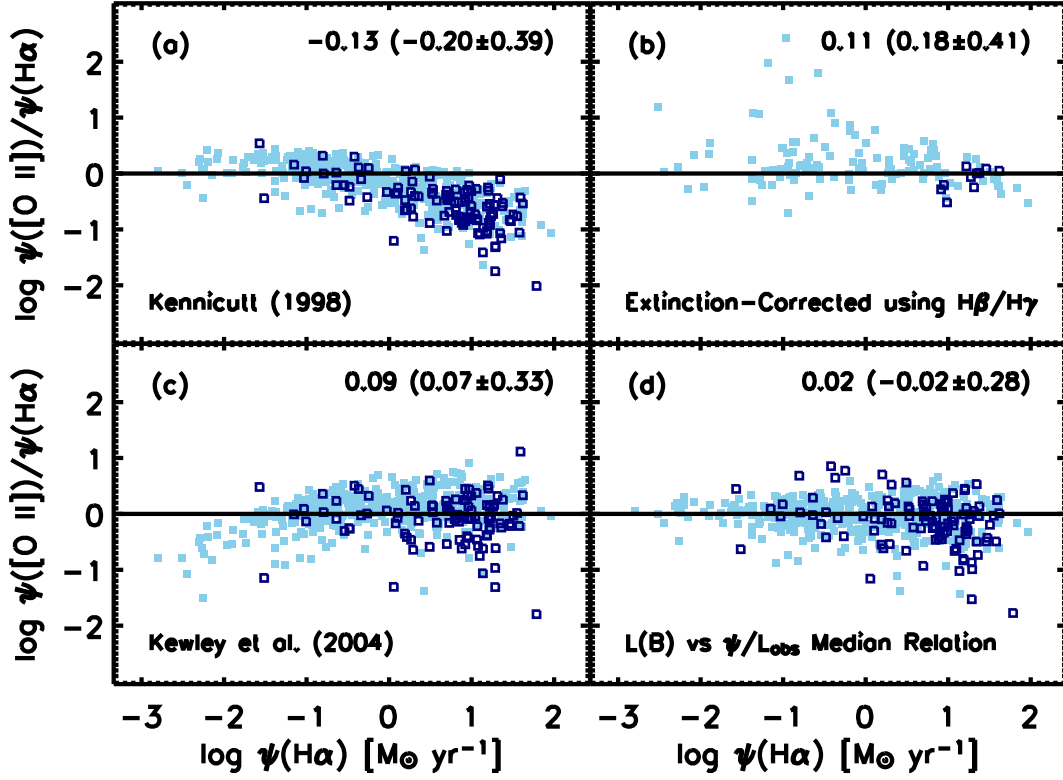


FIG. 20.— Comparison of $\psi([\text{O II}])$ using four independent calibrations versus $\psi(\text{H}\alpha)$. Figure 18 defines the different symbols. (a) $\psi([\text{O II}])$ obtained using the Kennicutt (1998) calibration. (b) Here, we correct $[\text{O II}]$ for extinction using the measured $\text{H}\beta/\text{H}\gamma$ ratio, assume an intrinsic $[\text{O II}]/\text{H}\alpha = 1$ ratio, and apply equation (4) to estimate $\psi([\text{O II}])$. This panel only includes objects having $\text{EW}(\text{H}\beta) > 10 \text{ \AA}$ in emission and $\text{S/N}(\text{H}\gamma) > 7$. (c) $\psi([\text{O II}])$ estimated by applying the empirical abundance and extinction corrections advocated by Kewley et al. (2004). (d) $\psi([\text{O II}])$ derived using the calibration developed in §4.3.

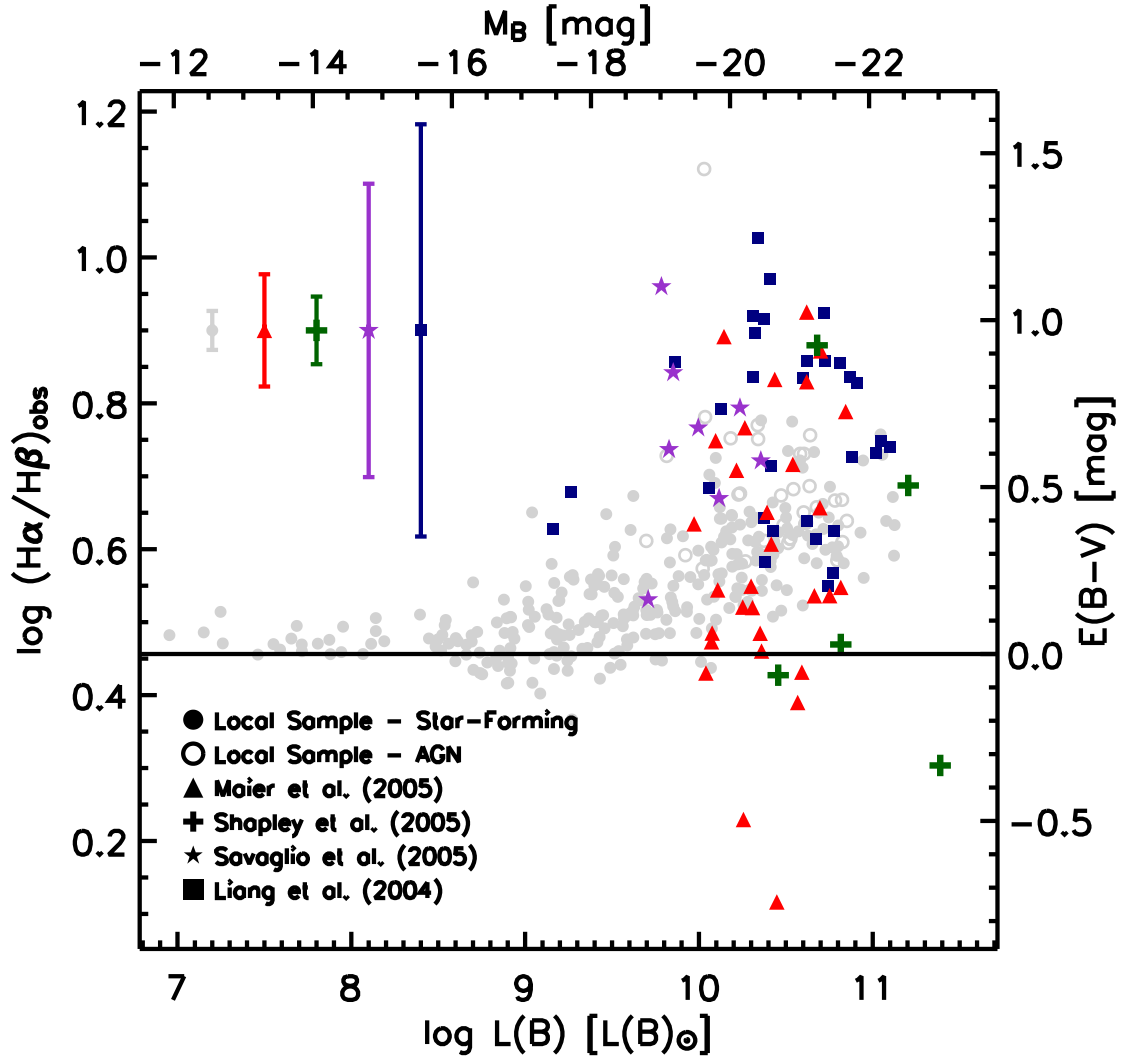


FIG. 21.— Comparison of the local and intermediate-redshift ($z = 0.7 - 1.4$) relation between the observed $H\alpha/H\beta$ ratio and the B -band luminosity, $L(B)$. The *solid* line corresponds to the intrinsic $H\alpha/H\beta$ Balmer decrement. The error bars in the upper-left part of the figure indicate the median 1σ uncertainty in the data for each sample, as defined in the legend. Note that the data from Savaglio et al. (2005) and Liang et al. (2004a) have been derived from the $H\beta/H\gamma$ ratio, as described in §5.

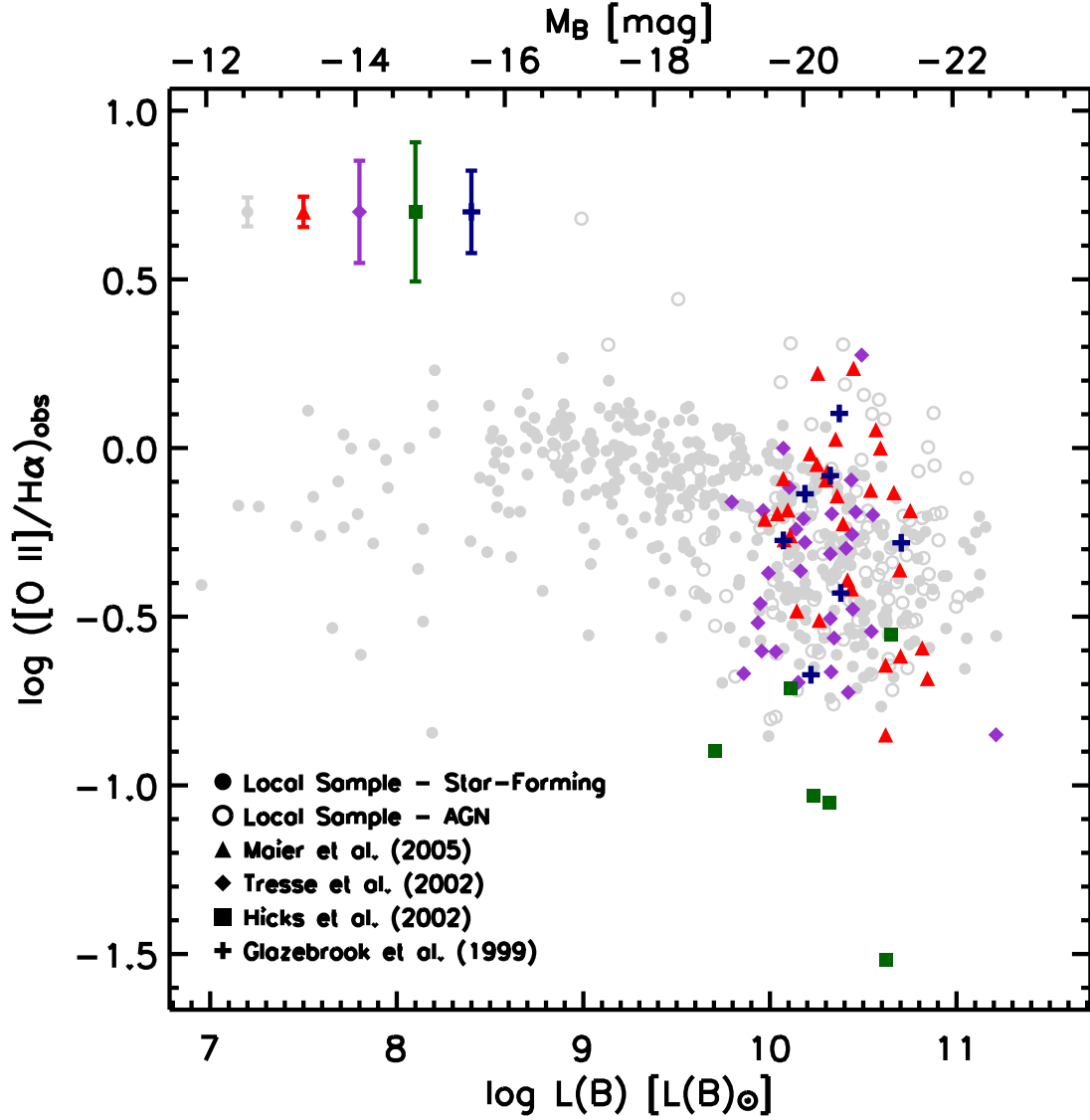


FIG. 22.— Correlation between the observed $[O \text{ II}]/H\alpha$ ratio and the B -band luminosity, $L(B)$, for our local spectroscopic sample and several intermediate-redshift ($z = 0.5 - 1.5$) galaxy samples. The error bars in the upper-left part of the figure indicate the median 1σ uncertainty in the data for each sample, as defined in the legend.

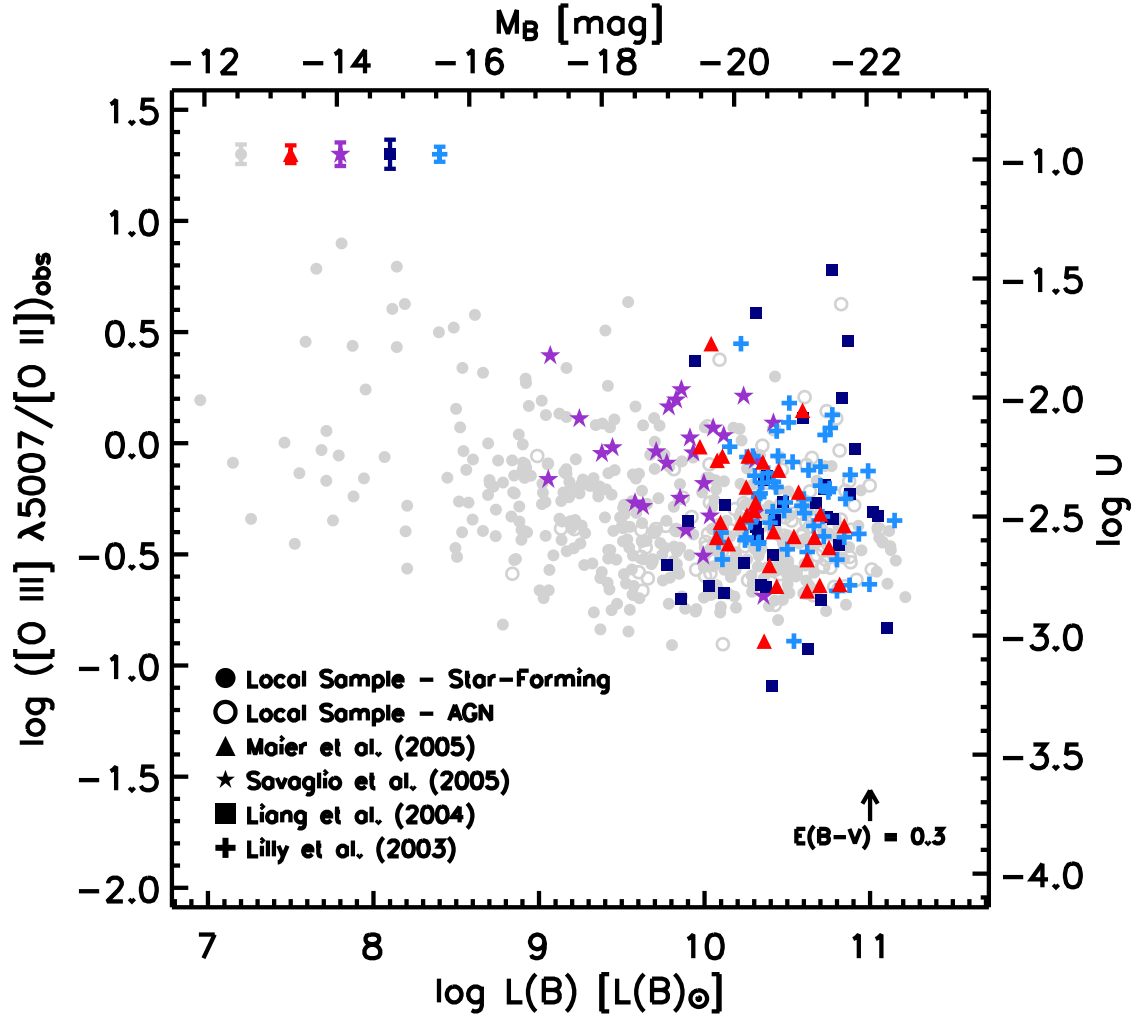


FIG. 23.— Comparison of the local and intermediate-redshift ($z = 0.4 - 1.0$) relation between the observed $[O \text{ III}] \lambda 5007/[O \text{ II}]$ ratio and the B -band luminosity, $L(B)$. The error bars in the upper-left part of the figure indicate the median 1σ uncertainty in the data for each sample, as defined in the legend. The arrow indicates the effect of 0.3 mag of reddening on an intrinsic $[O \text{ III}]/[O \text{ II}]$ ratio of -1.7 dex, neglecting any reddening effects on $L(B)$. To estimate the sequence in ionization parameter, $\log U$, from the $[O \text{ III}]/[O \text{ II}]$ ratio (right axis), we utilize the solar-metallicity, continuous star formation photoionization models by Kewley et al. (2001a).

TABLE 1
H β λ 4861 STAR-FORMATION RATE CONVERSION FACTORS

$\log L(B)$ [$L(B)_\odot$]	M_B [mag]	$\log [\psi/L(\text{H}\beta)_{\text{obs}}]$ [$10^{41} \text{ erg s}^{-1}/(\mathcal{M}_\odot \text{ yr}^{-1})$]				
		P_{25}	P_{50}	P_{75}	$\langle R \rangle$	σ_R
7.25	-12.68	0.400	0.449	0.539	0.435	0.079
7.75	-13.93	0.371	0.397	0.435	0.403	0.042
8.25	-15.18	0.401	0.418	0.497	0.431	0.057
8.75	-16.43	0.349	0.399	0.451	0.414	0.080
9.25	-17.68	0.426	0.495	0.649	0.526	0.147
9.75	-18.93	0.490	0.547	0.670	0.583	0.157
10.25	-20.18	0.639	0.767	0.890	0.775	0.188
10.75	-21.43	0.819	0.892	1.032	0.927	0.190

NOTE. — The columns labeled P_{25} , P_{50} , and P_{75} give the 25, 50 (median), and 75 percentile of the $\psi/L(\text{H}\beta)_{\text{obs}}$ distribution, respectively, in bins of 0.5 dex in luminosity. $\langle R \rangle$ and σ_R give the mean and standard-deviation of the distribution in each bin.

TABLE 2
[O II] λ 3727 STAR-FORMATION RATE CONVERSION FACTORS

$\log L(B)$ [$L(B)_\odot$]	M_B [mag]	$\log [\psi/L([\text{O II}])_{\text{obs}}]$ [$10^{41} \text{ erg s}^{-1}/(\mathcal{M}_\odot \text{ yr}^{-1})$]				
		P_{25}	P_{50}	P_{75}	$\langle R \rangle$	σ_R
7.75	-13.93	-0.028	0.098	0.414	0.156	0.240
8.25	-15.18	-0.136	0.039	0.291	0.109	0.313
8.75	-16.43	-0.140	-0.074	0.111	-0.017	0.185
9.25	-17.68	-0.046	0.092	0.282	0.136	0.292
9.75	-18.93	0.056	0.201	0.395	0.261	0.347
10.25	-20.18	0.297	0.530	0.781	0.545	0.332
10.75	-21.43	0.517	0.762	0.972	0.749	0.285

NOTE. — The columns labeled P_{25} , P_{50} , and P_{75} give the 25, 50 (median), and 75 percentile of the $\log [\psi/L([\text{O II}])_{\text{obs}}]$ distribution, respectively, in bins of 0.5 dex in luminosity. $\langle R \rangle$ and σ_R give the mean and standard-deviation of the distribution in each bin.